INTEGRATION OF ADVANCED MANUFACTURING IN THE MECHANICAL DESIGN OF REFLECTIVE OPTICS

by

Nicholas Wayne Horvath

A dissertation submitted to the faculty of
The University of North Carolina at Charlotte
in partial fulfillment of the requirements
for the degree of Doctor of Philosophy in
Mechanical Engineering

Charlotte

2020

Approved by:

Dr. Matthew Davies

Dr. Christopher Evans

Dr. Steven Patterson

Dr. Scott Smith

Dr. Thomas Suleski

ABSTRACT

NICHOLAS WAYNE HORVATH. Integration of advanced manufacturing in the mechanical design of reflective optics. (Under the direction of DR. MATTHEW DAVIES)

High-performance freeform optical systems, designed for broad spectral imaging from the visible to the far infrared, place new demands on optical design, precision manufacturing, and precision metrology. In this dissertation, four key aspects are addressed (i) precision placement of freeform optics, (ii) closed loop iterative manufacturing and metrology, (iii) advanced materials, and (iv) design for manufacture. The dissertation includes a new kinematic mount design used for manufacturing and metrology of a freeform optic, an experimental study on additively manufactured silicon carbide for optical applications, and a new design methodology for higher efficiency lightweight mirrors considering additive manufacturing as the main process chain.

To meet the tolerances on figure, roughness, and relative positioning in such systems requires the ability to perform metrology and manufacturing corrections on freeform optics in a continuous feedback loop. This feedback loop requires a common interface for machining and manufacturing platforms. Chapter 2 describes the design, analysis, and testing of such an interface suitable for use with single point diamond turning and deterministic micro-grinding. The interface utilizes a torsionally preloaded, robust, kinematic mount capable of supporting manufacturing process loads while maintaining the position repeatability in five degrees of freedom required for the measurement and correction of optical figure. Results from a prototype system demonstrate an absolute and relative in-plane position uncertainty less than 200 nm and 50 nm, respectively, and the axial position uncertainty of 40 nm absolute and 10 nm relative. The absolute and relative angular positioning uncertainties less than 1 µrad and 0.25 µrad respectively. The results exceed the requirements for many optical systems. The mount is also suitable for use in opto-mechanical assembly, so that

the same platform can be used for manufacturing, metrology, final assembly, testing, and service.

Many of the properties of silicon carbide (SiC) are advantageous for optical applications, such as telescope mirrors and industrial laser systems. However, the base shapes of complex components are costly and difficult to manufacture. Leveraging additive manufacturing, near net complex components are readily processed. In Chapter 3, an investigation on the post processing of additively manufactured SiC (AM SiC) compared to chemical vapor deposited (CVD) SiC. The specific grinding energy for the AM SiC was lower than CVD, however the trends were the same. A specular finish was observed on both materials but the AM SiC finish was limited due to residual porosity.

Additive manufacturing is a disruptive technology that can be leveraged by the redesign of components in most engineering fields. The fundamental engineering resources for lightweight mirrors were developed more than 30 years ago with a main design limitation, state of the art manufacturing. Chapter 4 presents two design methodologies for the design of lightweight mirrors. The first method utilizes analytical expressions to design a traditional isogrid mirror, which provided the foundation for most lightweight mirrors to date. The second method employs a combination of topology optimization, lattice infill, and analytical estimation to develop an advanced lightweight mirror designed for additive manufacturing. The advanced mirror design outperforms the traditional design for each functional requirement including a 94% reduction in predicted surface quilting and a higher specific stiffness. The manufacturing of the advanced mirror is only possible with an additive manufacturing process.

Chapter 5 provides a summary of the work along with the most recent findings and potential future work.

DEDICATION

I dedicate this dissertation to my wife, Lindsey Horvath, who has supported me throughout my entire graduate studies. Your patience, understanding, love, and willingness to listen kept me sane. I cannot thank you enough, Thank you. I also dedicate this to my son, Enzo. While you may not understand why "Daddy has to work?" so late at night and on the weekends yet, my hope is your life and path to a fulfilling career will be a little less tumultuous than mine. I love you both.

ACKNOWLEDGEMENTS

I first would like to acknowledge the role of my advisor, Matthew Davies, for his years of continued support, funding through CeFO projects, and willingness to allow me freedom to explore outside of project requirements. I also acknowledge my committee members Steve Patterson and Chris Evans, who provided countless hours of technical advice over many years and continually challenged me to understand first principles. I attribute my technical foundation and ability to think through a problem to them. Their perpetual influence is evident in most of my work. I would also like to acknowledge Scott Smith for the opportunity to finish my dissertation work at the Oak Ridge National Laboratory, which provided prodigious resources in both equipment and staff most graduate students will not experience. I also acknowledge faculty and staff at UNCC and specifically in the Center for Precision Metrology (CPM) for the technical conversations, lab space, equipment, training, and overall interest in my work. This includes, Jimmy Miller, Brian Dutterer, Geoff Heacock, Joe Dalton, Stuart Smith, Kosta Falaggis, Greg Caskey, and Scott Williams. Lastly, I would like to acknowledge many of my peers, most notably, the routinely attending members of the ASPE student chapter, Kumar Arumugam, Laura Hopper, Todd Noste, Masoud Arablu, Sam Ludwig, Jacob Cole, and Kristen Venditti, staff and students at the University of Rochester, Aaron Bauer and Eric Schiesser, and Duke Centennial Hall 110 office mates, Dustin Gurganus, Tyler Blankenship, Farid Javidpour, Jesse Grover, and Kang Ni, all of which provided perspective and a critical sounding board for technical innovations. This research was in part supported by the National Science Foundation I/UCRC Center for Freeform Optics. This research was also supported by the Department of Defense, Office of the Secretary of Defense and the Department of Energy, Office of Science, Office of Energy Efficiency and Renewable Energy, Office of Advanced Manufacturing, Energy and Transportation Science Division and used resources at the Manufacturing Demonstration Facility, a DOE-EERE User Facility

at Oak Ridge National Laboratory.

TABLE OF CONTENTS

LIST OF TABLES

LIST OF FIGURES

LIST OF SYMBOLS/ABBREVIATIONS

δ_q Peak to valley surface quilting deflection

δ_{RMS} Root mean square mirror self weight deflection

η Areal solidity ratio

κ Rib effectiveness factor

ν Poisson's ratio

ϕ Mirror diameter

ψ Azimuthal angle on mirror surface

ρ Material density

A Mirror area

B Inscribed cell diameter

d Depth of cut

E Modulus of elasticity

E' Specific grinding energy

f Feed per revolution

F_n Normal tool force

F_t Tangential tool force

F_w Axial tool force

h Overall mirror thickness

h_c Cell depth

r Mirror semi-diameter

s Tool stepover

t_f Facesheet thickness

t_w Rib/Web thickness

V_s Peripheral wheel speed

AM Additive manufacturing

CVD Chemical vapor deposition

CVI Chemical vapor infiltration

FE Finite element

MSF Midspatial frequencies

NA Neutral axis

PV Peak to valley

RMS Root mean square

S_q Areal root mean square of a surface measurement

SiC Silicon carbide

SPDT Single point diamond turning

TPMS Triply periodic minimal surface

CHAPTER 1: INTRODUCTION

With the advent of realizable freeform optics, a new standard for advanced imaging performance is pervasive in the photonics community. However, high-performance freeform optical systems, designed for broad spectral imaging from the visible to the far infrared, place new demands on optical design, precision manufacturing, and precision metrology. In this dissertation, four key aspects are addressed (i) precision placement of freeform optics, (ii) closed loop iterative manufacturing and metrology, (iii) advanced materials, and (iv) design for manufacture.

The near arbitrary shape of these optics introduces a series of challenges in manufacturing. Traditional spherical reflective optics can be fabricated by grinding and polishing systems that leverage the rotational invariance of the mirror shape with averaging methods and full aperture polishing. Freeform mirrors however require a manufacturing process with at minimum three degrees of freedom, along with a tool smaller than the aperture. Single point diamond turning machines, fast tool servos, and deterministic micro-grinding were enabling manufacturing technologies to realize freeform surfaces in a variety of optical materials [1, 2, 3, 4]. The advancement in manufacturing and the ability to realize new surface shapes allowed for innovation and flexibility for optical designers [5, 6]. This freedom in optical design has led to the development of multiple lab level imaging systems in both the infrared and visible spectrums [7, 8, 9, 10].

However, freeform optics additionally present a set of metrology challenges, where due to the rotationally varying terms ($z = f(r, \theta)$), classical optical figure metrology is often not acceptable—technically or economically—or realizable [11]. Due to the need for extra datums and specification of sub-micrometer accuracy, in-process metrology is

often completed on the manufacturing equipment to avoid errors in remounting after off machine metrology [12, 13]. Completing on-machine metrology does not account for systematic machine errors, such as straightness and squareness [14, 15]. While the systematic errors on an ultra-precision machine are often small and negligible, in particular on freeform optics with small clear aperture (≈10 mm) for use in the infrared. However, for larger freeform optics with a clear aperture in the range of 250 mm (or larger) intended for use in the visible spectrum, this is not the case.

Further, the sub-aperture manufacturing techniques required for freeforms drive manufacturing times higher and inherently introduce additional long term thermal drift and sometimes thermal cycling with error components not seen in smaller components [16]. Other contributions to figure error that must be considered are mounting stresses. Moreover, often the mounting on manufacturing and metrology platforms are different. Errors due to mounting stress will not be evident in on machine metrology and could be incorrectly compensated with an incorrect interpretation of off machine metrology. Chapter 2 addresses some of these concerns by creating a new kinematic mount system that is used through the entire process chain of surface manufacturing, iterative independent metrology, and system integrating. This is completed by a redefinable datum system to register the coordinate system of the optical surface in a common reference frame. Where the reference frame could not be physically transferred, the repeatability of the mount was quantified to provide the uncertainty for the location of the coordinate system of the mirror in the main reference system, thus allowing for uncertainty propagation through both the surface figure metrology and in the instrument if required. The system described provides a mirror mount design enabling a deterministic iterative manufacturing-metrology process chain.

Freeform mirrors with the clear aperture in the range of 250 mm are well suited for instruments used for surveillance and remote sensing. However, due to the harsh environmental conditions, such instruments can be introduced to, most reflective

optical materials would have severe deficiencies, thus reducing optical performance. For this reason, a candidate material often chosen for these applications is silicon carbide (SiC). Research using SiC as a mirror material was initiated during the Reagan administration's Strategic Defense Initiative (SDI) during the 1980s. The primary immediate application was for water-cooled optics, replacing molybdenum, copper, and tungsten carbide laser mirrors [17, 18]. However, a secondary application was presented as an alternative material to lightweight beryllium and glass reflective optics [19]. Due to shifts in defense programs, the primary focus for SiC turned to lightweight mirrors and optical support structures [20]. As the material manufacturing technology matured through the early 1990s for reaction bonded, hot pressed, and chemical vapor deposited SiC [21], optical designs for three mirror anastigmatic telescopes were beginning to emerge as functional telescopes with lightweight SIC mirrors [22, 23, 24, 25].

Silicon carbide is an advanced refractory ceramic with a high ratio of elastic modulus to density and a high ratio of thermal conductivity to thermal expansion. These properties result in a mirror that has high stiffness, low mass, and low thermal distortion, thus positioned as a leading candidate material for lightweight mirrors exposed to harsh conditions. However, ceramics such as SiC are primarily covalent materials with a low ratio of elastic modulus to hardness and a high ratio of shear modulus to bulk modulus, each corresponding to limited slip systems and brittle behavior. Thus, the same properties that make SiC desirable for imaging systems in harsh environments makes it difficult to manufacture.

SiC mirror preforms can be manufactured in a number of different ways, such as slip casting, hot isostatic pressing, reaction bonding, and chemical vapor deposition. Each process chain results in a material with various crystallographic orientation, grain size, residual porosity, and purity, thus affecting the thermo-mechanical properties. Additionally, the manufacturing methods for complex SiC preforms lend to

traditional techniques such as milling or die pressing. These traditional methods limit the geometry of the preform, thus limiting the design space for the mirror. For this reason, since the inception of silicon carbide lightweight mirrors, some form of the isogrid supported design has dominated the industry.

The introduction of additive manufacturing is a disruptive technology in the advanced manufacturing portfolio and is often mentioned as the leading process chain for the next industrial revolution. The use of additive manufacturing in ceramic materials, is an enabling technology for the creation of complex components, otherwise not possible. However, additive manufacturing of ceramics has seldom resulted in full density monolithic structures, which has deleterious effects on the thermomechanical properties of the material, lending to sparse usage in high-risk components [26]. To address this issue, driven by the most stringent requirements—nuclear power applications—a new method of producing near arbitrary monolithic components in SiC with high purity by additive manufacturing was developed by Terrani et al. [27]. Here, the process chain includes an additive manufacturing step to create a base geometry with an intentional high porosity, followed by a gaseous phase infiltration of the base material, resulting in near full density material. Leveraging this work, new component designs and system configurations in SiC could be accomplished, thus the use of the material for reflective optics is of great interest. However, this new process chain also results in a new material microstructure. Foundational work on the post processing of this material was required to quantify if the surface quality could achieve a specular finish suitable for the use as reflective optics. This heterogeneous material, comprised of α-SiC particles in a dominant β-phase SiC matrix with a nanocrystalline microstructure, develops a homogeneous outer layer of β-phase SiC during the infiltration process. Thus, a series of grinding experiments were performed in Chapter 3 to quantify both, the manufacturability of this new material compared to traditional CVD-SiC, and the surface quality for use in reflective optics.

Mentioned, the genesis of lightweight silicon carbide mirrors was driven by mass reduction, stiffness, and thermal stability compared to glass and beryllium [19, 28]. Moreover, the demand for lightweight mirrors in general, is omnipresent in every decade since the introduction of advanced all-reflective imaging systems. Over this time, the shapes of the optical surfaces have evolved, from spheres to conics to freeform, each improving image quality over the previous. Further, the advancement in SiC material quality and production has increased, thus reducing lead times and developing mirror surfaces with sub-nanometer level roughness [29]. However, the design of the isogrid support structure has had a near stagnate geometry since the 200" Hale primary mirror for the Palomar observatory in 1949 [30]. The isogrid design exists not as optimal design, but as a design that is readily manufactured. Even with recent manufacturing advancements, including additive manufacturing and topology optimizations, the designs remaining dominated by 2-D isogrids. Kishner et al. provides figures of merit for lightweight mirrors and shows the standard isogrid design at that time for silicon carbide mirrors in 1990 [19]. In 1995, another design is shown with a square unit cell isogrid with a reaction bonded closed backsheet [23]. Papenburg et al. introduced an innovation with carbon fiber reinforced silicon carbide (C/SiC) in 1999, yet the mirror preform was milled in the green state with a square open back isogrid design [31]. Xuejun et al. in 2005 [32], Robichaud et al. in 2012, [33], Ding et al. in 2019 [34] and even additively manufactured SiC mirrors in 2020 [35], all showing some form of isogrid design utilizing 3 basic 2-D structures, the triangular, square, and hexagonal (referred as a honeycomb).

These nearing 80-year-old lightweight mirror designs are outdated and maintain a consistent problem well known in the industry of surface print through from the isogrid structure [36], occurring still in the most advanced imaging systems ever created, such as the James Webb Space Telescope [37, 38]. The intrinsic issue with the isogrid design is a fundamental coupled design trade-off. To reduce the mass of the mirror,

the isogrid cell size must increase and/or the facesheet thickness decrease. However, to reduce the print through, the facesheet must either increase in thickness or the isogrid cell size be reduced. The literature history for lightweight mirrors provides two key pieces of information: there has been demand with little sign of slowing for lightweight mirrors and the mirrors required must be lighter, stiffer, and overall better, in particular, in pursuit of shorter wavelength imaging systems. Thus, the design of the mirror preform, considering recent advancements in state of the art manufacturing, is ripe for innovation.

Considering the enabling work for SiC preforms in Chapter 3, and the decades of history requiring lighter, stiffer, and overall better mirrors, the lightweight mirror design was revisited. Further, while fundamental research has been published on aspects of mirror design, the literature lacks a comprehensive design methodology for these mirrors, hence the wide distribution of mirror isogrid designs and techniques shown in literature. Thus, Chapter 4 provides both, a systematic design framework for the traditional lightweight isogrid mirrors and provides a new systematic design methodology for a lightweight mirror design that has a higher specific stiffness, lower areal mass density, and an order of magnitude reduction in surface print through, resulting in a higher efficiency lightweight mirror. Chapter 4 provides a significant contribution to the optomechanical design engineering community for both, traditional lightweight mirror design and the emergence of a paradigm shift for new lightweight mirror designs.

Freeform optics, additive manufacturing, and silicon carbide mirrors are disruptive technologies independently. The work described in this dissertation merges these disruptive technologies into a systematic framework that has the potential to revolutionize both the manufacturing process chain and the mechanical design of lightweight mirrors. The combination of the three papers of this dissertation lays foundational work in reflective optics for overcoming manufacturing challenges, and for advancing

mechanical design in consideration of advanced manufacturing. The result is a significant advancement in the state of the art for creation of silicon carbide, additively manufactured, high efficiency, freeform reflective optics.

CHAPTER 2: KINEMATIC MIRROR MOUNT DESIGN FOR ULTRA-PRECISION MANUFACTURING, METROLOGY, AND SYSTEM LEVEL INTEGRATION FOR HIGH PERFORMANCE VISIBLE SPECTRUM IMAGING SYSTEMS

2.1 Introduction

High performance visible spectrum optical systems that operate in a variety of changing conditions require a deterministic approach to the design and manufacture of each critical component. The use of freeform optics can reduce overall volume while maintaining performance [39], with the trade-off of increased sensitivity and tighter tolerances. Freeform surfaces also require sub aperture manufacturing processes such as single point diamond turning (SPDT), magnetorheological finishing (MRF), and deterministic micro-grinding. These processes produce error patterns, typically manifesting as waviness or mid-spatial frequencies, that are not typically seen in traditional optics manufacturing. Further, freeform metrology platforms with uncertainties less than the manufacturing platform are needed to correct and validate optical components [11]. Thus, the use of freeforms introduces new challenges that must be dealt with in the manufacturing-metrology loop.

Ideally, a feedback loop between metrology and manufacturing is implemented to determine when the process has reached figure convergence, and an independent metrology platform is used to validate the results [16]. In order to appropriately measure the figure of the optic, reference features such as datums and fiducials are required to establish a local coordinate system. These reference features must not only be realizable in manufacturing and metrology but also at the system level. During assembly and optical testing, datums and fiducials allow the measurable positioning

of each optic relative to the previous in all six degrees of freedom with controlled tolerances. In this Chapter, we focus on the design for manufacture and metrology, but recognize that for high performance optical systems, datums and fiducials must also be realizable during assembly and testing. Thus, the mechanical interface described in this Chapter is designed not only to provide a common interface between manufacturing and metrology platforms, but also to provide a high precision interface between each optic and the system housing.

Tolerances in freeform optical systems are demanding and meeting them requires and iterative process to mitigate the effects of machine motion and thermal errors in ultraprecision manufacturing equipment. During the in-process iterative feedback loop between manufacturing and metrology, the optic must be repeatedly remounted on the manufacturing and metrology equipment with sub-micrometer level positioning accuracy, typically requiring custom fixturing [12]. In order to achieve figure accuracy, the mounting stresses and associated deformations must also be minimized. Exact constraint designs, such as a kinematic mount or kinematic coupling [40], is a well-known technique for mounting components that achieves these goals.

In an exact constraint design, the number of constraints equal the number of rigid-body degrees of freedom in a system. An example is the three ball, three vee groove kinematic coupling [41]. If the contact interfaces are assumed to be point contacts with zero friction, then a theoretical perfect constraint with perfect position repeatability is obtained. However, in reality deformations and friction exist at the interfaces, and because the size and shape of the contact patches are functions of the contact forces, both coupling stiffness and repeatability will also be a function of loading conditions. Using Hertzian contact theory, one can model each constraint location to determine the displacement, stiffness, and stress at the mounting interface as a function of preload. From this, the joint compliance as a function of loads coming from both preload and process load can be determined.

A common trade off in an exact constraint mount is that increased load capacity typically leads to degraded positioning repeatability. Several designs have been developed to balance this trade off. Culpepper described a quasi kinematic coupling with a theoretical line contact at the interfaces. This design provided a moderate load capacity with 0.5 µm repeatability at relatively low cost [42]. An alternate approach was discussed by Willoughby [43] and Slocum [41] to provide a large load support while maintaining a near point contact and associated repeatability. In this approach, two sections of a sphere are joined to produce a "canoe ball" or canoe. When interfaced with a vee the deformations of the canoe result in a high aspect ratio elliptical contact patch, effectively distributing the load to reduce the risk of plastic deformation while maintaining sub-micron repeatability. A drawback with this design is the cost of the canoe shaped component which is manufactured with a high precision contouring grinder [43]. Coupling repeatability has been covered both analytically and experimentally for many designs, some of which show the direct effect of preload on system repeatability [44, 40, 43].

In the present work, the authors detail the design of a kinematic mount that maintains position repeatability suitable for the manufacture of freeform optics while supporting the loads expected in precision manufacturing. The design has several advantages over others previously reported [45, 41, 46, 47, 48]. First, it does not require expensive strict tolerances on the kinematic mount components themselves [49]. Second, it provides moderate load support, and third, it is demonstrated to have submicron repeatability. The design leverages some previous work in the field, specifically the understanding of effective groove angle and its effect on repeatability due to friction and preload [44]. A primary goal of the design is to maintain a minimum stiffness during single point diamond turning (SPDT) or deterministic micro-grinding while simultaneously maintaining sub-micrometer positioning repeatability. This Chapter describes the design, analysis, and experimental performance of the kinematic cou-

pling. Through modeling the effect of process forces on stiffness is predicted and used to set the preload forces to maintain the stiffness at a desired level. The mount utilizes a novel torsional preload produced magnetically and is suitable for rapid mounting and dismounting on metrology and manufacturing platforms, thus closing the manufacturing and metrology loop needed for the deterministic manufacture of freeform optics.

2.2 Mount Design

2.2.1 System and Mount Load Conditions

The mirror mount design is driven by a diffraction limited off-axis multi-mirror visible spectrum imaging system with a set of specific load cases [50]. During operation, the instrument will experience temperature variation, must operate in arbitrary orientations, and survive high-g accelerations in any orientation. The surface figure error on the mirror must be less than 100 nm RMS during operation to maintain performance. While the design of the lightweighted mirror to maintain this performance is out of the scope of this document, the constraint design and overview of the mirror assembly is shown. In order to meet the required specification of the instrument, the final mirrors will be made in silicon carbide (SiC) with a CVD SiC cladding on the optical surface.

To generate the freeform surface in SiC, a process known as deterministic microgrinding must be used [4]. During this process, a diamond grit resin-bonded grinding wheel is used to grind the surface with depths of cuts on the order of 1 µm during finishing operations. This document is constrained to showing the aluminum prototypes of the mirrors, which are direct replicas of the SiC mirrors, with a nickel phosphorus coating for diamond turning.

Along with the system level load cases, manufacturing and metrology of the mirrors impose load conditions and constraints. Considering the manufacture and metrology as part of the load conditions, then some additional drivers are identified as reduced

packaging, robustness, manufacturing forces, accessible datums, and sub-micrometer position repeatablity. For this reason, the effect from the process force magnitudes during manufacturing were modelled to verify the stiffness of the mount. Also, the design details how a definable coordinate system was created for the optical surface that can be transferred between the manufacturing platform, metrology, and then integrated into the instrument.

2.2.2 Mount Configuration

An optic is paired with an optical cell, whose design is used for both the manufacturing mount and application mount. The optical cell has the appropriate reference datums to establish a coordinate system for the optic. These datums also act as the mating interface features at the system-level. The optic is installed on a set of kinematic mounts, allowing for removal of the optic for in-process intermittent metrology. Stated in Sec. 2.1, to meet the figure tolerance of the optical prescription, the mirror would have to be manufactured and then measured on separate metrology equipment. Therefore, there is an uncertainty in the position of the optic relative to the optical cell which can affect performance of the instrument after completion of the optical surface. The system-level error budget for the instrument accounted for the peak to valley repeatability targets, initially 1 µm for the linear degrees of freedom (x, y, z) and 10 µrad for the rotational degrees of freedom (ϵ_x, ϵ_y).

The design of the mount comprises three identical kinematic joints, equally-spaced on a circle, at 66 percent the diameter of the optic. Equally-spaced identical joints provide an athermal mount configuration, where a change in temperature will allow for a nominally uniform change in size while maintaining position of the vertex. The exact constraint design reduces the risk of optical surface deformation from external forces, where the errors will largely be rigid body motions of the optic.

Each joint is rotated 90 degrees about the coupling angle bisectors and provides constraint in the axial and azimuthal directions, requiring a torsional preload, Fig. 2.1.

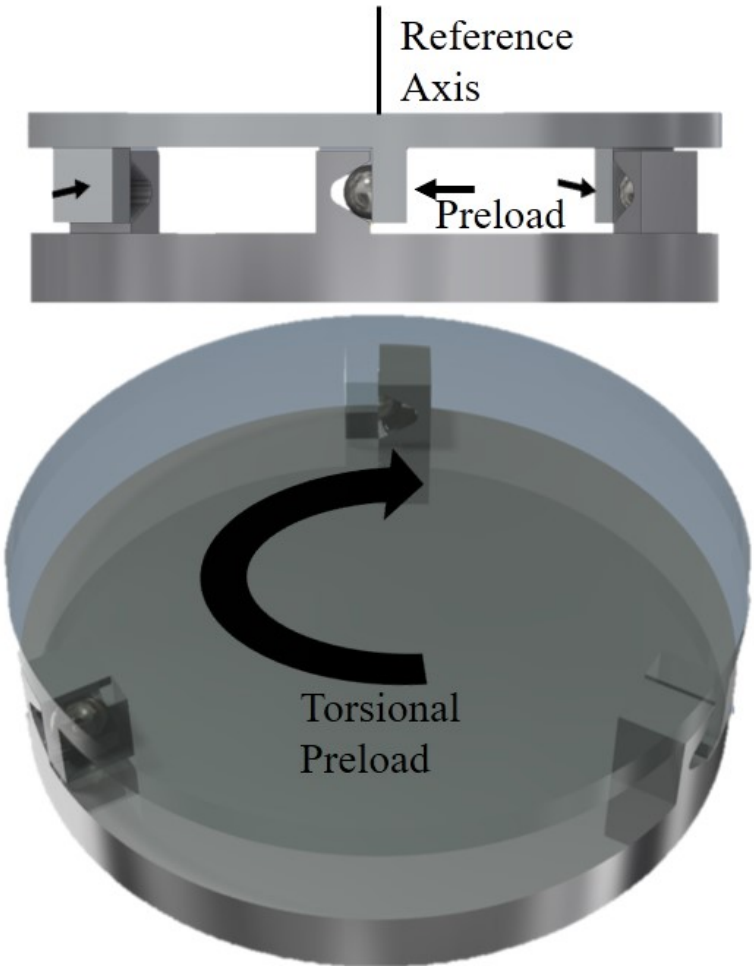

Figure 2.1: A generic representation of a torsionally preloaded kinematic coupling, with the mounting locations shown near the diameter for clarity.

The bisector represents a degree of freedom, thus rotation of each joint will still maintain an exact constraint configuration. This technique of rotating a groove or set of grooves about the bisector has been shown by Slocum generically for a vertical configuration [41] and by Hale on the National Ignition Facility at Lawrence Livermore National Lab mirror mounts [48]. While groove rotations to support a mirror for a vertical configuration has been shown, to the author's knowledge, this Chapter is the first to detail a design and prototype for a torsionally preloaded kinematic mirror mount.

In this configuration, the preload direction is perpendicular to the reference axis of

the optic, requiring a rotation of the optic to seat the mount. Preload in each joint is set by a permanent magnet with an adjustment to change distance between the magnet and mating component. Fig. 2.2 shows the final design of the optic, paired with the optical cell, and kinematic mount assembly. The novelty of this design is two fold, where the configuration intrinsically reduces the concern of the mirror decoupling from the optical cell due to an arbitrary gravity vector, thus, satisfying the high-g survival load condition. Also, during manufacturing, the normal force from the rake face of the diamond turning tool or the feed direction during micro grinding is in the same direction as the preload force, therefore nominally increasing the stiffness of the mount.

2.2.3 Manufacturing Configuration

The optical cell is mounted to the spindle nose of the ultra precision diamond turning machine. To create a measurable coordinate system on the optical cell, the central bore inside the flange and three interface pads are single point diamond turned, defining the z-axis and origin, and rotations about the x-axis and y-axis. The optical cell is rotated by the spindle to align the freeform prescription. Precision bores are diamond milled in the optical cell along a defined axis of the prescription, which completes the datum definition of all 6 degrees of freedom for the optical cell. The three pads and two precision bores are later used for locating the optical cell and optic into the global coordinate system of the imaging instrument.

The optic is installed on the kinematic mount and the diameter and a freeform orientation flat are SPDT or ground. The purpose of the defined diameter and orientation flat are for coarse optic alignment on separate metrology equipment for initial figure measurement. The optical surface is manufactured in coordinated axis mode (c-x-z) with the vertex of the optic set as an integer number of millimeters from the 3 diamond turned pads on the optical cell. Once the final pass on the optical surface is completed, the 3 pads on the optical cell are recut to set the axial distance of the

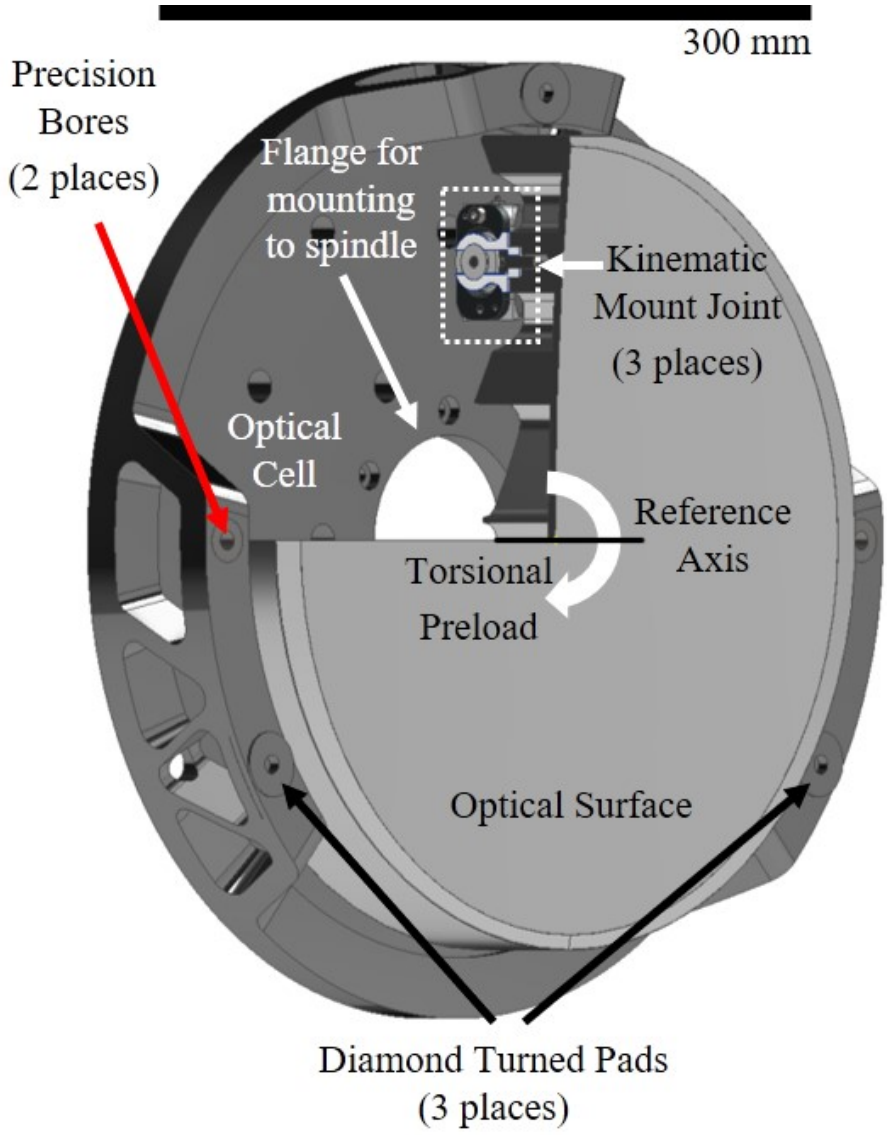

Figure 2.2: The optical cell comprises a flange that mounts the optical cell to the spindle nose of the diamond turning machine. The optic is installed in the optical cell by a torsionally preloaded kinematic mount and the freeform optical surface is diamond turned in coordinated axis mode. Three pads and two bores on the optical cell are diamond turned and milled, respectively, to establish a coordinate system on the optical cell. The coordinate system of the optic and freeform optical surface is relative to the optical cell. The three pads and two precision bores locate the optical cell, and therefore the optical surface, into the global coordinate system of the imaging instrument.

optic relative to the optical cell. This technique removes the initial postion offsets present from the kinematic mount assembly, pairing the optic and optical cell for life. The completion of this process results in a fully definable coordinate system for the optical surface, with the optical cell as the reference.

The optic is then removed from the kinematic mount and the optical cell remains on the spindle of the diamond turning machine. The optic is installed on a matched kinematic mount on a separate machine for figure metrology. For this stage of metrology, the references required are only the turned diameter and orientation flat. Piston and tilt errors from the metrology mount can be removed during data processing. If the figure tolerance is not met, the optic is reinstalled in the optical cell on the manufacturing platform and is corrected. This process redefines the 3 pad reference features at each iteration until figure convergence is achieved. Once figure specification is met, the optical surface location uncertainty relative to the optical cell, is given by the uncertainty in the repeatability of the kinematic mount, which was quantified and documented in this Chapter.

2.2.4 Description of Components

The kinematic mount plane was designed near the shear plane of an lightweighted optic, shown in Fig. 2.3. This reduces angular effects at the optical surface from arbitrary gravity loading orientations and forces during manufacturing. It also reduces the bending moment due to friction in the joint. Fig. 2.3 also shows the location of an eccentric pin that changes the gap of the magnetic preload. The pin access allows for easy preload adjustment in any configuration. When the magnet is at the maximum gap distance, the preload force is approximately 5 N per joint, holding the optic in place until the user rotates it out of the seat. A joint from the prototype kinematic mount installed on the optic is shown in Fig. 2.4.

Figure 2.5 contains the component details of one kinematic joint. Component 1 is an ogive with a 100 mm radius at the mating interface in one cross section and a

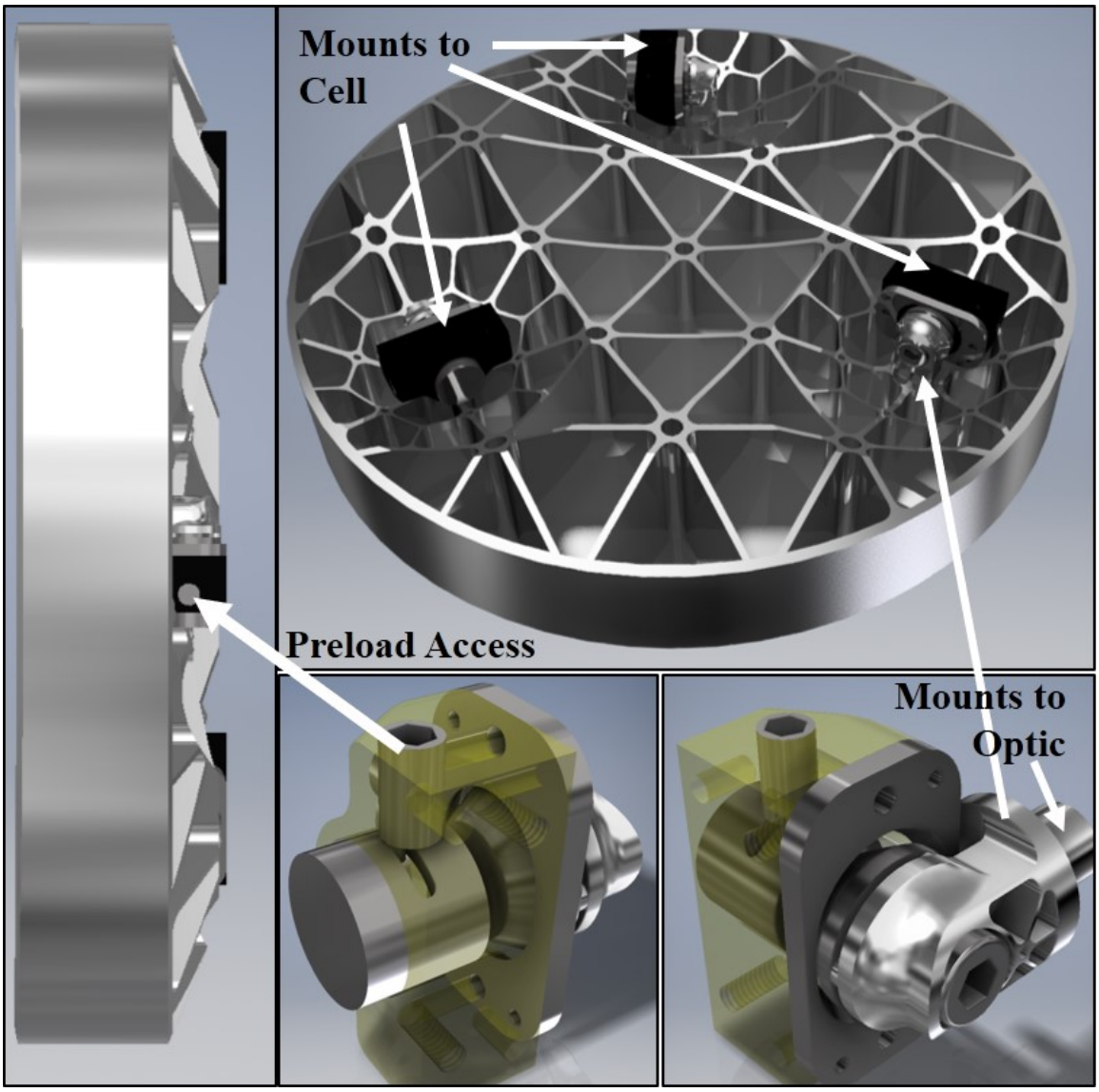

Figure 2.3: Model of lightweighted optic with kinematic joints installed. The joints are also shown, one component transparent to show internal detail of component interactions.

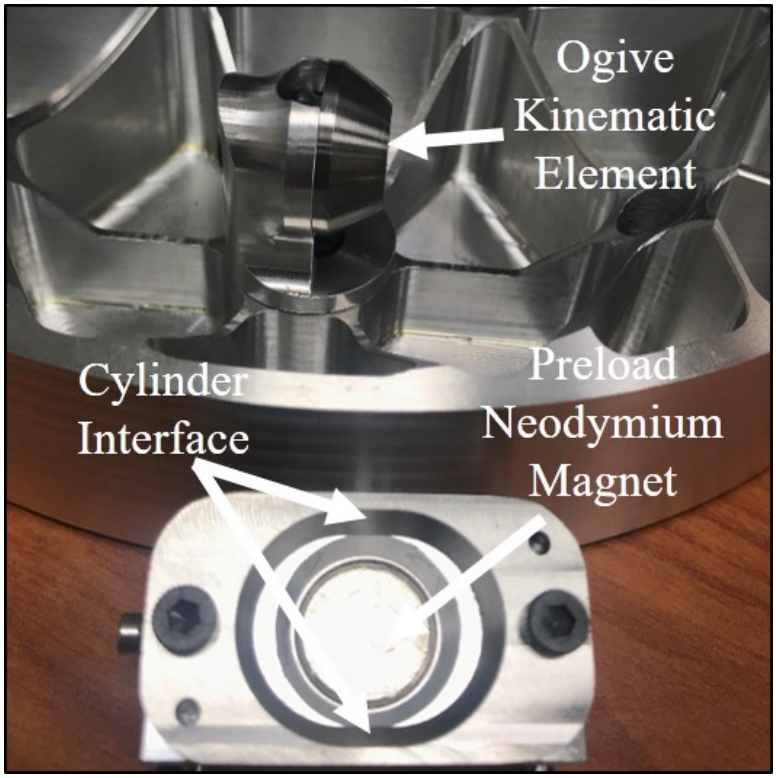

Figure 2.4: Prototype Kinematic joint disconnected

9 mm radius in a perpendicular cross section. Component 2 is a truncated cylinder pair with a 50 mm radius. The design creates an elliptical contact patch, distributing the load and reducing the contact stresses. The details of the interface are shown in Table. 2.1 and the general description is shown in Fig. 2.6.

The design of the geometry allowed for a traditional manufacturing process, where component 1 was turned on a Milltronics CNC Lathe and Component 2 was ground flat and machined on a Makino A51 CNC Mill, after which the groove was lightly

Table 2.1: Kinematic mount component contact details with an effective groove angle of 58° and a preload of 65 N

	Component 1	Component 2
Radius	$R_{xx} = 100$ mm	$R_{xx} = 50$ mm
Radius	$R_{yy} = 9$ mm	$R_{yy} =$ infinity
Contact Patch Dimensions	183 µm x 78 µm	183 µm x 78 µm
Max Pressure	533 MPa	533 MPa
Max Shear	105 MPa	105 MPa

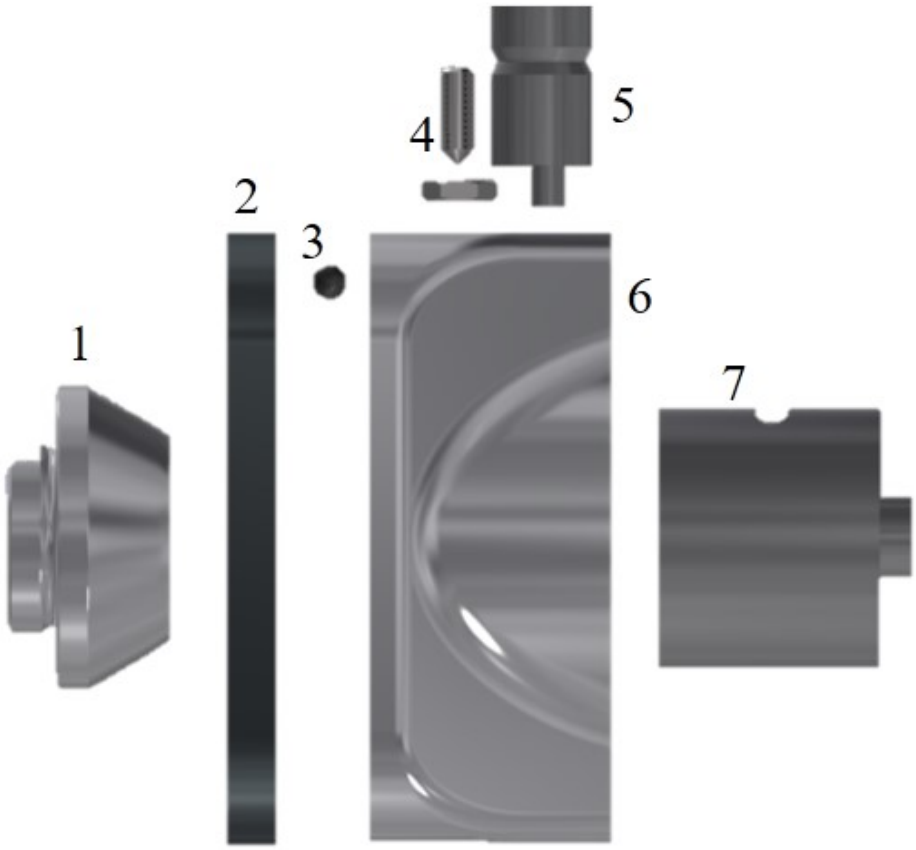

Figure 2.5: Component detailed view

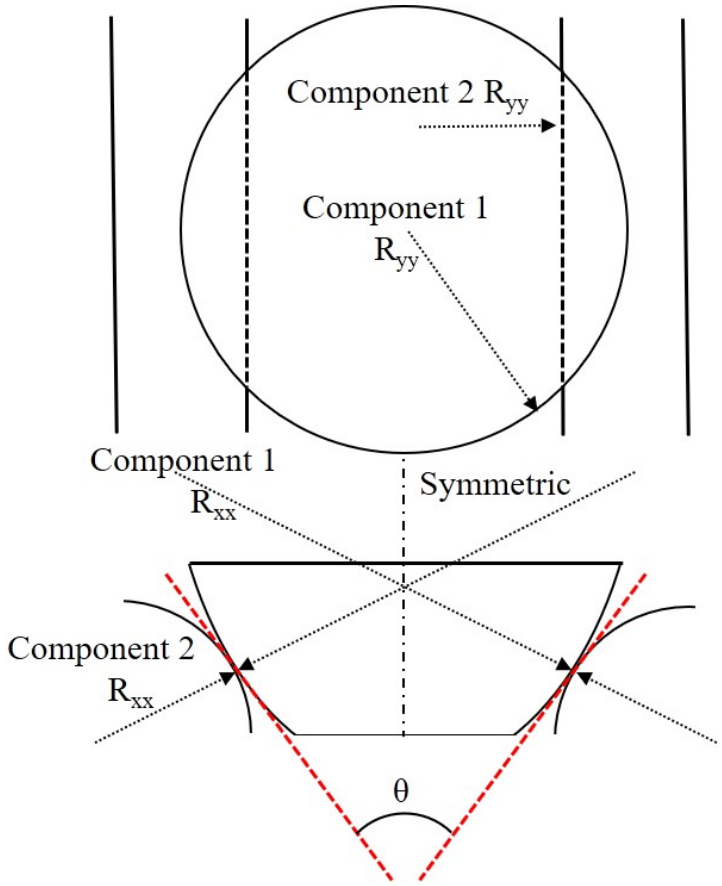

Figure 2.6: Schematic representation of the interface between Component 1 and Component 2

burnished. The material used for both components was 17-4 PH stainless steel.

Component 3 - 7 provide the mechanics for the joint. Components 5 and 7 are inserted into Component 6, Component 5 fitting into a slot of Component 7. Components 3 and 4 constrain Component 5 from being removed from Component 6 yet allowing a rotational degree of freedom. Rotation of component 5 will cause a linear translation of Component 7. The translation changes the gap between the magnet in component 7 and the face of Component 1. The maximum force in this system is applied when component 7 rests on the seat in Component 6. Component 1 mounts to the optic and Component 6 mounts to the optical cell. Because the optic is initially manufactured to a near net shape and requires post processing once combined as an assembly with the optical cell, each Component, including the optic and optical cell only required standard machining tolerances, on the order of 100 µm.

2.2.5 Coupling Stiffness

The stiffness of the mount is a function of the loading force applied to each joint. The loading force comes from the preload and, in manufacturing, is also affected by process forces. Therefore, it is important to understand how the process forces affect the "net preload" and hence the stiffness of each joint. To do this, we apply tangential and normal process force components, F_t and F_n on the optical surface, project the forces into the kinematic mount grooves and look at the effect of force location on the net preload, and therefore stiffness. While the magnitudes of the process forces for diamond turning and micro-grinding will differ, the force component model will hold true for both.

The general case for two deformable bodies in contact was used to calculate the deflection, the contact patch size, and the stress [51]. The slope of the deflection as a function of preload determined the stiffness and compliance curves of the contact patch, Eq. 2.1 and Eq. 2.2:

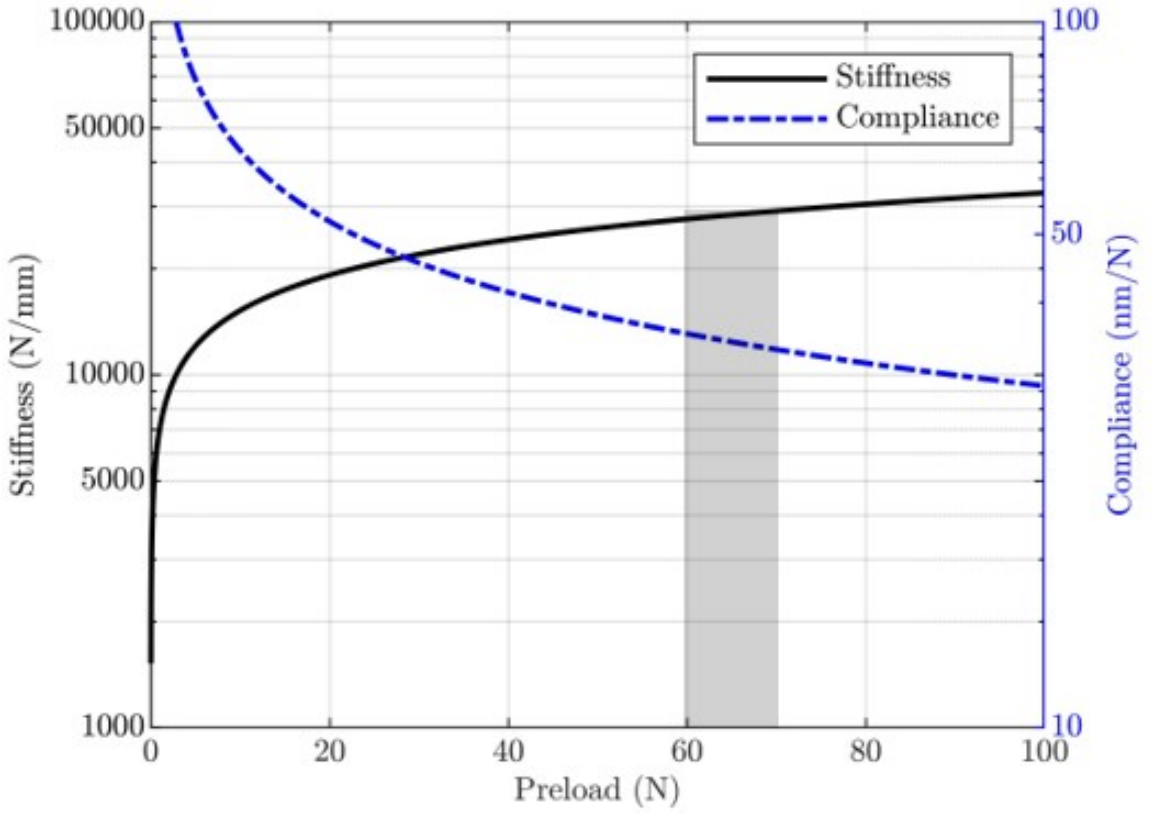

Figure 2.7: Stiffness and compliance curves of one contact patch. Each kinematic joint has a preload between 60 N - 70 N

$$\delta(P) = \lambda \sqrt[3]{\frac{P^2 C_e^2}{R_e}} \tag{2.1}$$

$$c(P) = \frac{1}{k(P)} = \frac{2\lambda}{3P} \sqrt[3]{\frac{P^2 C_e^2}{R_e}}. \tag{2.2}$$

Here P is the groove normal component of the preload force, R_e is effective radius, C_e is the reciprocal of equivalent modulus, and λ is the Hertz coefficient with respect to the angle between the normal planes. Fig. 2.7 shows the stiffness and compliance curves for the mount as designed.

The mount was designed to have a maximum compliance at each joint during manufacturing of $65\,\mathrm{nm\,N^{-1}}$ at any radial or azimuthal location on the optical surface.

During manufacturing, the tangential cutting force, which is calculated by a cutting coefficient and the chip area, shown in Eq. 2.3 is parallel to the preload force:

$$F_t = k_t f d, \tag{2.3}$$

where k_t is tangential specific cutting energy, f is feed per revolution, and d is depth of cut. The process forces are projected into the grooves of the kinematic mount, thus, the forces have a direct effect on the preload and stiffness of the joint. A diagram of the parallel forces are shown in Fig. 2.8. The preload vector is oriented in the same direction as the cutting force to nominally sum the forces as a function of azimuthal angle. Equations 2.4-2.6 represent the change in effective preload due to the tangential tool force as a function of the position on the optical surface, at which the cutting force is applied:

$$F_{J1}(r, \phi) = \frac{F_t r}{3L}(1 + 2\sin(\phi)) \tag{2.4}$$

$$F_{J2}(r, \phi) = \frac{F_t r}{3L}(1 - \sin(\phi) - \sqrt{3}\cos(\phi)) \tag{2.5}$$

$$F_{J3}(r, \phi) = \frac{F_t r}{3L}(1 - \sin(\phi) + \sqrt{3}\cos(\phi)). \tag{2.6}$$

Here L is radius of the kinematic mount circle, r is radial distance from the coupling centroid, and ϕ is azimuthal angle about the coupling centroid.

Figure 2.9 shows the result of the change in preload due to a 1 N cutting force at each of the 3 joints as a function of azimuthal angle and radius, noting that the radius of force application may be greater than the radius of the coupling. The phase shift between the angle at which the peaks occur is 120°, equal to the angular separation between the coupling joints. When the cutting force is directly over one joint, the reaction force is maximum and the force at the other joints become zero.

The change in preload as a function of radius and angle is expanded into normal

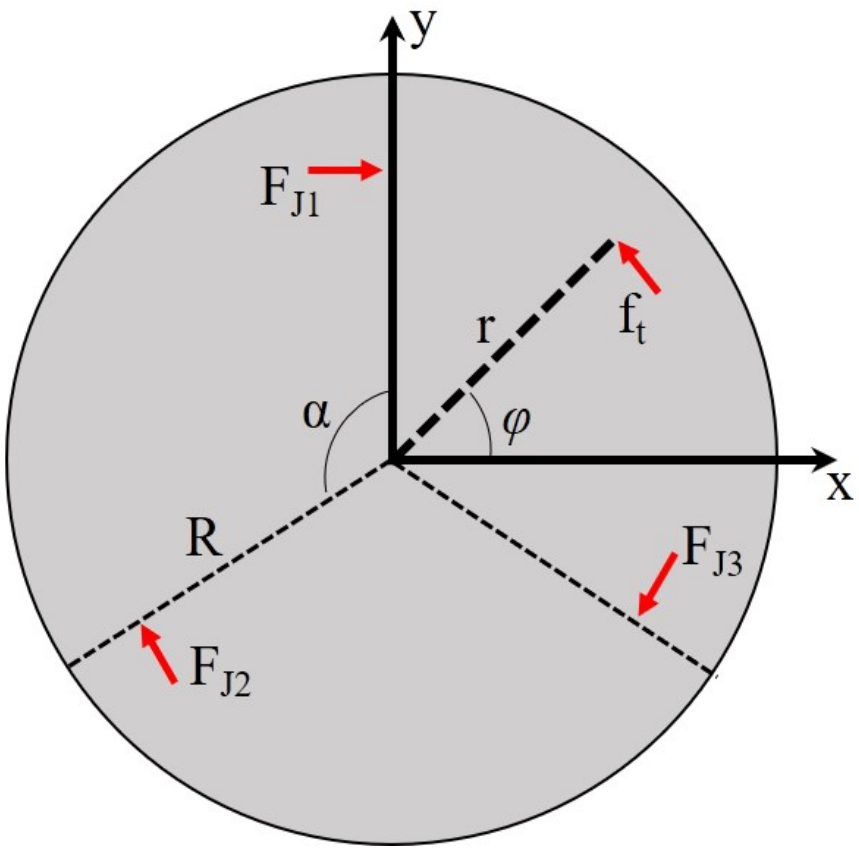

Figure 2.8: A freebody diagram of the tangential tool force and the reaction forces at each kinematic joint. R is the radius of the optic, ϕ is the angle of the tool force projected from the x-axis, and α is the angle between kinematic joints, which is set to 120°.

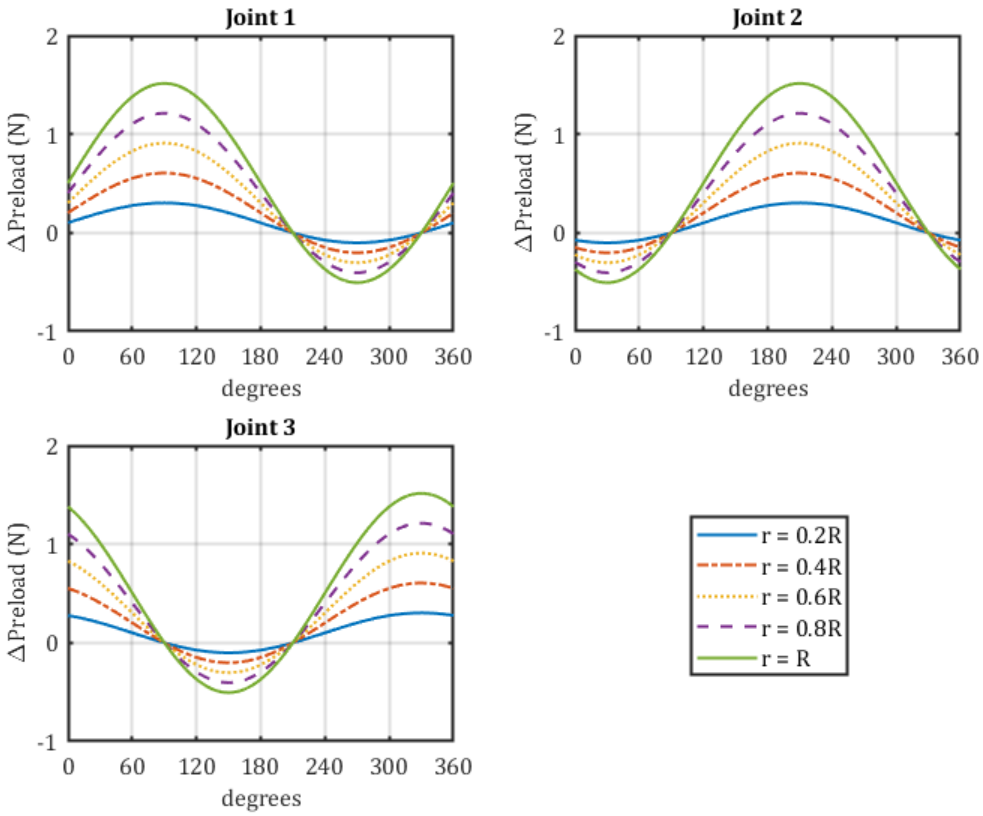

Figure 2.9: Change in preload (F_{Ji}) due to cutting forces as a function of radius and azimuthal angle ϕ. R is the radius of the optic

components of the groove for each joint. Considering the force normal to the optical surface is a fraction of the tangential component,

$$F_n = k_n f d \approx \mu F_t, \tag{2.7}$$

the change in reaction forces at each groove normal is found in Eq. 2.8 and Eq. 2.9:

$$F_{G1_i}(r,\phi)_{i=1,2,3} = F_{Ji}\frac{\cos(\theta) - \mu\sin(\theta)}{\sin(2\theta)} \tag{2.8}$$

$$F_{G2_i}(r,\phi)_{i=1,2,3} = F_{Ji}\frac{\cos(\theta) + \mu\sin(\theta)}{\sin(2\theta)}. \tag{2.9}$$

Here F_{Ji} is the magnitude of the of the resolved force at each joint and θ is the half angle of the joint vee groove.

Figure 2.10 shows the result of the reaction forces from Eqs. 2.8 and 2.9. The lower groove (groove 2 in Fig. 2.10) has a higher reaction force than the upper groove due to the 90 degree rotation of the joints. These force changes can be substituted into Eq. 2.1 or 2.2 as a δP to calculate the positional change of the ball or the change in joint stiffness. The maximum reduction in stiffness occurs when the tool position is directly between two grooves. At this position, the preload is reduced 0.6 the resolved force at the groove, 180 degrees from the tool. The mount maintains compliance specification for a resolved tool force up to 70 N.

2.3 Repeatability Testing

2.3.1 Metrology Setup

Five capacitance gauges were used to measure the repeatability of the mount in the three linear and two rotational degrees of freedom. A Lion Precision Elite Series MM190 capacitance gauge system was used to record the measurements. The capacitance gauges have a resolution of 10 nm. Two gauges were placed in plane of the mount to measure $x - y$ position. Three gauges were placed underneath the mount,

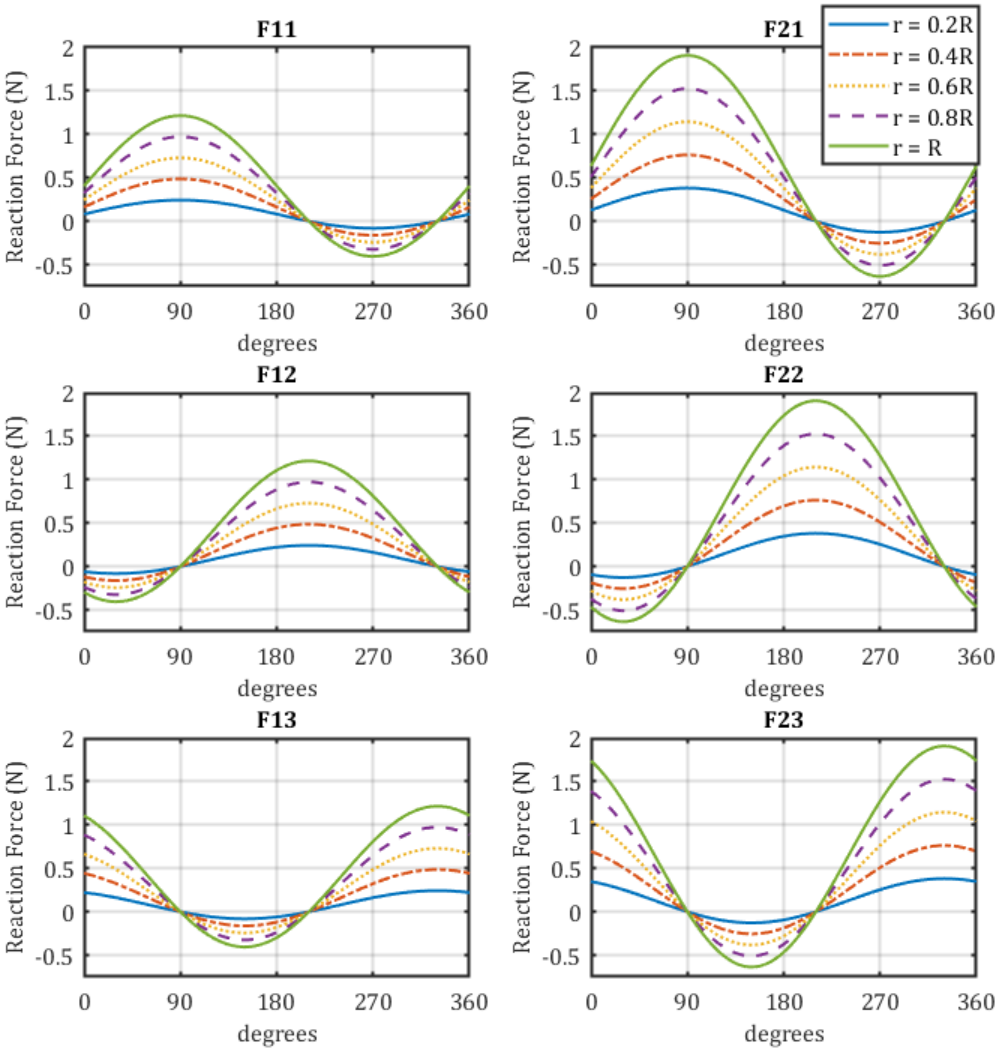

Figure 2.10: Groove normal reaction forces due to cutting forces as a function of radius and azimuthal angle ϕ ($F_{ij} : i$ =groove number, j =joint number)

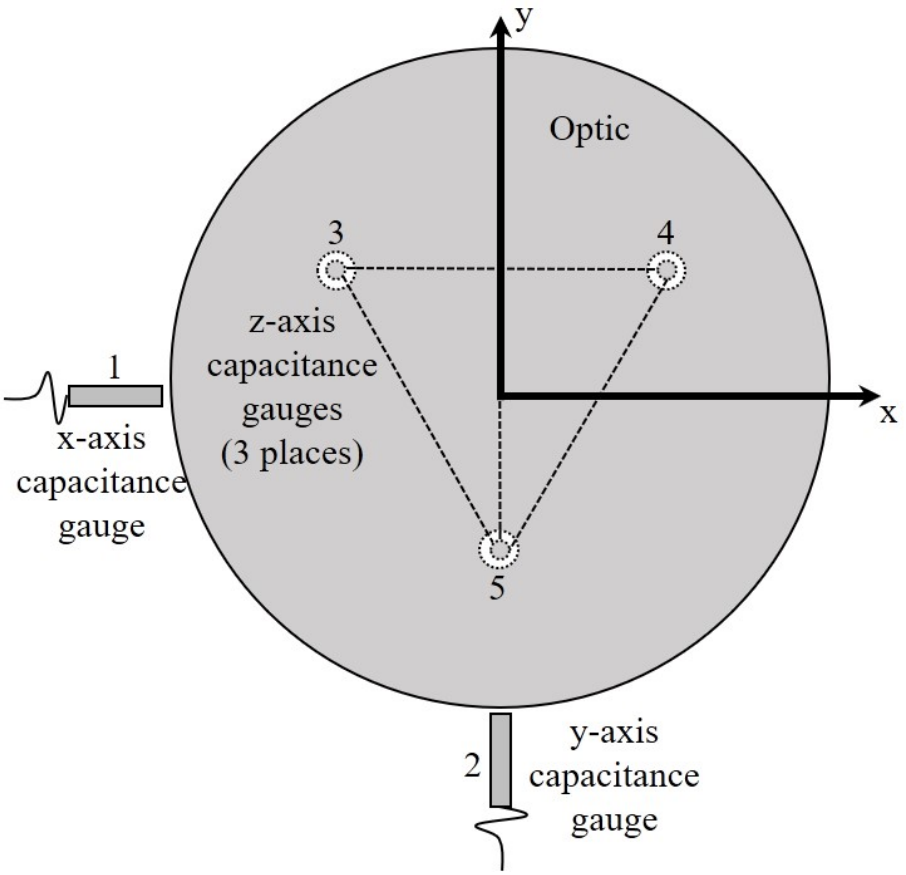

Figure 2.11: A representation of the metrology configuration, where gauges 1 and 2 provide measurements for in-plane (x-y) radial positioning. The average of gauges 3, 4, and 5 provide the axial (z) positioning. Readings from gauges 3 and 4 and the distance between them, with a small angle approximation, provide rotation about the y-axis. The average of 3 and 4 with the reading from 5 and the distance of the bisector provides the rotation about the x-axis.

equilaterally spaced, allowing for axial and angular measurements. A schematic representation of the metrology loop is shown in Fig. 2.11. Fixturing was designed and fabricated out of MIC6 tooling plate to hold the five capacitance gauges, shown in Fig. 2.12.

The test artifact was a 270 mm aluminum optic, prior to diamond turning. Temperature sensors were placed on the outer diameter of the test artifact and fixturing. The measurements were performed on an optical bench in a temperature controlled lab with temperature stability of 0.1 °C. The metrology loop was checked for hysteresis

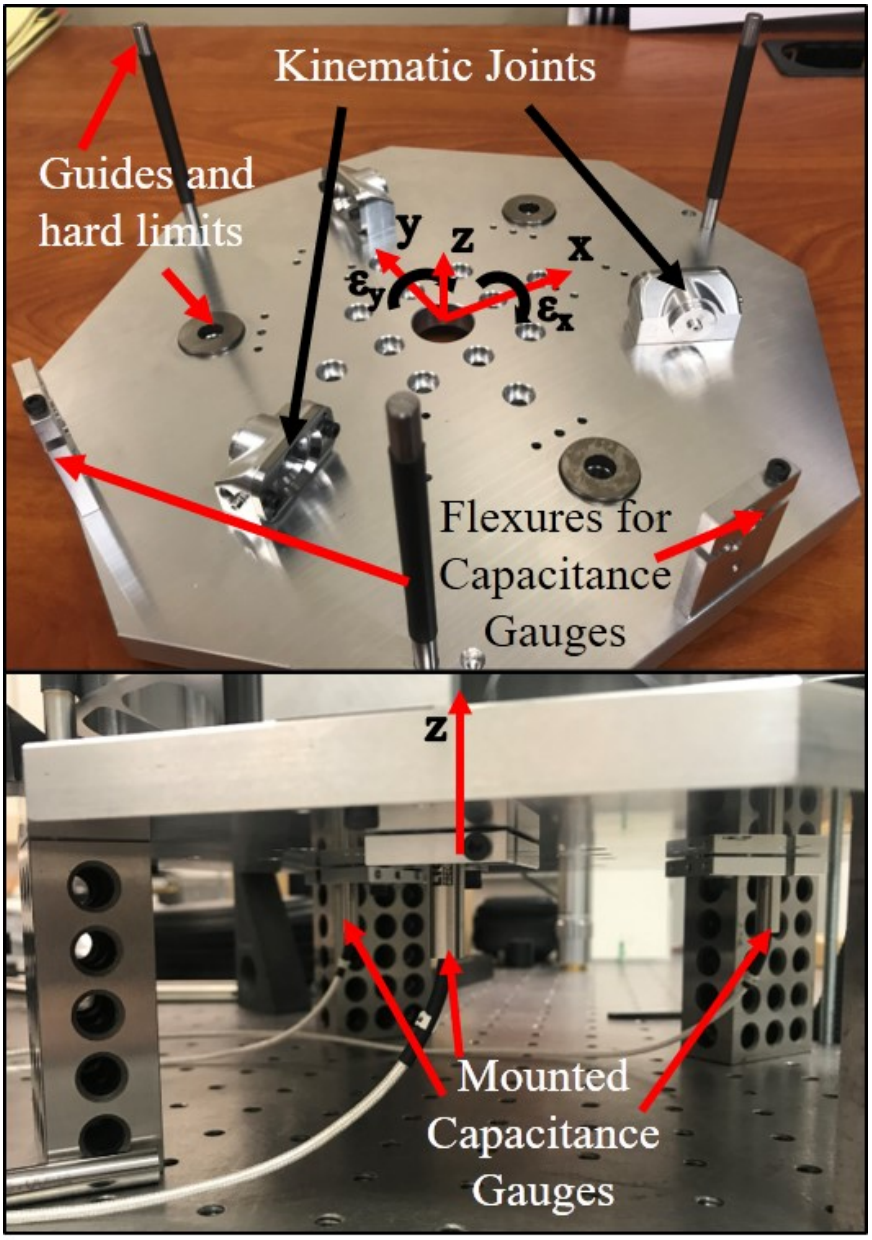

Figure 2.12: The metrology frame, which contains five capacitance gauge flexure mounts and safety limits. The guide rails on the fixture and hard washer limits above the axial gauges, ensured the optic would not touch the capacitance probes during the installation.

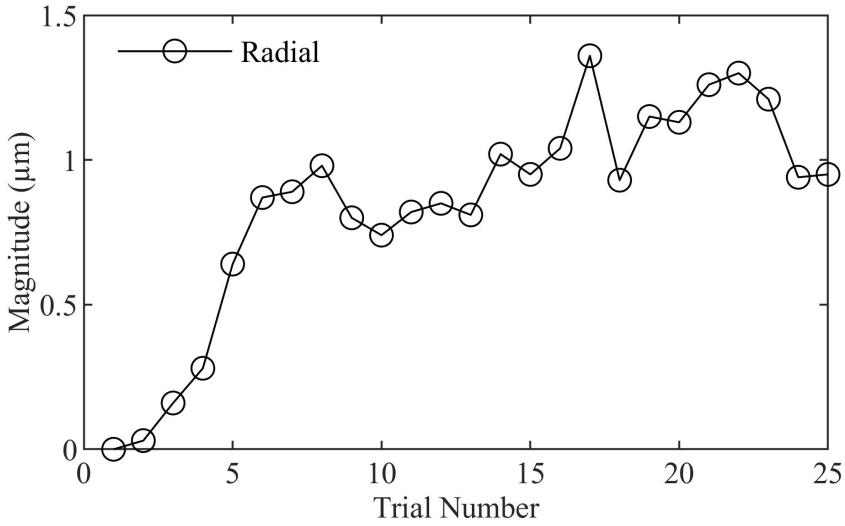

Figure 2.13: This figure shows the initial radial position change of the centroid of the optic, which shows a break in period near 10 trials. The other degrees of freedom that were measured exhibited a similar effect. The measurements were taken again after the break in period, which were the measurements used to quantify the uncertainty of position repeatability.

and stability over time, prior to taking measurements.

Measurements were taken in sets of 25 and temperature data was recorded each set. The process for each trial was as follows:

1. Optic installed in mount
2. Preload applied in a sequence
3. Capacitance gauge readings recorded
4. Preload removed in a sequence
5. Optic uninstalled from mount

2.3.2 Absolute Repeatability

An initial set of measurements were taken with no lubrication on the mount contact surfaces, which showed a break-in period at approximately 10 trials, shown in Fig. 2.13. The magnitude of the centroid absolute position during the break in period

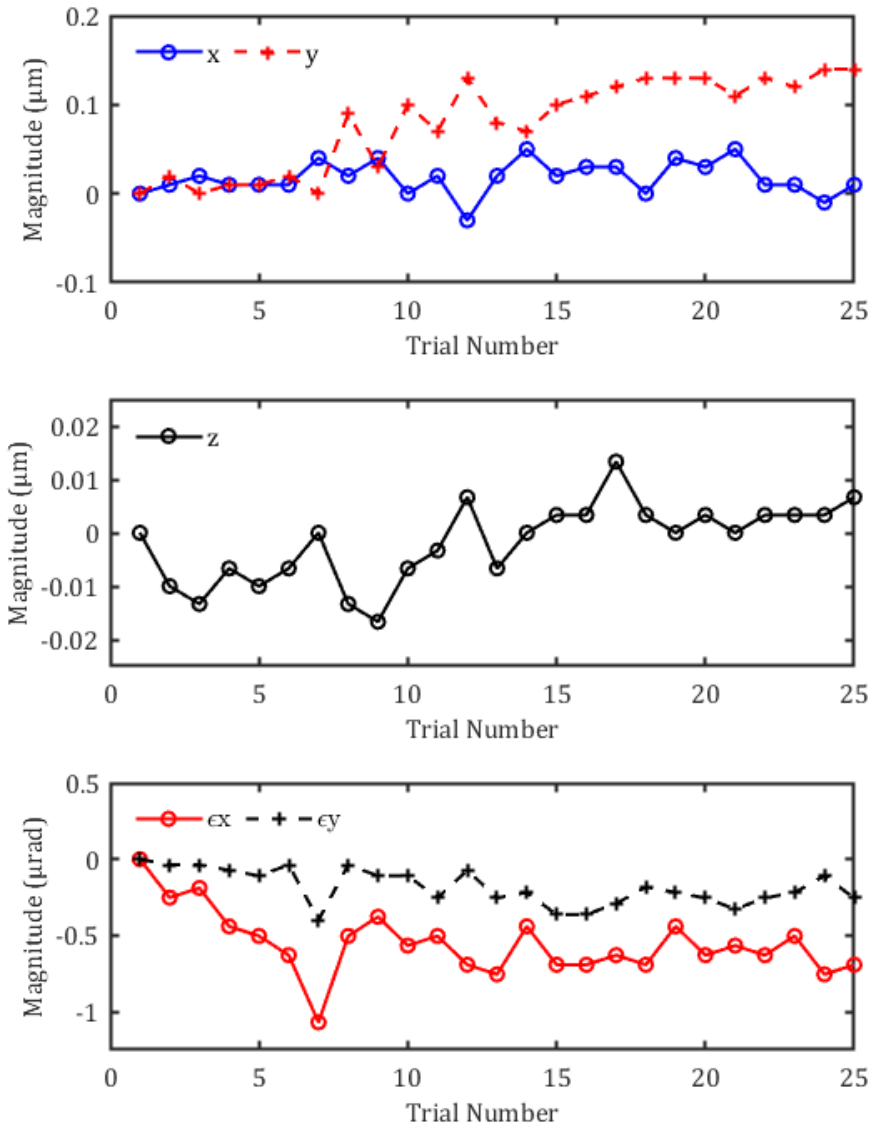

Figure 2.14: Single measurement set with typical results.Temperature effects were not removed from data.

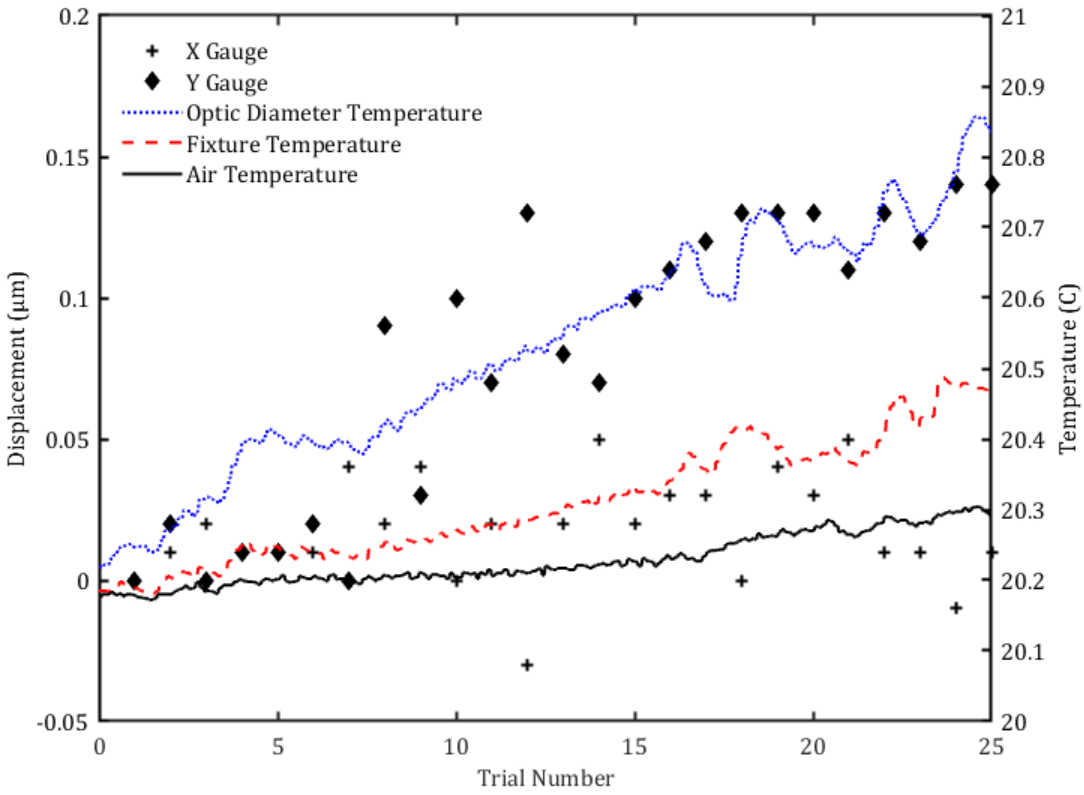

Figure 2.15: The figure shows recorded temperature data overlapped with the measurements for x,y position repeatability. The temperature probe on the optic diameter was nearest to the Y capacitance gauge. This location on the optic is where it was handled during the repeatability test, therefore some thermal drift was expected. This thermal effect would not occur during manufacturing, as the optic and diamond turning machine will have a soak out time prior to machining.

changed by approximately 1 µm. The measurements then settled to a peak to valley range of 0.5 µm after break in. The axial and angular changes exhibited a similar trend as the centroid position, where after the break in period the peak to valley changes were less than 0.25 µm and 2.0 µrad, respectively.

After the break in set was completed, the mount was cleaned and lubricated with a silicon based lubricant to reduce the frictional effects prior to the remaining measurements. Fig. 2.14 shows a typical result from a measurement set without removing the contribution of thermal drift in the data. The peak to valley range from the initial absolute position for a combined in plane repeatability is less than 200 nm. The peak to valley of the axial displacements is less than 40 nm and angular changes are less than 1 µrad.

The measurement along the y direction had the largest amount of drift in the data. The optic was handled closest to this sensor during the measurement process and some thermal drift was expected. Fig. 2.15 shows a qualitative correlation between the temperature of the metrology loop and the drift in the y direction measurements.

2.3.3 Relative Position Change

The peak to valley repeatability over a series of consecutive measurements exceed the requirement by an order of magnitude, yet it is not the best representation of the mount when used in practice. In use, the optic is installed in the mount, preloaded, and the optical surface and reference datums are manufactured. The optic is removed from the mount and installed on a matched coupling for figure metrology. After figure metrology is performed, another iteration of figure correction is performed, and the process is repeated until convergence is achieved. The iterative process redefines the coordinate system of the optic after each installation with the exception of the final iteration. Therefore, the change in relative position is a direct representation of the errors that will affect system performance.

To quantify this, the absolute value of the differences between the positions from

one to the next were calculated. Multiple sets of measurement data were combined with the difference taken from one measurement to the next. This gives the relative position change of the measurands. The method also reduces the uncertainty of thermal contribution from handling the optic that would otherwise not be part of the manufacturing and metrology process. The relative position change for multiple repetitions are plotted in Fig. 2.16. Box and whisker plots of the relative position change are shown in Fig. 2.17. The mean in plane relative position change is less than 50 nm for 1σ and less than 100 nm for 3σ. The mean axial relative position change is less than 10 nm and the angular changes are less than 0.25 µrad with 3σ being approximately 25 nm and 0.5 µrad respectively. Table. 2.2 provides a summary of the results compared to the original error allowance. Table. 2.2 also shows the updated values for the error budget, where a coverage factor was applied to the statistics from the measurements. These values are used for all each mirror in the system level error budget.

Table 2.2: Repeatability contribution to the error budget and a summary of the results

Parameters	x (µm)	y (µm)	z (µm)	ϵ_x (µrad)	ϵ_y (µrad)
Initial Error Allowance	1.00	1.00	1.00	10.00	10.00
Absolute P-V	0.10	0.15	0.03	1.10	0.40
Relative P-V	0.06	0.10	0.03	0.60	0.60
Updated Error Allowance	0.15	0.15	0.06	1.25	1.25

2.4 Conclusion

The kinematic mount designed and analyzed in this research meets the requirements for all expected external load cases and has a repeatability that is an order of magnitude better than the requirement. The subcomponents required no special tooling, machines or fixturing to manufacture nor did they require better than standard machining tolerances to achieve the goals. This resulted in a low cost mount where any quality machine shop could manufacture the components. The torsional

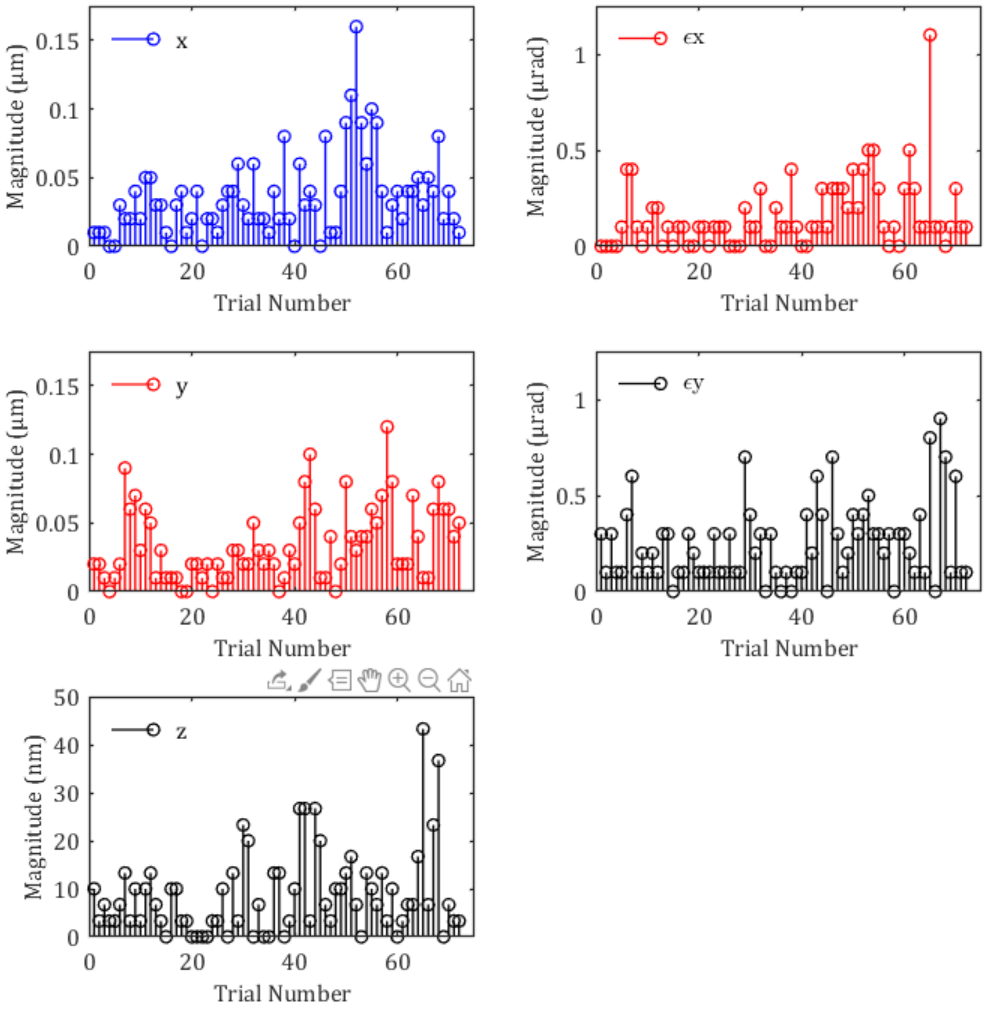

Figure 2.16: Relative 5 degree of freedom repeatability magnitudes

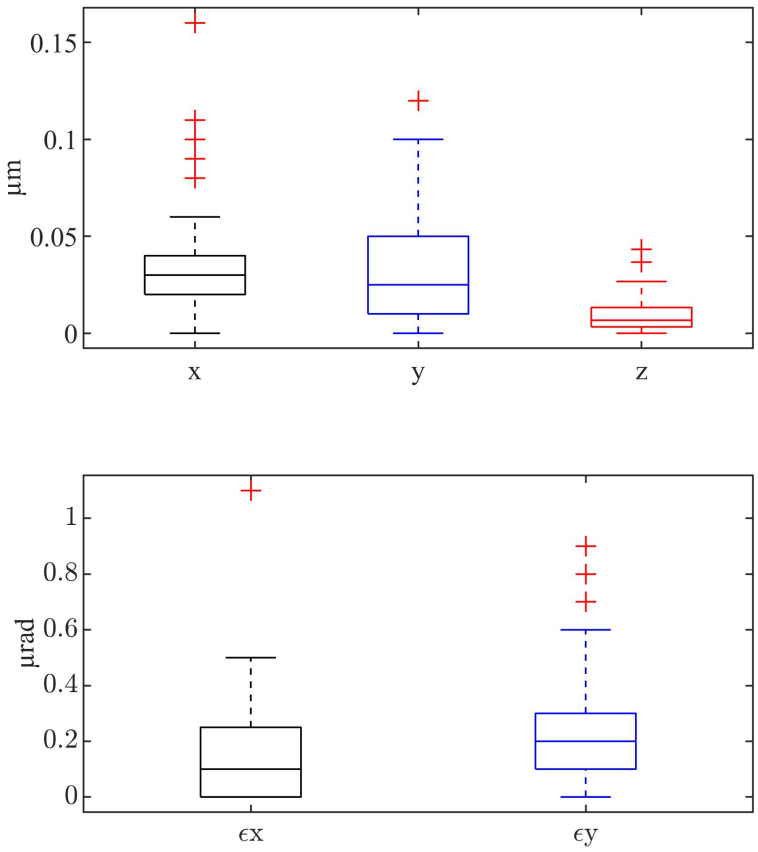

Figure 2.17: Relative position changes for in plane, axial, and angular. The box represents between the 25^{th} and 75^{th} percentile, the line through the box is the mean value, and the whisker extensions are the peak to valley values, excluding outliers which are marked with a (+)

.

preload configuration and analysis of the process forces shows the robustness of the mount, where the compliance goal was satisfied for larger cutting forces than seen in diamond turning. With an increase in preload, other machining processes and components could benefit from this type of mount, such as grinding hubs, lathe chucks, or other rotating equipment.

This Chapter was published in Precision Engineering, Vol. 60, N. W. Horvath, M. A. Davies, and S. R. Patterson, Kinematic mirror mount design for ultra-precision manufacturing, metrology, and system level integration for high performance visible spectrum imaging systems, 535-543, Copyright Elsevier (2019). Additional permissions for reprint of work is not required in a thesis or dissertation.
(www.elsevier.com/about/policies/copyright/permissions)

CHAPTER 3: GRINDING OF ADDITIVELY MANUFACTURED SILICON CARBIDE SURFACES FOR OPTICAL APPLICATIONS

3.1 Introduction

Freeform optics are a disruptive technology in the optics industry [5] due to the ability of freeform designs to (i) reduce the number of optical components, (ii) drastically reduce system size (x5 or more) [39], (iii) improve performance, and (iv) enable new optical functionality [52]. In imaging systems, dramatic improvements are possible if the initial optical design is chosen judiciously [6]. This has led to interest in telescope designs for observation and surveillance. The mechanical and thermal properties of silicon carbide make it a candidate material for such designs particularly for harsh environments. Because of the necessity to grind and potentially polish SiC to achieve freeform shapes with optical tolerances, this adds significant manufacturing challenges.

However, these are partially offset by the advantages of freeform systems, reduced components and compact systems, that reduce the amount of material that must be processed to achieve a given optical function. The production bottlenecks are in the production and processing of the freeform blanks, coating with CVD SiC, and final machining. These can be ameliorated if the time to produce freeform blanks and the processing time (grinding, polishing, metrology) can be reduced. This Chapter describes research results on the production of optical blanks by a novel additive manufacturing production method and the processing of this new grade of SiC by rough and finish grinding.

Abrasive machining of advanced ceramics presents complexities not found in metals. As described by Inasaki [53], Malkin and Huang [54], and Komanduri et al. [55],

ceramics are predominantly covalent materials (Si_3N_4 75%, SiC 88%), subsequently have low ratios of Youngs modulus to hardness ($\frac{E}{H_v}$) and high ratio of shear modulus to bulk modulus ($\frac{G}{K}$) all of which correspond to limited slip systems, narrow dislocations and brittle behavior down to small length scales. Thus gentile conditions for processing are required leading to increased processing time. Thus, the same properties that make ceramics such as silicon carbide desirable make them difficult to process. To complicate matters further, industrial SiC is manufactured in several grades produced by sintering, reaction bonding, crystal growth, and chemical vapor deposition (CVD) and the grade affects their material behavior and grinding performance [56]. Nonetheless, work by Zhong et al. [57] and more recently by Namba et al. [58], Ruckman et. al [59] and Shanmugam et al. [56] demonstrate that ultraprecision grinding of SiC can possibly produce optical quality surface roughness on complex optics without the need for post processing.

In this research, we present the first grinding results for a new grade of SiC produced by additive manufacturing methods and densification by chemical vapor infiltration (AM SiC). The advantage of the process is its ability to produce an essentially arbitrary near net shape freeform surface in SiC. This minimizes material removal by time intensive abrasive processes. Additionally, by extending chemical vapor infiltration (CVI) beyond densification, an outer cladding (similar to CVD) suitable for optical surface finishes is generated. This could further eliminate extensive rough grinding and separate CVD coating. The end goal is to bring processing time for freeform SiC optics from months to weeks.

3.2 Additive Manufacturing Process and Material

The additive manufacturing process consists of two stages. The first stage is additive manufacturing of a SiC green body from powder feedstock in a binder jet process. A high purity α-SiC powder feedstock with a grain size of $23 \pm 6\,\mu m$ is bonded with an aqueous or organic based binder with a layered print strategy [27]. As with most

powder bed systems, this strategy can produce virtually any desired geometry. The powder bed print undergoes a binder curing step followed by CVI at a temperature of 1000 °C and a gauge pressure of 27 kPa that infiltrates the pores in the preform until it reaches approximately 90% density. Continued infiltration beyond this point will result in surface features that are fully dense, similar to CVD of SiC on a substrate. Because the outer skin is a continuation of the infiltrated matrix in the substrate, there is no abrupt interface but rather a gradient transformation. Figure 3.1 shows a micrograph of the material after CVI. Black areas are residual porosity, darker gray areas are the original α-SiC powder, and lighter gray areas are the CVI SiC, which has been shown to be highly crystalline with randomly oriented columnar grains and no amorphous pockets [12]. The final material has a density of 2.95 g/cm^3 (92% of theoretical), a characteristic equibiaxial flexural strength of approximately 300 MPa (CVD SiC is 389 MPa), a thermal conductivity of approximately 40 W/(mK), and a Weibull modulus of 14, greater than CVD SiC, which is 5. Grinding experiments were conducted on the AM SiC and compared to CVD SiC to test the viability of the material for freeform optics.

3.3 Description of Experiments

Figure 3.2 shows the experimental setup. The experiments were performed on a Makino a51nx high speed machining center with a 20 kW, 14.000 min^{-1} spindle. This is a 4-axis high speed precision machine suitable for rapid freeform grinding. While the machine is not an ultraprecision machine, it will be shown that it can produce surface roughness that is suitable for infrared optics. A custom grinding arbor was constructed to accommodate diamond grinding wheels. Forces were measured with a Kistler 9257B dynamometer. Roughing and finishing wheels were obtained from Scomac Diamond Tools. The roughing wheels were 325/400 grit bronze metal bond with an average grain size of 40 µm and N75 diamond concentration. The finishing wheels were 2/4 µm grain size with a copper resin bond and N75 diamond

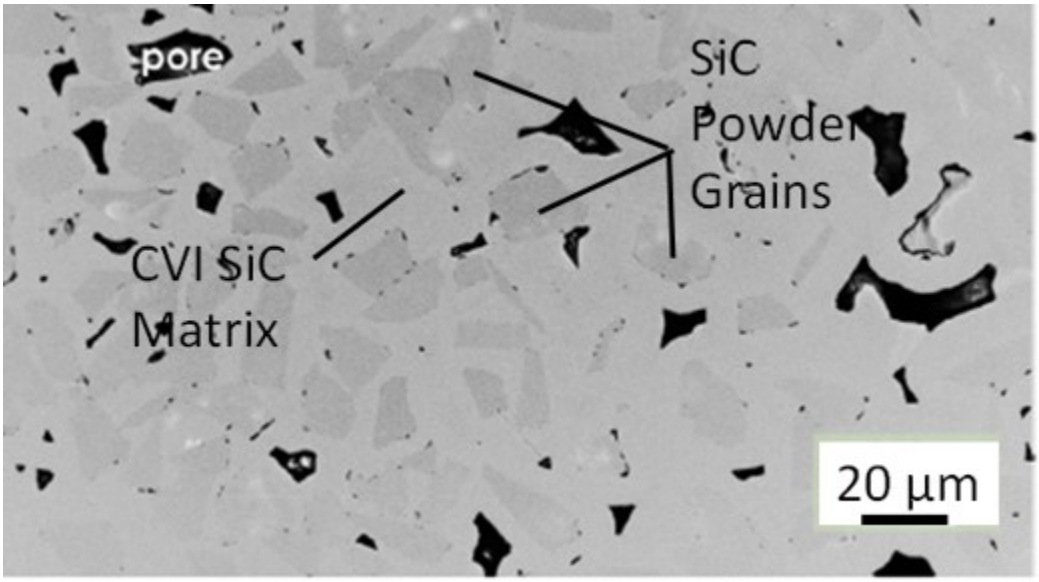

Figure 3.1: A cross sectional view of the microstructure of AM SiC material after the CVI process (Courtesy of Oak Ridge National Laboratory

concentration. Both wheels were toroidal with diameter $d_s = 80\,\text{mm}$ and width $b_s = 12\,\text{mm}$. The Type-F peripheral shape has a nominal radius of 6 mm. The bonded diamond matrix is on the periphery of a 60 mm metal insert. The wheels were both trued by a brake truing device (Norton 3597) with a vitrified 80 grit SiC wheel using a mutual wear toolpath to converge on the prescribed radius of the diamond wheel. The wheels were then dressed with a 400 grit aluminium oxide dressing stick using the same mutual wear toolpath. All grinding was performed under nozzle flood coolant with a Hysol MB 50 5% concentration oil to water emulsion.

Grinding experiments were conducted on bulk CVD SiC and AM SiC. The materials were chosen because CVD SiC and the CVI matrix of the AM SiC have a similar microstructure, which is comprised of small columnar grains. Further, the measured grinding energy for CVD SiC can be compared to existing literature and will provide a baseline for comparison to the AM SiC. The workpiece dimensions were a 50 mm diameter disc and a 50 mm inscribed circle hexagon on the CVD and AM SiC, respectively.

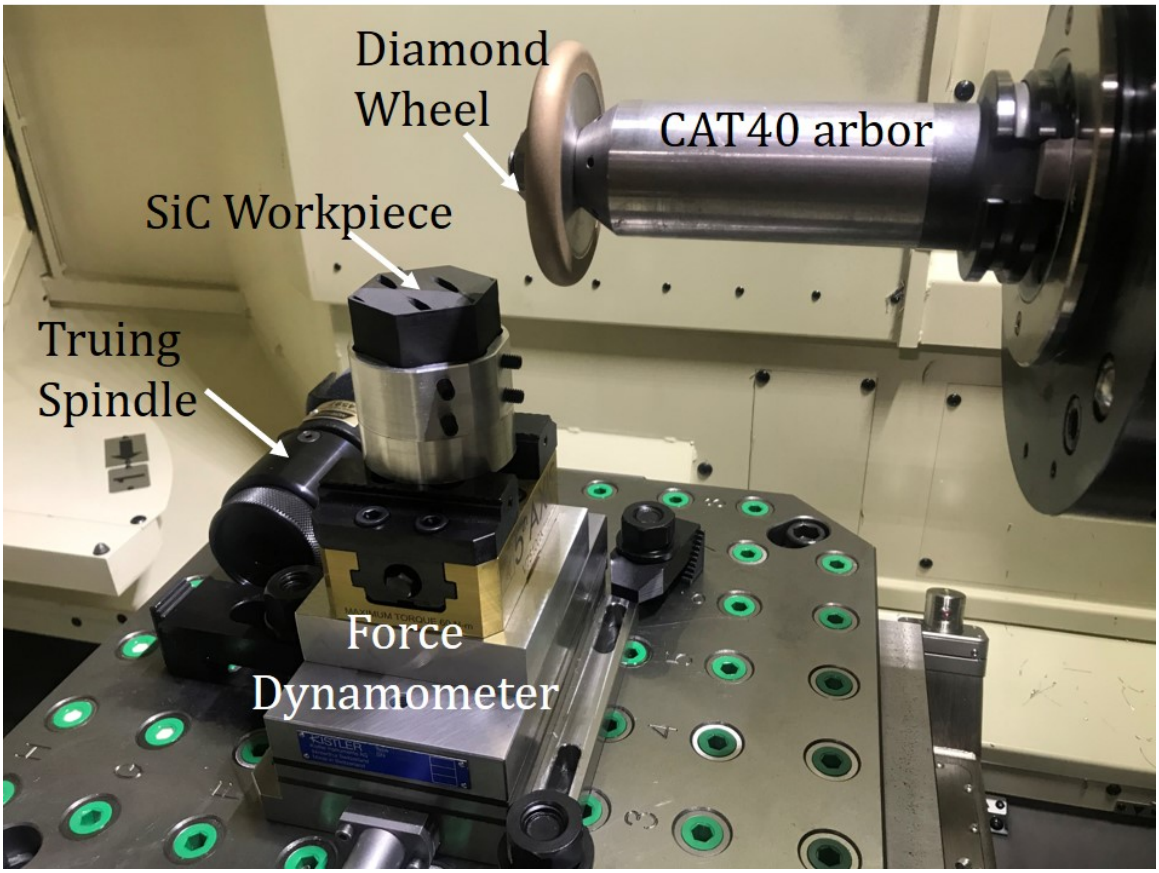

Figure 3.2: Experimental setup showing the workpiece, fixturing, force dynamometer, and grinding wheel.

A cross axis toolpath that enables freeform manufacturing as described by Ruckman et al. [11] was used during the experiments as shown in Fig 3.3. For freeform machining, the grinding wheel remains in a fixed x-y plane, the part is rotated (b), and the grinding toolpath varies along the y-axis as a function of azimuthal position on the part. The stepover progresses along the x-axis towards the workpiece center, resulting in an x-y-b coordinated axis spiral. This configuration is similar to coordinated axis diamond turning used for freeform optics manufacturing where cutter radius, $d_s/2$, and the stepover, s, generate a large-scale cusp pattern on the workpiece. Intrinsic grinding induced errors arise from both the change in d_s and the form of the wheel, which evolve during the grinding process. The cross axis grinding configuration has the advantage that is most sensitive to the maximum d_s and is

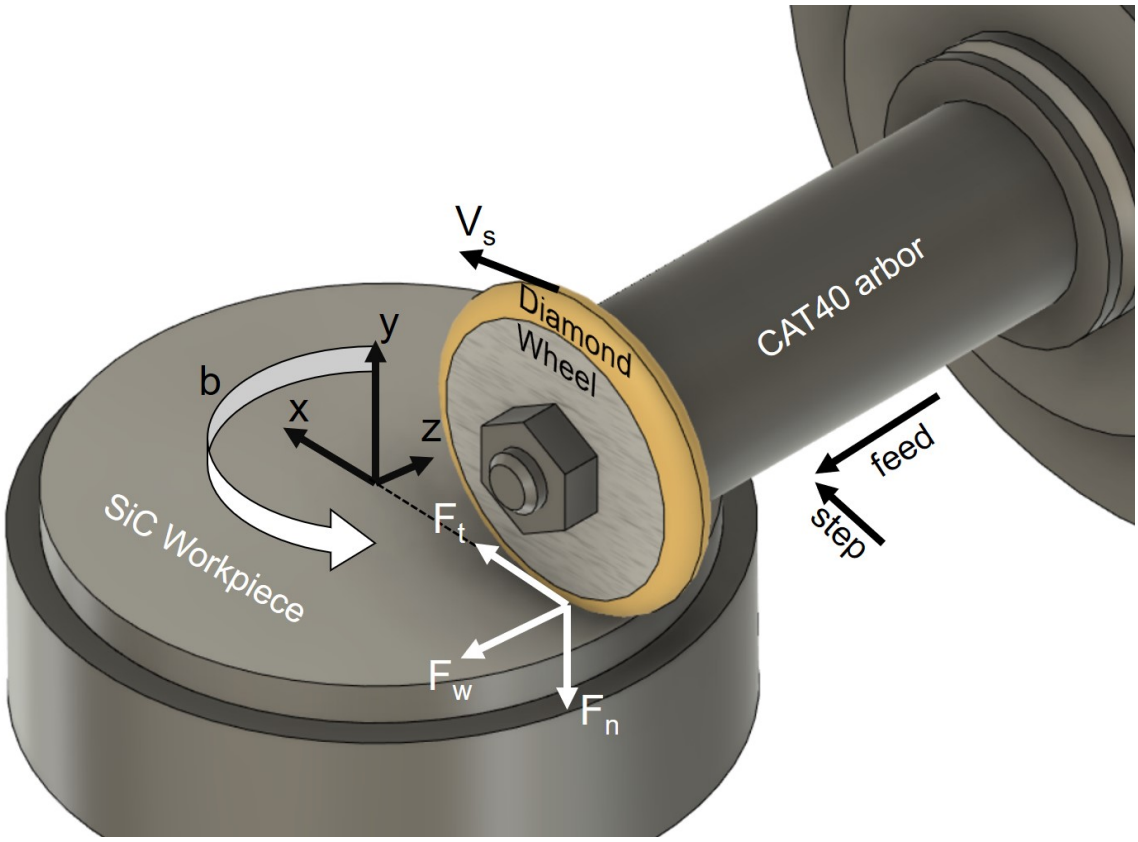

Figure 3.3: Cross axis grinding configuration for contour grinding of freeform shapes

relatively insensitive to wheel form. For the experiments presented in this Chapter, a single direction raster toolpath was used with no continuous rotation of the b-axis, producing a more fundamental set of grinding experiments while still maintaining the engagement configuration that occurs in contour grinding.

Identical process parameters were used for both the AM SiC and CVD SiC. The depth of cut, stepover, and feed per revolution were fixed for the experiments at $d = 0.15\,\text{mm}$, $s = 0.35\,\text{mm}$, and $f = 0.20\,\text{mm}$, respectively. The wheel speed V_s was varied from $20\,\text{m}\,\text{s}^{-1}$ to $50\,\text{m}\,\text{s}^{-1}$. At $58\,\text{m}\,\text{s}^{-1}$, the feed was increased from 0.20 mm to 0.40 mm. The material removal rate range was from $50\,\text{mm}^3/\,\text{min}$ to $290\,\text{mm}^3/\,\text{min}$ with the chosen parameters.

Finish passes with the 2/4 µm resin bond wheel were performed orthogonal to the feed lay of the rough grinding patches. Namba et. al. [10] showed that for an

average diamond size of less than 5 µm, a surface with characteristic scratches along the grinding direction, indicating ductile dominated flow, can be achieved in CVD SiC. Three finish passes were performed at incremental depths, $d = 10\,\mu\text{m}$, with $V_s = 30\,\text{m}\,\text{s}^{-1}$, $f = 0.10\,\text{mm}$, and $s = 0.10\,\text{mm}$ with a bi-directional raster pattern. The first 10 µm depth was finished from the edge to the center of the workpiece, the second 10 µm depth was finished from the edge to 5 mm from center and the final 10 µm depth from edge to 10 mm from center, leaving a stepped pattern on the workpiece. This allowed for observation of gross residual damage from roughing.

3.4 Data Analysis

Force data was collected for all roughing parameters with multiple samples per section. Forces for finish passes were too low to be resolved due to the coolant noise. Therefore, all data shown is for roughing parameters only. A 50 Hz low pass filter was applied to the data to reduce spindle noise. The force signals were trimmed to remove the transient response on workpiece entry and exit and the mean and standard deviations were calculated. Because the cross axis grinding toolpath feeds orthogonal to the rotation direction of the wheel, the axial force component was not ignored.

The specific grinding energy was calculated using Equation 1.

$$E' = \frac{F_t V_s + F_w V_w}{V_w s h} \tag{3.1}$$

Here, F_t is the tangential force component, F_w is the axial force component, V_s is the peripheral wheel speed, V_w is the product of the feed per revolution f and spindle speed in s^{-1}. Error bars on all subsequent figures represent a coverage factor of 2.

A Veeco WYKO NT9100 coherence scanning interferometer (CSI) with a 50x objective and rectangular field of view of 130 µm 174 µm was used to measure surface texture at multiple locations on both the rough ground and finished sections. Tilt was removed from all measurements and a spatial band pass filter of 2.5 µm to 80 µmwas

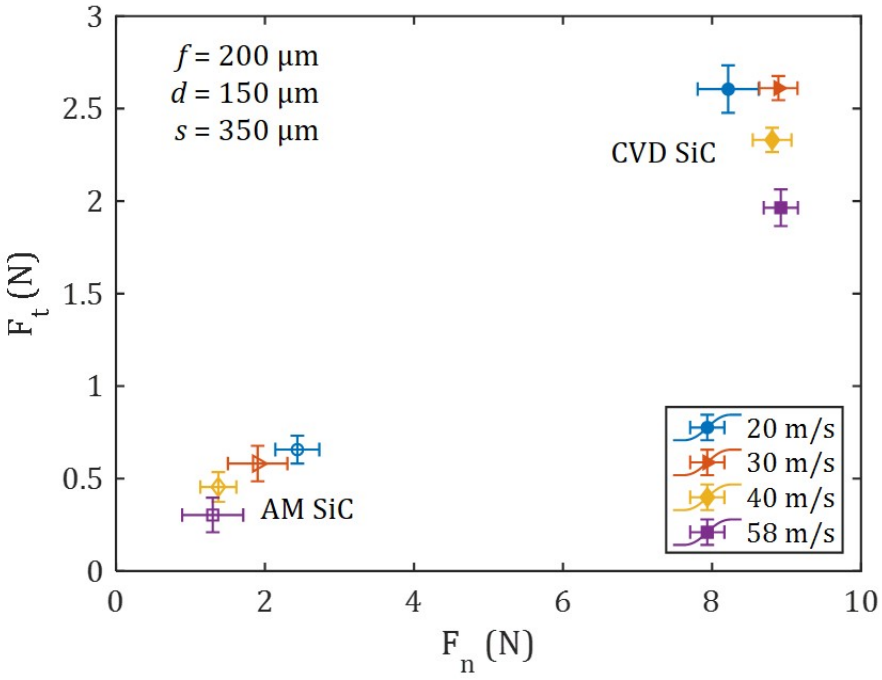

Figure 3.4: Tangential vs. normal force with constant feed per revolution

applied in accordance with ISO 10110-8 to quantify RMS surface roughness.

3.5 Results and Discussion

Analysis of the force signals revealed similar trends between the two materials. The forces in the AM SiC were approximately four times lower than the CVD SiC. However, the ratio of the tangential force to normal force ($\frac{F_t}{F_n}$) was in the range of 0.25 to 0.30 for all process parameters for both materials, as shown in Figure 3.4.

The specific grinding energy as a function of V_s and f is shown in Figures 3.5 and 3.6. As with the forces, the specific grinding energy for the AM SiC is three to four times lower than that in the CVD SiC for all parameters. The range for CVD SiC is approximately 15 J/m^3 to 60 J/m^3. From Inasaki [5], the tangential forces and material removal rates can be estimated for SiC at various parameters for surface grinding. The specific energy can then be calculated obtaining approximately 40 J/m^3 at a depth of cut of 25 µm and 55 J/m^3 at a depth of cut of 6 µm. While the grade of SiC is not specified and the configuration is different in [54], these values are in

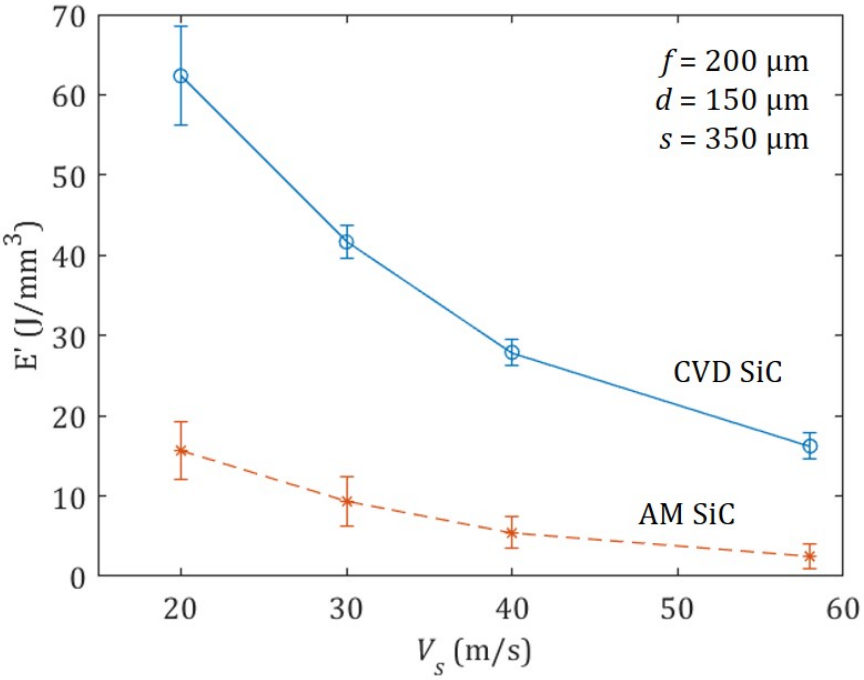

Figure 3.5: Specific grinding energy with constant feed per revolution

reasonable agreement with our measurements and are higher than those for AM SiC. Figure 3.5 shows that the specific energy for both materials drops with wheel speed while Figure 3.6 shows an increase with feed per revolution. A similar observation was made by Kovach et. al., that specific grinding energy decreased with an increase in material removal rate [60].

Figure 3.7 shows the evolution of the surface textures of each sample at the highest material removal rates. The top row shows representative rough ground surfaces of the two materials. Interestingly, the RMS surface roughness on the CVD sample was approximately constant at 0.5 µm for all roughing parameters, with the surface dominated by fracture. The AM SiC sample was similar but the roughness was higher (between 2 µm to 3 µm) and likely underestimated due to data drop out, with the roughness dominated by what appears to be pull out of the α-SiC powder. The second row of Figure 3.7 shows the results of a single 10 µm deep finish pass on both materials. For the CVD SiC, this was adequate to remove any visual evidence of the

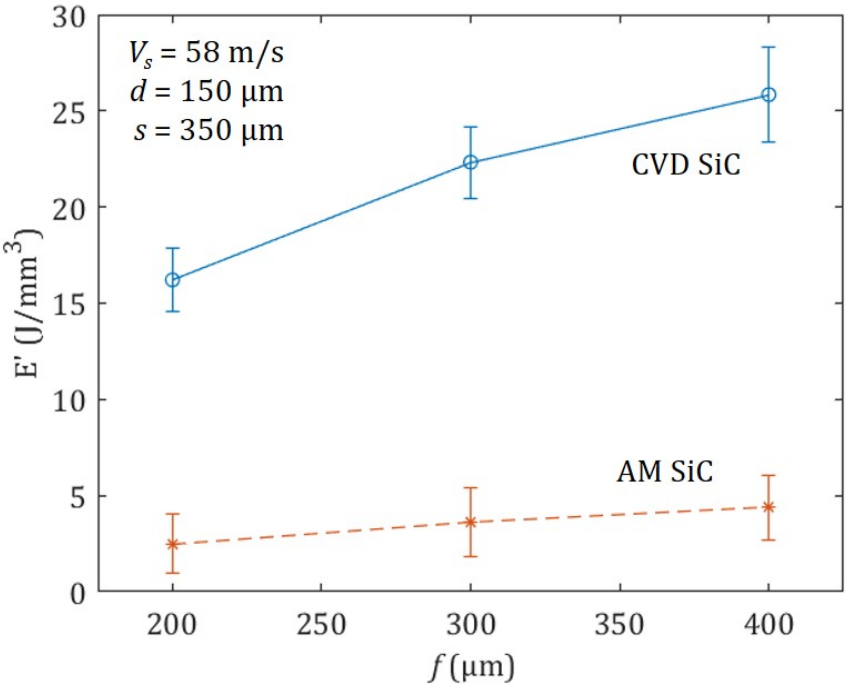

Figure 3.6: Specific grinding energy with constant wheel speed

roughing pass and resulted in an RMS surface finish of 9 nm. The CVI sample still had large voids where the original feedstock particles may have been pulled out of the CVI matrix, resulting in an 800 nm RMS surface finish. However, the CVD SiC and AM SiC are beginning to show characteristic scratches along the grinding direction, indicative of a more ductile flow. After three 10 µm deep finish passes, (shown in Figure 3.7, row three) the remaining voids in the CVI matrix, seen in row two, have decreased to a level more akin to the residual porosity when compared to Figure 3.1, thus, a limitation of the material.

3.6 Conclusions

In this Chapter, we have examined the possibility of using additive manufacturing to make preforms for freeform optics. The additive process utilizes α-SiC powder in a binder jet process, followed by CVI for densification. We compared the grinding behavior of AM SiC to CVD SiC with the following results:

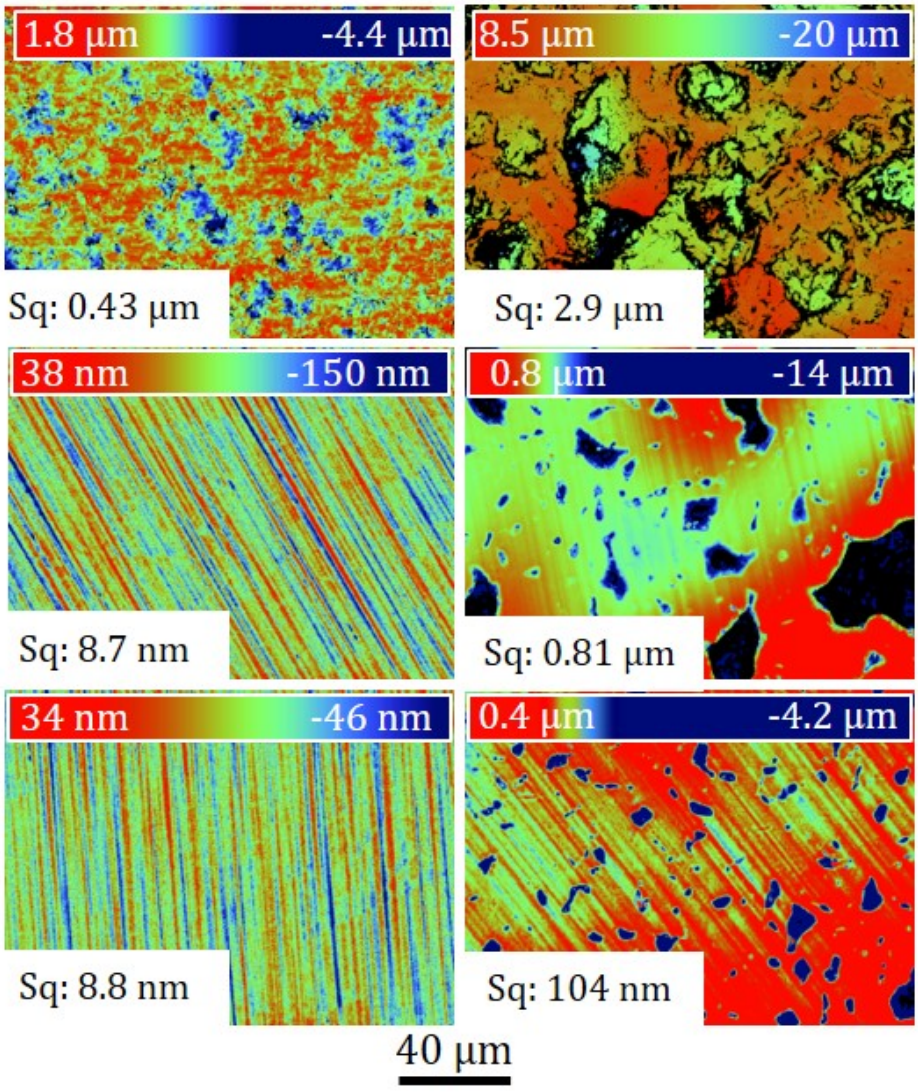

Figure 3.7: CSI measurements for CVD (left column) and CVI (right column). The top row is the surface texture of representative rough ground sections. The second row shows the surface after a single 10 µm depth finish pass. The third row shows the results after three 10 µm depth finish passes.

- AM SiC can be ground with diamond grinding wheels with the same parameters as CVD SiC,
- AM SiC produces significantly lower forces and specific grinding energies compared to CVD SiC,
- hypotheses for lower forces include low bonding strength between the powder and the CVI matrix in the AM composite and material leading to bulk particle pull out and differences between CVD SiC (columnar) and CVI SiC (random) [8],
- the roughness of finish ground AM SiC is limited by residual porosity due to less than 100% density,
- the roughness limitations of the material can likely be reduced or eliminated by extending the CVI process to produce a fully dense CVI outer layer on the AM SiC,
- despite AM SiC material limitations, both finish ground materials have specular surfaces, Figures 3.8(a) and 3.8(b), surfaces were produced on a high-speed precision, not ultraprecision, machining center,
- the achieved roughness of <10 nm RMS is suitable for infrared applications, but the effect of form and mid-spatial frequency errors require further investigation,
- the AM SiC process can produce arbitrary shapes including a near net shape preform for a freeform optic including integrated structural and weight reduction features.

Figure 3.8(c) shows the potential of the process: a light-weighted mirror blank for a SiC freeform telescope printed in less than a week, compared to typical industry turnaround times of months.

Figure 3.8: (a) Finish ground CVD SiC surface. (b) Finish ground AM SiC surface. (c) A 270 mm diameter light weighted mirror blank manufactured by AM process.

CHAPTER 4: ADVANCING LIGHTWEIGHT MIRROR DESIGN: A PARADIGM SHIFT IN MIRROR PREFORMS BY UTILIZING DESIGN FOR ADDITIVE MANUFACTURING

4.1 Introduction

Open back mirrors are one of the most widely used designs for lightweight mirrors in telescope design because of their high stiffness to mass ratio. Most designs utilize an isogrid support structure on the backside of the mirror to achieve the stiffness to mass ratio requirements. These traditional isogrid mirror designs are often 2-D geometries that were developed such that they are readily milled or cast to net shape. However, introducing additive manufacturing (AM) as a new process chain for mirror preforms could offer profound advantages in both, the mechanical design of the mirror by using lattice structures and topology optimization, along with a reduction in lead-time. Sweeney et al. provided case studies using multiple AM methods with varying material choices for mirror designs and discussed findings such as: stress relief during polishing, isotropy of thermo-mechanical properties, and reduced lead time prototyping [61]. While other work has shown other successes in additively manufactured mirror preforms that were then post polished [62, 63], discussions on the design methodology leveraging additive manufacturing have not been discussed in detail.

Current isogrid lightweight mirror designs were developed decades ago with the fundamental design work developed by Barnes, where he introduced analytical solutions for self weight deflections of symmetric sandwich mirrors and local surface deformations over an isogrid unit cell [64]. Mehta expanded on this work to include the equivalent bending thickness to calculate flexural rigidity for both open and closed

back mirrors, along with optimizations based on state of the art manufacturing limitations [65]. Vukobratovich and Valente began implementing finite element methods to further analyze designs that used analytical expressions for lightweight mirrors. Additionally, the previous work included a review of arch back mirror designs and the tradeoffs, including manufacturing difficulty [66, 67]. An intrinsic trade off with isogrid designs are residual surface deformations created during the manufacturing process, known as "quilting". These deformations are caused by the reduced stiffness of the unsupported facesheet which is localized over the unit cells, between the rib structure on the optical surface [68, 36]. The deformations over the aperture from the array of unit cells, cause the surface to have a quilted texture with a lower order radial and azimuthal spatial wavelength variation than typical surface finish, however higher order than surface figure (or form). These are known as midspatial frequencies (MSF). Excessive amplitudes over these spatial wavelengths can have deleterious effects on optical performance, even while meeting both figure and surface finish requirements [69].

The common limitations for the mirror design in the preceding work was the state of the art manufacturing and advanced computer modeling. Analogously the implementation of complex freeform optics was limited by state of the art manufacturing. However, with current machines and multi-axis manufacturing, these freeform shapes are now realizable and transformative for an optical designer [52, 70]. Freeform optics have proven to provide equal or better performance with a smaller volume, thus reducing the overall weight of optical systems [39, 6]. Combining complex surface shapes with complex mechanical geometries for mirror preforms can result in a new standard for optical system performance.

Therefore, the purpose of this Chapter is both, (i) to revisit traditional analytical expressions, providing a systematic design method; (ii) to develop a new design methodology, utilizing a combination of analytical and finite element methods, con-

sidering today's current state of the art manufacturing, to create higher performance mirrors. Thus, the Chapter comprises two main sections on the design and analysis methodology for lightweight mirrors. Section 4.4 describes the design method of an isogrid open back mirror that can be made by traditional manufacturing methods, followed by a finite element model for design confirmation. Section 4.5 then provides the design method for a mirror design considering additive manufacturing for the mirror preform fabrication, also followed by a finite element model for design confirmation. Both methodologies are presented in general form while providing a case study to quantify the validity of each method.

4.2 General Design Conditions and Functional Requirements

To provide a real world case study, boundary conditions and functional requirements were defined. In previous work by the authors, mirrors were designed for a freeform, three mirror, anastigmatic telescope, in both aluminum and SiC [50]. The case study for this Chapter is on the design of the 184 mm tertiary mirror to meet design functional requirements. The low curvature freeform mirror was simplified to a flat mirror only for analysis, as the focus of this Chapter is to introduce the design methodology for the mirror support structure, which is applies to all flat and low curvature mirrors on this scale. The design requirements for the telescope comprise a maximum overall weight and mirror deflection limitations from self weight loading and final surface polishing. The weight of the telescope was distributed between the housing, mounting cells, and mirrors, leading to target mass per unit area of less than $20\,\mathrm{kg/m^2}$. A system level error budget was developed, with the surface figure error (SFE) allowance for the self weight deflection set less than 5 nm RMS. The midspatial frequency subaperture surface deflections (quilting) from polishing, were limited to 43 nm peak to valley. A minimum thickness limitation of 1 mm was also set as a general manufacturing constraint.

To constrain the mirror design, initial volumetric boundary conditions must be set.

First, the diameter, which is prescribed by the optical design, with the second being mirror overall thickness. The mirror design methodologies assume the thin plate relationship for self weight deflection, where the deflection is proportional to r^4/h^2, where r is the semi-diameter and h is the overall mirror thickness. Normalization of the thickness to the diameter (ϕ) show that the increase in compliance below 0.1ϕ resulted in significant self weight deflection with a three point mount with an increased sensitivity of the mount location [50]. The proportionality ratio becomes less sensitive starting at $0.2\phi - 0.3\phi$. Thus, a design decision must be made to either require stiffness in the mirror substrate or a separate support structure, such as a whiffletree. Due to other influences including iterative manufacturing and athermalization, which is outside of the scope of this Chapter but described in Chapter 2, the mirrors would be supported at three points and kinematically mounted to the optical bench, without an additional complex support structure, thus requiring adequate stiffness in the mirror [71]. For these reasons, the mirror starting thickness was set to 0.2ϕ, or 36.8 mm.

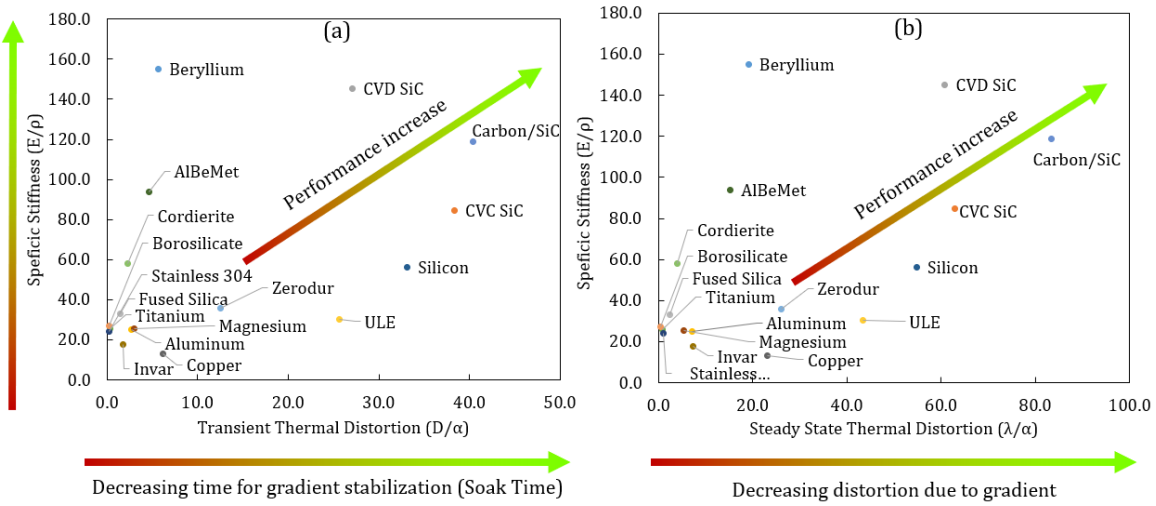

Figure 4.1: Figures of merit for materials commonly used in telescopes. (a) Specific stiffness (E/ρ) versus diffusivity (D) per thermal expansion (α). (b) Specific stiffness (E/ρ) versus conductivity (λ) per thermal expansion (α)

4.3 Material Selection

One of the more attractive materials used for lightweight mirrors in telescope design is silicon carbide (SiC) because of the material's high thermal stability and high specific stiffness [72, 73, 74, 33]. Thermal stability is characterized both by the time for the stabilization of thermal gradients and the distortion caused by a steady state thermal gradient. To visualize this, materials are often compared by putting them on the same graphic as a function of important criteria or figures of merit. For example, Fig. 4.1 displays the transient and steady state thermal dimensional stability of various materials (horizontal axis) against specific stiffness E/ρ (vertical axis), where E is the elastic modulus and ρ is the density. In Fig. 4.1(a) the horizontal axis is D/α, where D is the thermal diffusivity in mm^2/s and α is the thermal expansion coefficient in $10^{-6}/K$. Greater diffusivity and a lower thermal expansion coefficient correspond to more rapid smoothing of transient temperature gradients and reduced strain gradient (stresses, distortion) for an instantaneous thermal gradient. In Fig. 4.1(b), the horizontal axis λ/α where λ is the thermal conductivity in W/m-K and α is the thermal expansion coefficient in $10^{-6}/K$. Greater thermal conductivity and a lower thermal expansion coefficient result in reduced steady state temperature gradient and reduced strain gradient for a given temperature.

SiC far outperforms other materials according to both criteria. However, manufacturing complex geometries in SiC has been challenging and often result in high costs and lead times. Moreover, grinding and polishing of SiC is time consuming and challenging, thus near net shapes are preferable to reduce unduly long post processing times. Terrani et al. introduced a novel process to additively manufacture complex SiC components to a near net shape, with very high purity and density [27]. Expanding on this work, Horvath et al. addressed the post processing of this material compared to CVD-SiC and found that equivalent surface finishes could be achieved with additional work to reduce residual surface porosity [75]. Because of these prior

studies, the mirror design was revisited, specifically in silicon carbide, however the design methodology is agnostic to the material selection. The material properties used for the silicon carbide were 3000 $\mathrm{kg/m^3}$ for the density, 300 GPa for the elastic modulus, and 0.17 for Poisson's ratio.

4.4 Traditional Analytical Mirror Design Methodology

In this section, we implement the design methodology using analytical methods to design a lightweight, open back, isogrid mirror. Imposing the boundary conditions set in Sec. 4.2, the mirror areal mass density functional requirement is first introduced, which prescribes the facesheet thickness limits. From this, the mass reduction is accomplished by introducing the solidity ratio, where the solidity ratio range is defined by the facesheet thickness and self weight deflection requirement. The isogrid support structure is designed by varying the cell size and rib thickness to meet the solidity ratio requirements, while also designing to meet the quilting requirements. In addition, the location of the neutral axis varies as a function of solidity ratio and facesheet thickness. Thus, an analytical expression was developed to approximate the location of the neutral axis using only the previously defined design parameters. Because varying the design parameters change the outcome for multiple functional requirements and are therefore not independent, a series of graphics plotting the design parameters were developed to better visualize the trade-offs and limiting values to achieve the mirror functional requirements. Fig. 4.2 provides a flowchart for the traditional mirror design methodology.

Nomenclature

The list of symbols used in the Chapter are given.

δ_q	Peak to valley surface quilting deflection
δ_{RMS}	Root mean square mirror self weight deflection
η	Areal solidity ratio
κ	Rib effectiveness factor
ν	Poisson's ratio
ϕ	Mirror diameter
ρ	Material density
A	Mirror area
B	Inscribed cell diameter
D	Flexural rigidity of a circular disc
E	Modulus of elasticity
h	Overall mirror thickness
h_c	Cell depth
t_f	Facesheet thickness
t_w	Rib/Web thickness
r	Mirror semi-diameter

Other variables are defined throughout.

4.4.1 Areal mass density and self weight deflection

Mirror apertures widely vary in size based on specific applications, thus a better metric for mirror mass is areal mass density, or mass per unit area. The general form for the estimation of the mass per unit area of the mirror is shown as Eq. 4.1

$$\frac{m}{A} = \rho(t_f + \eta h_c), \tag{4.1}$$

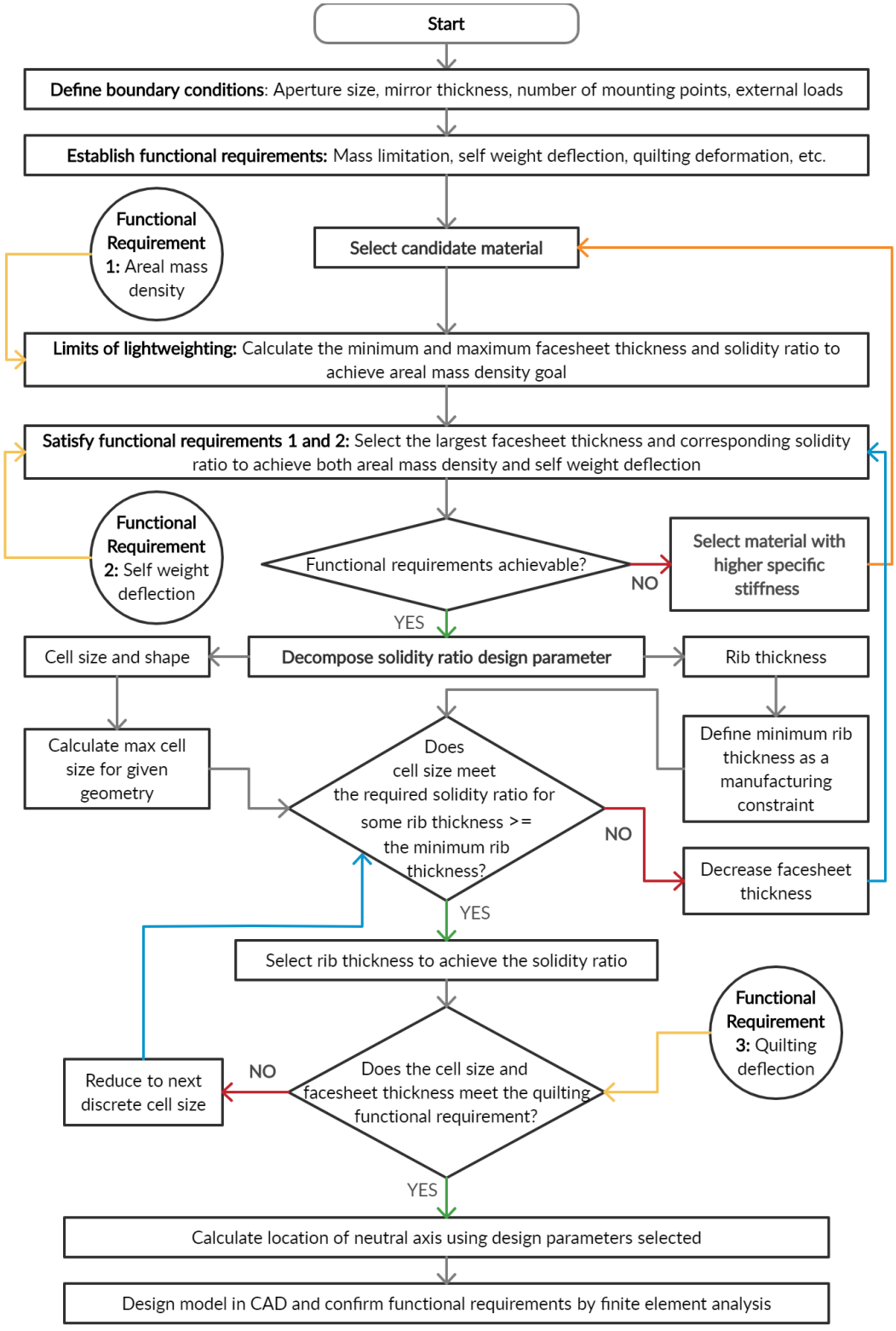

Figure 4.2: Design methodology flowchart for the analytical design of a lightweight mirror considering traditional manufacturing techniques

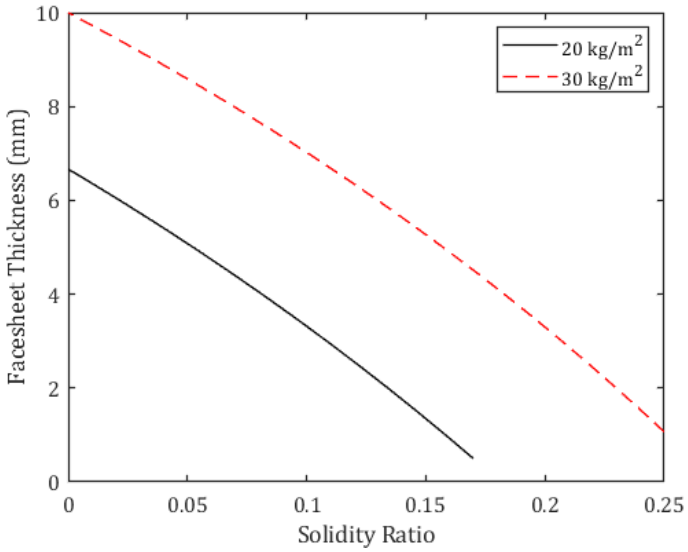

Figure 4.3: Achievable areal mass density considering the facesheet thickness and solidity ratio with a mirror overall thickness set as 36.8 mm.

where m/A is the areal mass density, ρ is the material density, η is the solidity ratio, and h_c is the isogrid cell depth. The overall mirror thickness, initially defined as 36.8 mm, is simply $t_f + h_c$. From Eq. 4.1, we show in Fig. 4.3 the facesheet thickness required as a function of solidity ratio to achieve two areal mass density requirements. Here, the limits of the facesheet thickness and required solidity ratio are shown to meet the areal mass density functional requirement. The maximum facesheet thickness to meet the 20 kg/m^2 requirement is approximately 6.5 mm, however leaving no material for an isogrid support structure. At the lower limit for the facesheet thickness of 1 mm, the manufacturing constraint previously mentioned, the solidity ratio required is approximately 0.16.

Using the facesheet and solidity ratio limits defined by Eq. 4.1 and shown in Fig. 4.3, the first functional requirement that can be met is the self weight RMS surface deflection. From the thin plate assumption, an analytical estimate of the mirror RMS surface deflection is shown in Eq. 4.2

$$\delta_{RMS} = C\frac{\rho g}{E}\frac{r^4}{{h_b}^2}(1-\nu^2), \tag{4.2}$$

where C is a constant from the mounting condition with $C = 0.323$ for a three point mount [76], ρ is density, g is gravitational acceleration, r is the semi-diameter of the mirror, ν is Poissons ratio and h_b is the equivalent bending thickness. The equivalent bending thickness was derived by Mehta for both open and closed back mirrors [65]. The equivalent bending thickness for an open back mirror is shown by Eq. 4.3

$$h_b = \left(\frac{(1-\kappa\eta)({t_f}^4 - \kappa\eta {h_c}^4) + \kappa\eta(t_f + h_c)^4}{t_f + \kappa\eta h_c}\right)^{\frac{1}{3}}. \tag{4.3}$$

It is worth emphasizing at this point that Mehta introduced a rib effectiveness factor, κ, to account for buckling and shear of the ribs in the isogrid. Mehta used an effectiveness factor of 0.5 for triangular and square cells and described the hexagonal pattern as "significantly smaller" [65]. The effectiveness factor provides a conservative estimate of the flexural rigidity of the mirror, in turn potentially leading to a design heavier than required. However, with most designs having partial cells and geometric variations around mounting point locations, further analysis is required by numerical finite element methods. After the creation of a solid model for finite element verification, small changes can be made to the design parameters to meet the functional requirements.

The self weight deflection for multiple facesheet thicknesses as a function of solidity ratio, using a three point mount is shown in Fig. 4.4. From the data in Fig. 4.3 it is shown that for any facesheet thickness that meets the requirement of $20\,\mathrm{kg/m^2}$, the solidity ratio to achieve this is too large to also meet the self weight deflection requirement. Mentioned, the conservative effectiveness factor could result in a stiffer mirror than designed. For this reason, values for the facesheet thickness of 2 mm and the solidity ratio of 0.15 were chosen. These values slightly exceed the areal mass

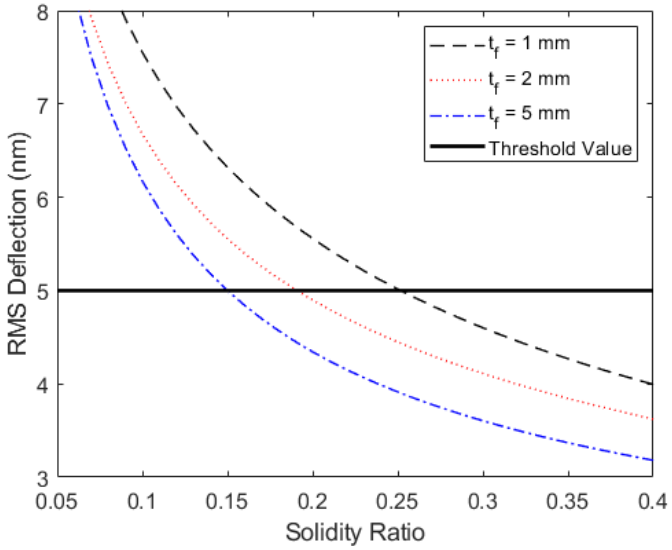

Figure 4.4: Self weight mirror deflection with a three point mount

density requirement and would be analyzed further after the creation of a solid model.

4.4.2 Isogrid Cell Geometry

To design the isogrid structure, the solidity ratio must be decomposed into physical design parameters. The solidity ratio is defined as the ratio between the area of an open geometry over the area of a solid geometry and is shown in Eq.4.4

$$\eta = \frac{(2B + t_w)t_w}{(B + t_w)^2}, \tag{4.4}$$

where B, and t_w are the geometry dependent inscribed circle cell size and interconnecting web thickness, respectfully. Figure 4.5 shows the three main geometries used for isogrid support structures with the parameters for calculation of the solidity ratio. Here, Fig. 4.6 shows the effect on the solidity ratio as a function of the cell diameter and discrete cell web thicknesses. Thus, the cell size and web thickness can be selected to meet the solidity ratio requirements, however additional constraints on the cell size must be introduced.

The first constraint is an upper geometric limit due to mounting point location.

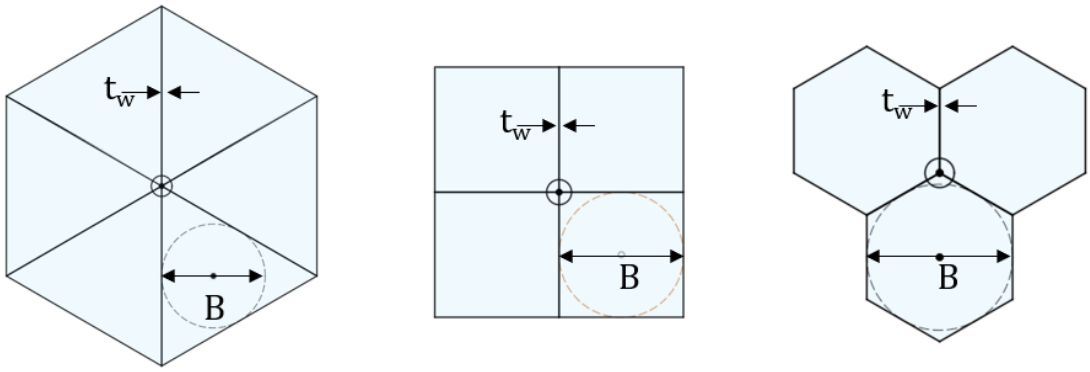

Figure 4.5: Examples of commonly used isogrid geometry. Left to Right: triangular cell, square cell, hexagonal cell. The central circle represents the central node for the connection points for the web with the triangular cell having 6 connections at the central node, the square and hexagonal with 4 and 3, respectively. Design parameters web or rib thickness, t_w and inscribed cell size, B are used to calculate solidity ratio.

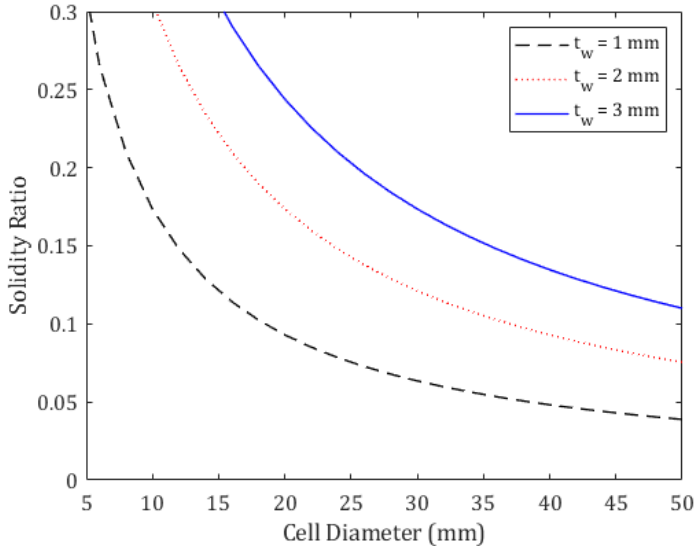

Figure 4.6: Solidity ratio as a function of the cell diameter at multiple web thickness values

Mentioned, this study is constrained to a sub aperture 3 point mount which is known to be at an optimal location at $\approx 66\%$ of the diameter. Moreover, for an open back mirror, the triangular cell geometry provides the highest flexural rigidity compared to square or hexagonal cells. An appropriate design will have the mounting points at a nodal location where the interconnected webs meet to provide the least compliant design at the mounting point, shown in Fig. 4.5. To achieve this using triangular cells, starting from a central node, and maintaining symmetry, the maximum length of the triangular cell wall is $0.66r$, with r being the semi-diameter of the mirror. Thus the maximum inscribed circle to calculate the solidity ratio is defined by Eq. 4.5, which results in a 35 mm cell size for a 184 mm mirror.

$$B = \frac{0.66r}{\sqrt{3}} \tag{4.5}$$

The second constraint is from the peak to valley quilting functional requirement. This surface deformation caused by the pressure applied during mirror polishing, which from Barnes [64], we can estimate using the cell size and unit cell geometry in Eq. 4.6

$$\delta_q = \psi \frac{P}{E} \frac{B^4}{D} = 12\psi \frac{P}{E} \frac{B^4}{{t_f}^3} (1 - \nu^2), \tag{4.6}$$

where δ_q is the deflection over the unit cell, P is the polishing pressure, E is the modulus of elasticity, D is the flexural rigidity, and ψ is a cell geometry constant with the triangular cell $\psi = 0.00151$. Note the equation is completely independent from the depth of the cell. To quantify the effect from these localized surface deformations, Vukobratovic derives the Strehl ratio as a function of the wavelength and quilting deflection from Eq. 4.6, shown in Eq. 4.7

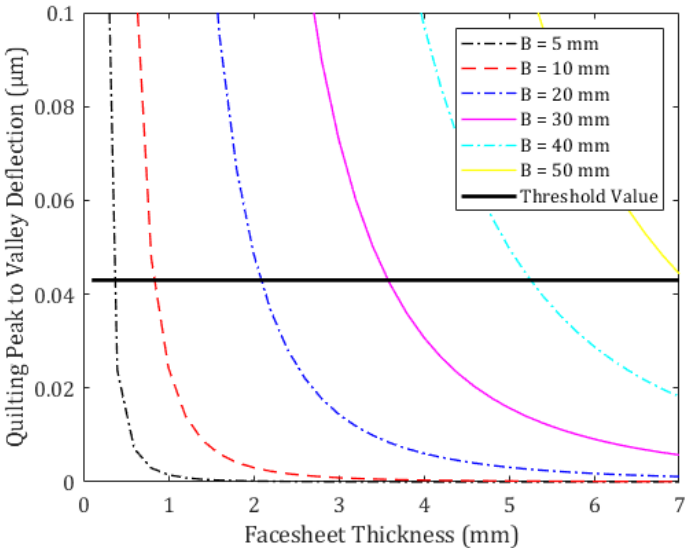

Figure 4.7: Quilting deflection as a function of facesheet thickness for multiple isogrid cell sizes under loading from polishing pressure

$$S = \frac{I_i}{I_o} = \frac{4\pi^2 \left(\frac{\delta_q}{2\lambda}\right)^2}{\left[1 - 2\pi^2 \left(\frac{\delta_q}{2\lambda}\right)^2\right]\left[1 - 4\pi^2 \left(\frac{\delta_q}{2\lambda}\right)^2\right]}. \tag{4.7}$$

For a test wavelength of 632.8 nm and a Strehl ratio constraint of 0.95 to allow for MSF wavefront error over multiple mirrors, this equates to a P-V quilting deflection allowance of 43 nm. Because of the hardness of SiC, higher polishing pressures are required to efficiently remove material [36], thus the polishing pressure of 42 kPa was used as the load condition. The quilting deflection as a function of facesheet thickness and cell size, with a polishing pressure of 42 kPa, is shown in Fig. 4.7.

From these two additional cell size constraints and using Fig. 4.7, the appropriate cell size can be selected to satisfy both the quilting deflection allowance and subsequently, the solidity ratio to achieve the areal mass density functional requirement. From the previous figures and constraints, it is shown for this application that the

maximum cell size of 35 mm will result in non-acceptable quilting deflection for any facesheet thickness less than 4.5 mm, thus a smaller size must be used. However, to ensure that each mounting point is located at the web nodes, the cell sizes are limited to discrete dimensions that can be calculated by Eq. 4.8,

$$B = \frac{0.66r}{\sqrt{3}} \left(\frac{1}{2} \right)^n \tag{4.8}$$

where n is a positive integer. From this, the next lowest size for this mirror is 17.5 mm, which meets the quilting requirement for a facesheet thickness greater than 1.5 mm. Using Fig. 4.6 the cell wall size is selected to meet the solidity ratio at the defined cell diameter, which was selected as 1.5 mm.

4.4.3 Neutral Axis Location for Isogrid Mirror

The location of the neutral axis of an open back lightweight mirror is not at the geometric centerline of mirror. However, it is known that the neutral axis is between the geometric centerline of the mirror and geometric centerline of the facesheet. The effect of the solidity ratio and facesheet thickness will change this location between these bounds. Placing the mounting features at the neutral axis reduces deformations at the optical surface by reducing the length of the moment arm of the mount geometry. Forces at the mounting points could be caused by either thermal or mechanical external loads, thus it is important to know the approximate location to reduce the bending moment. An analytical equation using only the previously described design parameters for the mirror was developed and confirmed by finite element analysis.

The approximation of the neutral axis of the circular plate was viewed in cross section and simplified to a beam model. The model was treated as a 2-component composite structure with a facesheet and lightweight back. Fig. 4.8 provides a diagram of the model including the mirror design parameters. This model assumes flat or low curvature mirrors, where for higher curvature mirrors, there is a small shift in the

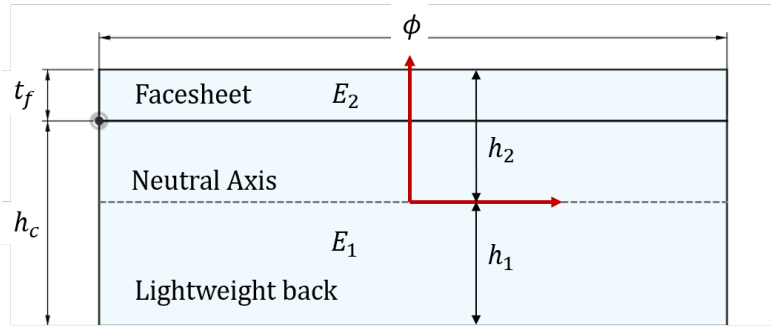

Figure 4.8: Diagram for the derivation of the neutral axis using parameters for the lightweight mirror

neutral axis location that is inversely proportional to the natural logarithm of the ratio of front and back curvatures.

Assuming pure bending and linearly elastic material, the location of the neutral axis can be found by analytic methods by setting the first moment of area equal to zero. For a composite structure this results in Eqs. 4.9-4.11

$$E_1 \int_1 y dA + E_2 \int_2 y dA = 0, \tag{4.9}$$

$$\int_1 y dA = \phi h_c \left(\frac{h_c}{2} - h_1 \right), \tag{4.10}$$

$$\int_2 y dA = \phi t_f \left(\frac{t_f}{2} + h_c - h_1 \right). \tag{4.11}$$

By treating the open back portion of the mirror as a cellular solid, we know from Ashby that the relative stiffness is proportional to the relative density by a power law, Eq. 4.12

$$\frac{E_1}{E_2} = C \left(\frac{\rho_1}{\rho_2} \right)^n \tag{4.12}$$

where C is the proportionality scaling constant and n commonly ranges between 1 and 2 for most cellular solids [77]. Because the areal solidity ratio is constant as

a function of cell depth, it was treated equivalent to relative density, resulting in Eq. 4.13

$$E_1 = CE_2\eta^n. \tag{4.13}$$

Substituting Eqs. 4.10, 4.11, and 4.13 into Eq. 4.9 and reorganizing in terms of distance from the top of the facesheet, h_2, the location of the neutral axis is shown in Eq. 4.14

$$h_2 = NA = (t_f + h_c) - \frac{1}{2}\frac{\eta^n {h_c}^2 + t_f(2h_c + t_f)}{\eta^n h_c + t_f}, \tag{4.14}$$

which is only in terms of the design parameters previously used in the mirror design. The exponential value is assumed to be between 1 and 2 and is solved by a least squares curve fit to a series of finite element models. The scaling constant was set to 1 such that the equation then satisfies the neutral axis boundary conditions mentioned prior.

A FE simulation was performed on a series of fixed free beam models with an end loaded moment. The series of models comprised a solid facesheet and open back structure with defined solidity ratios and facesheet thicknesses. The location of minimum strain in the model after loading was recorded at multiple parameters in order to perform a least squares fit for h_2 by adjusting the exponential term, n. The exponential term, was found to be 1.40 ± 0.08 over a 95% confidence interval. The analytical equation results for location of the neutral axis, normalized to the mirror thickness, as a function of solidity ratio with the overlaid finite element sample points is found in Fig. 4.9. From this, the neutral axis location can be approximated after selecting the facesheet thickness, cell depth, and the solidity ratio. For the mirror design in this Chapter, the location of the neutral axis is approximately 12 mm from the top of the facesheet, or the optical surface.

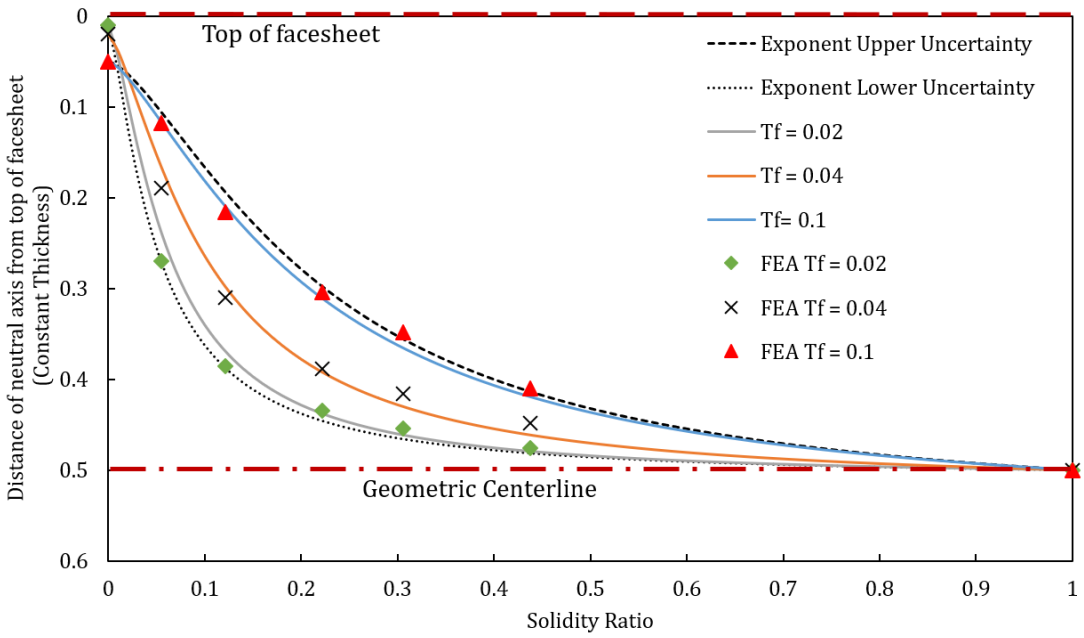

Figure 4.9: Location of the neutral axis as a function of solidity ratio for multiple facesheet thickness values, normalized to the overall mirror thickness

4.4.4 CAD Model and Finite Element Analysis of Analytical Designed Mirror

Using the values calculated from Sec. 4.4, the mirror was designed in CAD software and is shown in Fig. 4.10. Once designed, the areal mass density of the mirror was significantly higher than estimated. This is a result of the mass estimation in Eq. 4.1, which does not account for partial cells, the actual mount geometry, fillets to reduce stress concentrations and access for manufacturing tooling, and the outer shell. To meet the functional requirement the web thickness was reduced from 1.5 mm to 1 mm and the facesheet was reduced from 2 mm to 1.5 mm which reduced the areal mass density to 20.6 kg/m^2. The final solidity ratio of this mirror as designed in CAD, which is simply calculated by the area of the open isogrid structure divided by the area of the face sheet, is 0.15. The neutral axis location was then recalculated based on the actual solidity ratio and updated facesheet thickness, adjusting the mounting plane to 13 mm from the optical surface.

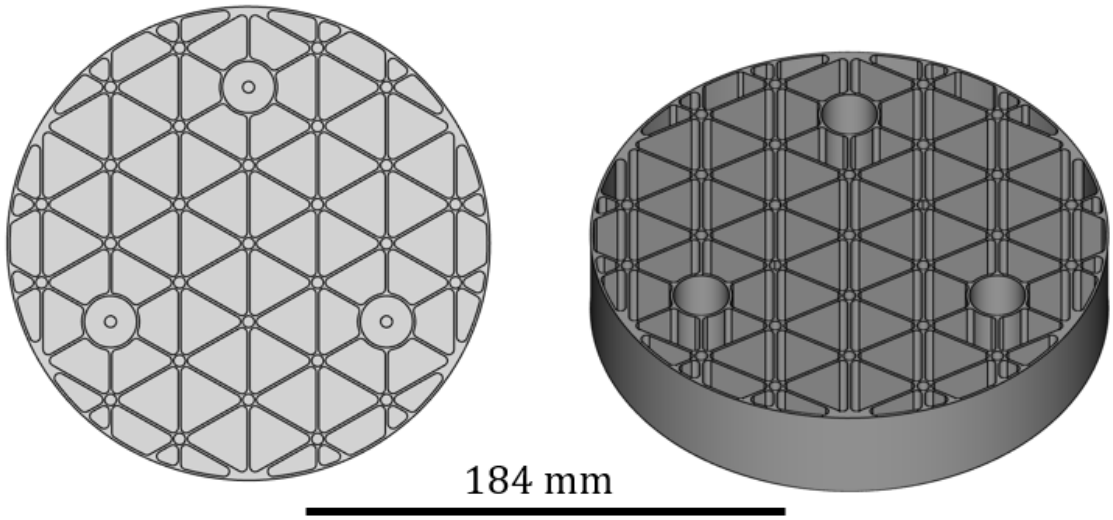

Figure 4.10: CAD model of analytical designed mirror with updated parameters to meet the areal mass density requirement

4.4.4.1 Finite element analysis of the analytical mirror design

Finite element methods are used extensively for design analysis of mirrors to characterize surface shape changes from the expected load cases. However, finite element software lacks the ability to quantify the shape of the deformation and reports only displacements. Thus, the deformed nodes are extracted and post processed to quantify the shape change. The changes to the surface shapes can be described by any number of polynomials, however the more common basis set used are the Zernike polynomials, which are a standard basis set for both optical design and optical metrology due to the orthonormality over circular apertures.

The designed model was imported into computer aided engineering (CAE) software for finite element analysis. A volume mesh with a maximum 4 mm edge length and quadratic tetrahedral elements were used for the entire mirror. An additional symmetric, quadrangulate mesh was used with shell elements on the optical surface, with the elements connected to the main body as dependent elements by the element faces. This method allows for a robust FE analysis while providing a uniform, symmetric mesh at the optical surface for further processing.

Two load cases were run in the FEA simulation, the first, a gravitational acceleration load with the force vector generated by the $1g$ acceleration value acting on the mass of each tetrahedral element. The second load case was a full aperture pressure simulating polishing. In the gravitational load case, the mirror was kinematically constrained by creating local oriented coordinate systems at each of the 3 mounting points and only constraining 2 degrees of freedom per mount point. For the polishing load case, the mirror was constrained by the back surface, which represents the constraint if using traditional polishing techniques. For each load case, the nodal points from the deformed FEA model were extracted for further surface processing.

4.4.4.2 FEA Results

Fig. 4.11(a) and Fig. 4.12(a) show the results in the native CAE software from the gravitational load and polishing pressure respectively. The surface nodes were extracted and least squares fit with Zernike polynomials. All terms up to the 7^{th} order radial and azimuthal, Z_7^7, were removed from the surfaces to reveal the midspatial frequency surface deformations from the isogrid structure. Fig. 4.11(b) shows the imported surface, the 7^{th} order Zernike polynomial fit (c), and the residual map after subtracting the Zernike map (d). The RMS deflection of the surface is found to be 1.2 nm, with higher order residual terms an order of magnitude less. While an order of magnitude less than the requirement, the isogrid structure is clearly visible in the residual map just from the gravity load. Thus, the mirror functional requirement of 5 nm for self weight deflection has been achieved. The analytical solution estimates that the self weight deflection with the current mirror parameters would be 6 nm RMS. As mentioned early, the rib effectiveness factor results in a conservative estimate of the flexural rigidity, thus it had a slight over estimate of the expected self weight deflection.

The surface processing from simulating the polishing pressure was treated in the same fashion and is shown in Fig. 4.12. However, the main interest is the residual

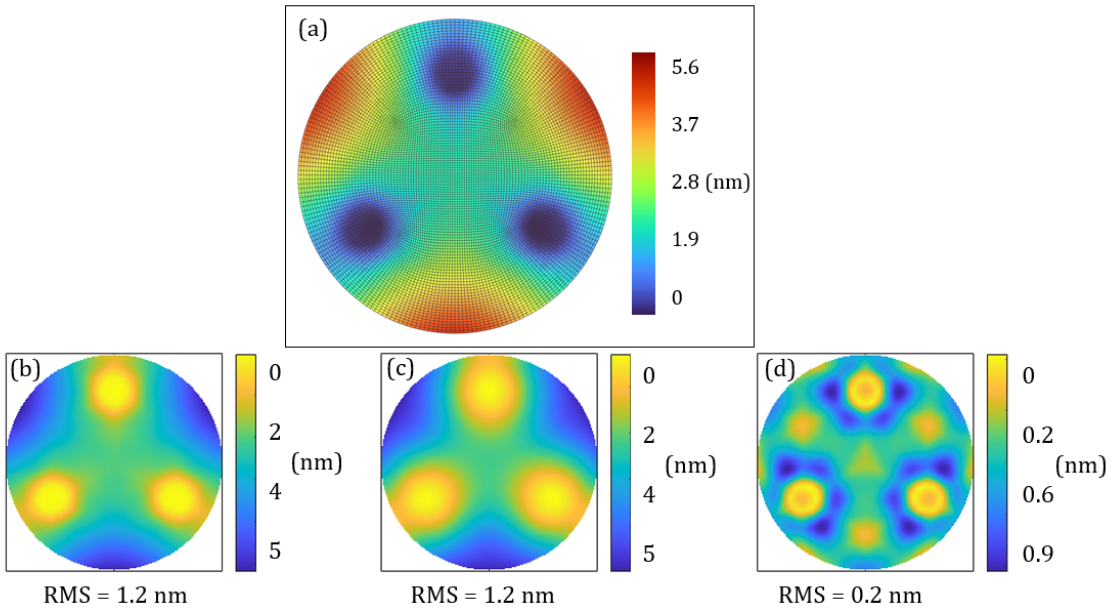

Figure 4.11: (a) FEA results from a $1g$ acceleration normal to the optical surface. The displacement magnitude is shown. (b) Raw imported surface data from quadrangulate mesh, (c) Zernike fit, (d) Zernike fit removal from the data set, or residual map

map 4.12(d), with the quilting functional requirement set as 43 nm peak to valley. The residual map shows that the peak to valley deflection is 42 nm, which just meets the functional requirement. This value also agrees with the analytical solution, Eq. 4.6, with the updated facesheet thickness of 1.5 mm.

In summary, the lightweight mirror has been analyzed to have a self weight deflection estimate of 1.2 nm RMS, a quilting deflection from polishing of 42 nm PV, and a total mass of 0.55 kg, resulting in an areal mass density of 20.6 kg/m^2. The areal mass density result is slightly above the initial functional requirement; however it is considered acceptable with all other requirements and manufacturing constraints being met.

4.5 Mirror Design Methodology for Advanced Manufacturing

Additive manufacturing is the latest addition in the advanced manufacturing portfolio and is often described as a leading disruptive and transformative technology for the next industrial revolution. Unlike traditional subtractive manufacturing meth-

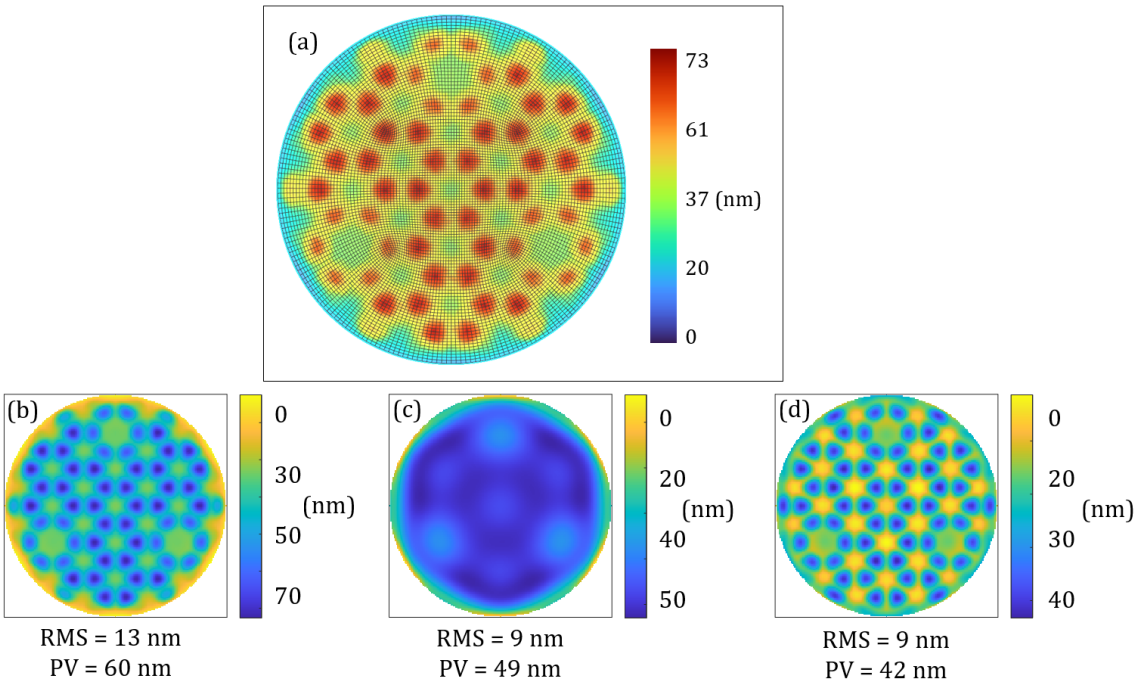

Figure 4.12: (a) Traditional mirror surface deflection from polishing pressure in native FEA output, (b) Raw imported surface data from quadrangulate mesh, (c) Zernike fit, (d) Zernike fit removal from the data set, or residual map

ods, such as milling or grinding, additive manufacturing does not require line of sight to create a geometry. Because of this, additive manufacturing enables new design freedoms not previously investigated. Combining readily available computer aided engineering software with additive manufacturing, the design of the mirror should be revisited to leverage these benefits.

This section uses the same initial boundary conditions and functional requirements found in Sec. 4.2. The mirror initial conditions began with the same volumetric design space as the traditional mirror, a 184 mm diameter, with a thickness of 36.8 mm, and 3 mounting pads at 0.66ϕ. The functional requirements are also identical, with the areal mass density requirement set as $20\,\mathrm{kg/m^2}$, quilting deflection less than 43 nm PV, and a self weight deflection less than 5 nm RMS. A minimum thickness limitation was also set to 1 mm, identical to the traditional mirror. However, the similarities to the traditional design end there. In this methodology, the functional requirements are

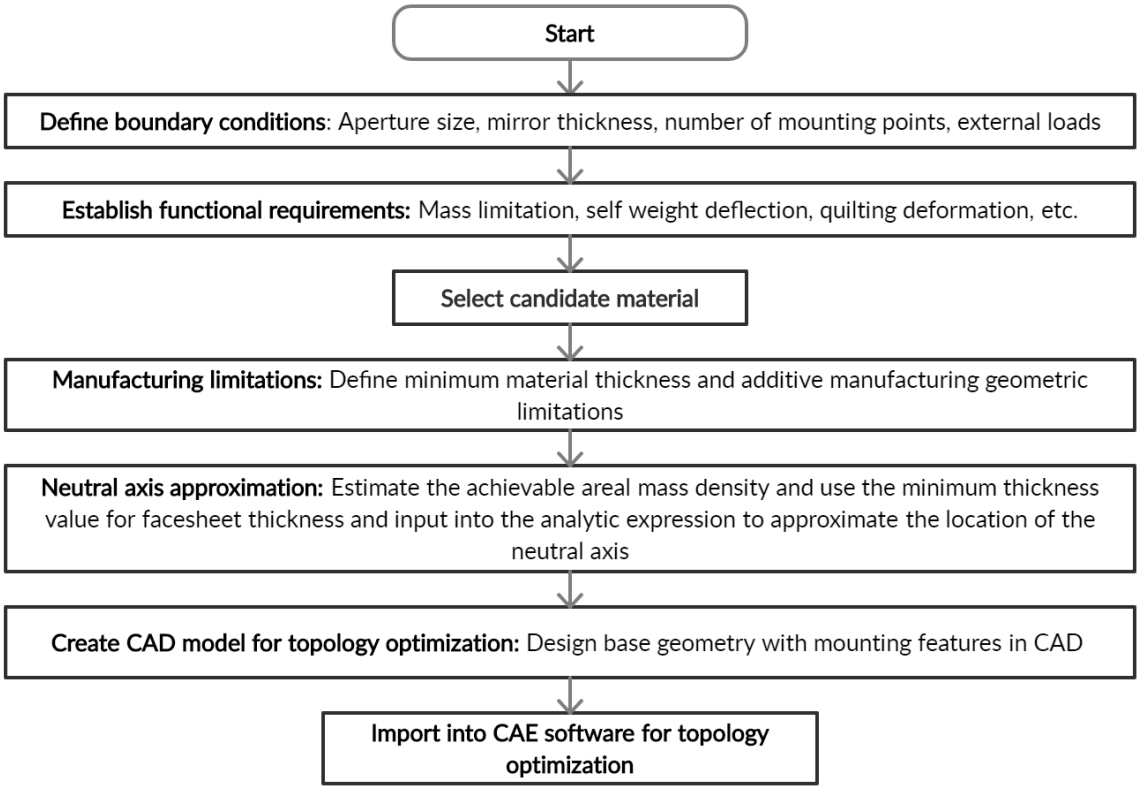

Figure 4.13: Part 1: Design methodology flowchart for the advanced mirror design considering additive manufacturing

met by a combination of computer aided engineering and fundamental understanding of the analytical methodology.

Figures 4.13 and 4.14 provide a flowchart for the advanced mirror design methodology. This design method begins with the creation of a solid model defined by the initial conditions. The model is then imported into CAE software for a topology optimization using the appropriate load cases, mounting restraints, material properties, and functional requirements. The mandatory geometries are selected such that the optimization does not suggest material removal in these volumes. For a mirror, the only mandatory geometry should be the facesheet and mounting points. The topology optimization results in a model comprised of threshold elements that are ranked between 0 and 1. In this case, threshold elements define which elements are contributing to the overall stiffness required to meet the displacement requirements,

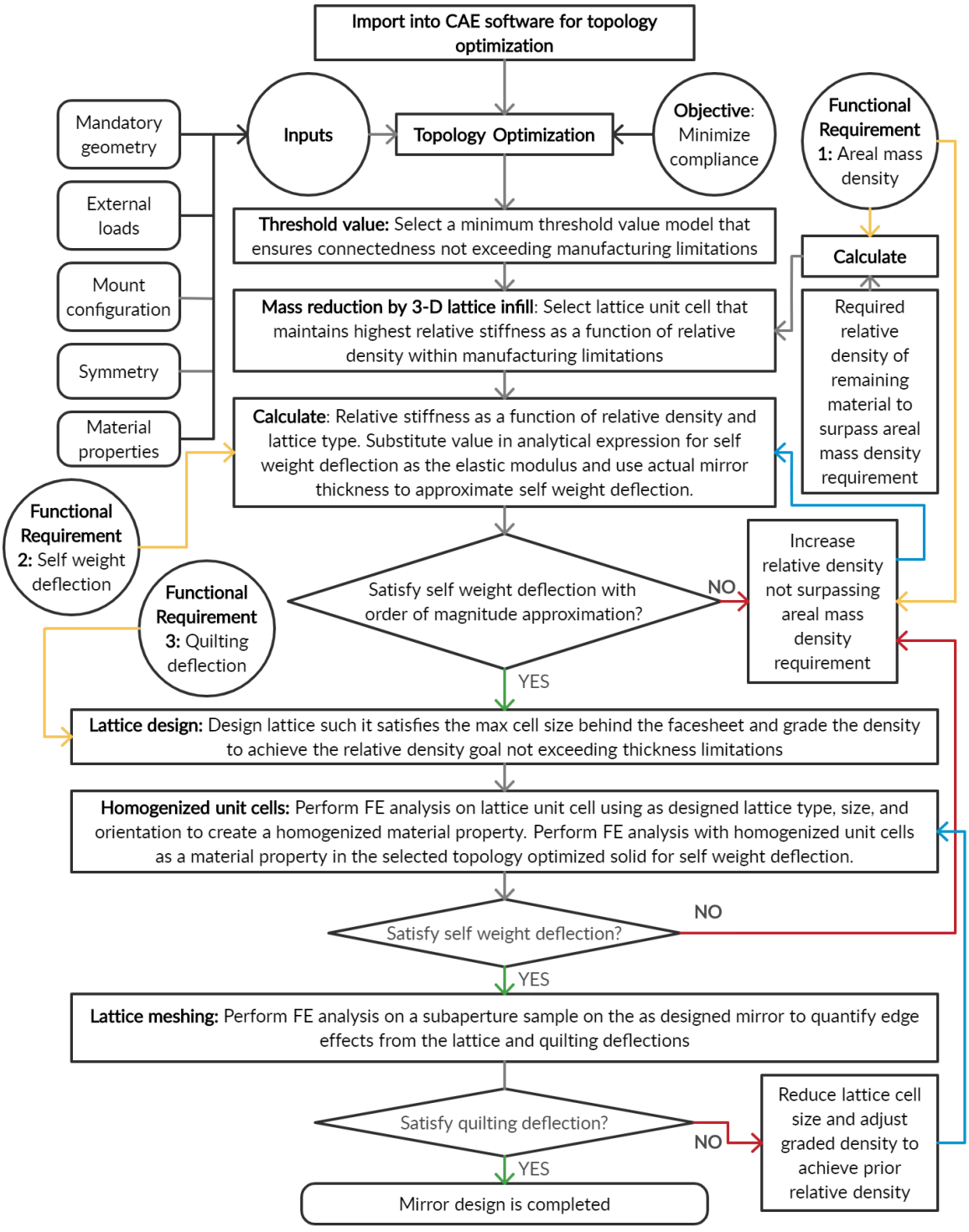

Figure 4.14: Part 2: Design methodology flowchart for the advanced mirror design considering additive manufacturing

with 1 as a full contribution and 0 as little to no contribution. Multiple topologies can be investigated by varying the acceptable threshold range. Depending on the limiting factors of the additive manufacturing method chosen, which is both material and printing machine specific, the appropriate topology can be selected. Once the topology optimized geometry is selected, further weight reduction is performed by introducing 3-D lattice structures, opposed to 2-D isogrids. Along with areal mass density reduction, the 3-D lattice structures will have an effect on the flexural rigidity of the mirror and the surface quilting. Here, we utilize the previously defined analytical equations combined with CAE to discuss the trade-offs in selecting a lattice structure such that an increase in the specific stiffness of the mirror is achieved while also reducing the quilting deformations. After the design of the mirror is completed, a secondary FE analysis is performed to independently confirm the chosen design parameters meet the functional requirements.

4.5.1 Topology optimization from external load cases

The initial solid model was generated and imported into CAE software for the topology optimization process. A unique differentiation between the analytical design method versus the CAE design method at this point is the calculation of bending stiffness or flexural rigidity. The analytical model for flexural rigidity must assume a homogeneous, linearly elastic component, thus leading to an equal distribution of stiffening elements over the entire mirror. However, shown previously, the assumptions used in the analytical methods resulted in a mirror with more mass than needed to achieve the stiffness requirements, only confirmed after a FE analysis. A CAE design method instead develops a compliance matrix containing all discrete elements in the mesh which is minimized during the optimization. This enables a localized distribution of stiffness only where required on the mirror and mass reduction where the material does not have a significant contribution to the overall stiffness. This is represented by the threshold elements in the optimization output. Therefore, the

main purpose of the topology optimization is to provide the designer with the internal force loop through the mirror from the external loads, thus showing where stiff elements are required in the design.

Identical to the traditional mirror FEA analysis, the model was meshed with solid tetrahedral elements with planar symmetry. The mount pads were kinematically constrained using local oriented coordinate systems that constrain two translational degrees of freedom per mount, representative of a 3 vee - 3 ball kinematic mount. Combined loading was applied for both gravitational acceleration to the solid body and polishing pressure in the optimization. The topology optimization successfully converged to the displacement requirements within 25 iterations. Multiple topologies are shown in Fig. 4.15 with the minimum threshold value shown, along with the input geometry. A topology with a minimum threshold value of 0.6 was selected, which contained excessive elements only to ensure connectedness of the structural loop, assurance that minimum thickness values were not exceeded, and to allow for further design work to reduce the mass. The smoothed result combined with the solid mount pads and facesheet is shown in Fig. 4.16.

An interesting observation to highlight is the connectedness between the mounting pads in the topologies shown in Fig. 4.15. This is a result of the kinematic constraint boundary condition. With each mounting location only constraining 2 degrees of freedom, the mirror requires high bending stiffness to connect the force loop from one mount point to the next in order to achieve the displacement requirements. A full encastre boundary condition at each mount point would result in stiff elements only near the mount with only the facesheet as a connected structure between the mounts, similar to work previously published [78]. Thus, a boundary condition not representative of the actual mount condition could significantly underestimate the required mirror stiffness when used in practice.

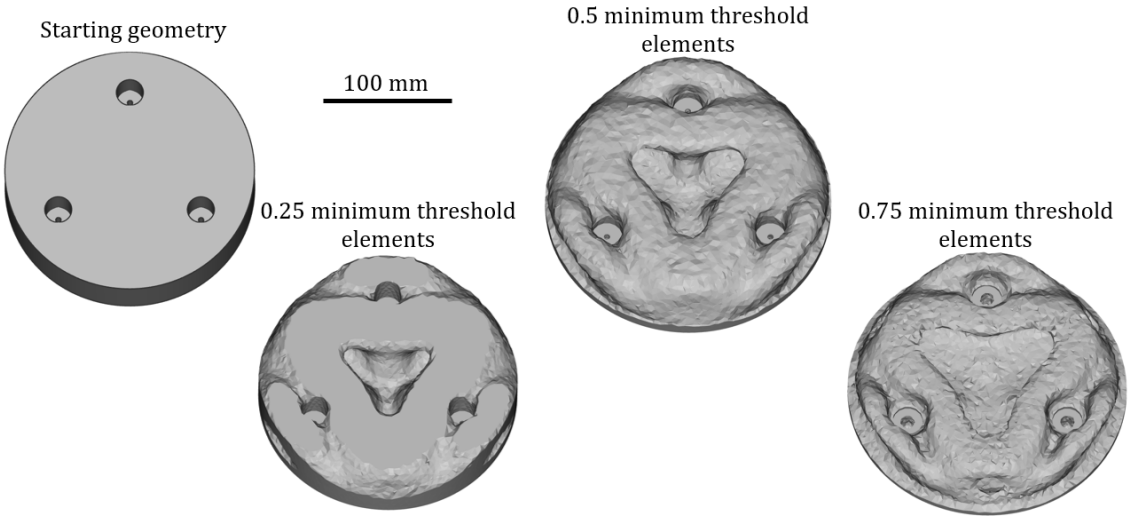

Figure 4.15: The topologies after convergence on the minimum compliance functional requirement at different remaining threshold values. A threshold value of 0 represents an element in the mesh with little to no contribution to minimizing the compliance, while a threshold value of 1 represents an element that has a maximum contribution in minimizing compliance.

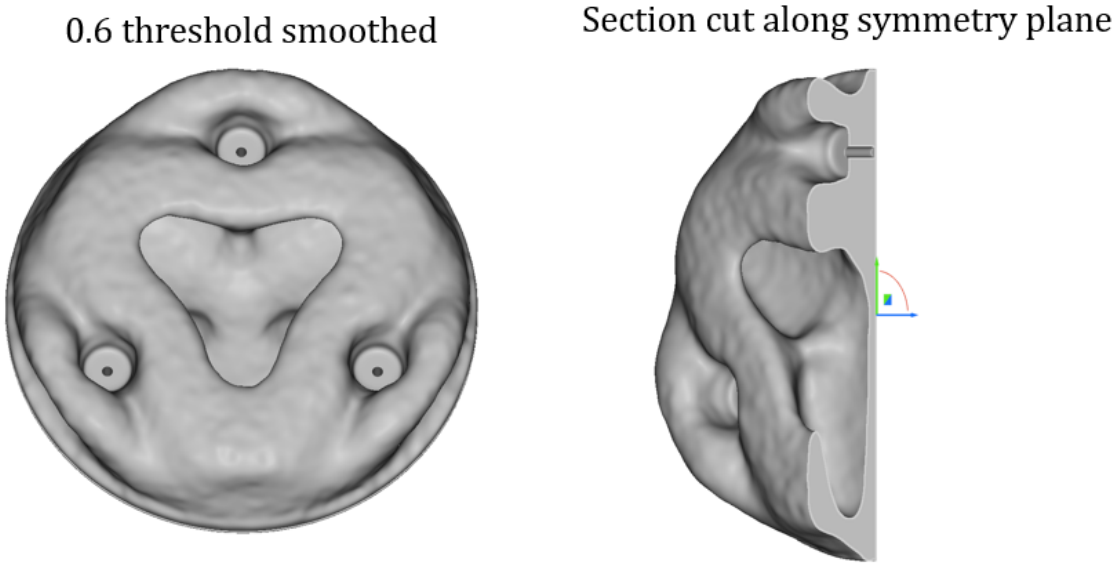

Figure 4.16: The 0.6 minimum threshold element geometry was selected for further design work. This geometry was selected to ensure connectedness through the structural loop and allowance for further mass reduction by lattice infills.

4.5.2 Weight reduction by lattice infill

The mirror with the selected topology optimization surpassed the displacement requirements, however it exceeded the areal mass density requirement. In similar fashion to the traditional design, a reduction of the remaining available volume must be performed in order to meet the mass requirement. The traditional design and previous state of the art manufacturing techniques were limited to a 2-D method with discrete constant cells, of which a solidity ratio was used as the design parameter. With current state of the art additive manufacturing, we can reassess this method with a volumetric approach using 3-dimensional lattice structures. The solidity ratio expanded to three dimensions is described as relative density for lattice structures or foams [77]. Using certain lattice geometries can also reduce the largely geometric anisotropy seen in isogrid designs.

We know from Eq. 4.6, confirmed to be accurate on the traditional design, that the quilting deflection is dependent on the facesheet thickness and the cell area behind the facesheet. Shown in Fig. 4.7 for a 1 mm facesheet in SiC, any cell size less than 10 mm would result in meeting the threshold requirement of 43 nm. This creates a maximum unit cell size for the lattice. Because the cell geometry far from the facesheet does not have a significant contribution to the quilting, the lattice geometry can vary as a function of distance from the facesheet,. This allows for a graded relative density as a function of distance from the facesheet. A similar idea has been shown to be effective for reducing quilting deflections by using stochastic foam cored mirrors. However, an intrinsic property of stochastic foam is a higher compliance compared to an ordered lattice structure, thus leading to a lower overall flexural rigidity [68, 77].

Self weight deflection is shown to be inversely proportional to the specific stiffness, Eq. 4.2. However, the specific stiffness is both, a material design parameter and a geometric design parameter for a lattice structure. The combination of these is known as the relative stiffness, which is proportional to the relative density of the lattice and

lattice type. The SiC provides a high material specific stiffness E/ρ, however the unit cell design and size of lattice infill will provide the geometric contribution to the relative stiffness. Al-Ketan et al. provided empirical data on multiple lattice topologies, reporting the relative stiffness values for each [79]. Of those tested, the sheet diamond triply periodic minimal surface (TMPS) lattice topology was shown to be the least sensitive in terms of stiffness reduction as a function of relative density. Similar to selecting a topology threshold, when choosing a lattice one must understand both, the geometric limits of the additive manufacturing method and open paths for powder removal to avoid trapped powders. While out of the scope of this Chapter, Sweeney et al. provide a comprehensive foundation on metallic mirror printing limitations using multiple printing methods [61]. However, extensive work in this area is still required and is changing as new machines are developed. The SiC printing method developed by Terrani et al. uses a binder jet printing method followed by a chemical vapor infiltration [27]. Because this printing method has minimal limitations for geometry creation and the sheet diamond TPMS lattice does not contain enclosed pockets, it was a suitable candidate for further analysis and subsequent prototyping for experimental design confirmation in future work.

Using implicit modeling software, the TPMS sheet diamond unit cell array was defined in cylindrical coordinates to provide a rotational symmetry of the lattice on the topology optimized mirror. An azimuthal frequency of 30 units were used to create a maximum spacing of 10 mm at the aperture edge. A graded relative density was also used which varied the thickness of the lattice elements from 4 mm to 1 mm starting from the back of the facesheet to 8 mm. After 8 mm, the lattice thickness was held constant at 1 mm. This combination resulted in no cells in any direction greater than 10 mm and the largest spacing behind the facesheet of 6 mm, thus meeting the threshold value derived from the analytical equation for quilting deflection. The slope of this graded density transition was not quantified as optimal, however it resulted in

a relative density value of 0.25.

From Al-Ketan et al. [79], we can approximate the relative stiffness for the sheet diamond TMPS lattice by the square root of the relative density. Substitution of this value in Eq. 4.2 for elastic modulus and using the actual mirror thickness as the equivalent bending thickness, we approximate the self weight deflection to be 4 nm RMS. This approximation does not account for the complex topology optimization, however the order of magnitude approximation is a useful step to progress towards a FE analysis confirmation.

The high azimuthal cell frequency of the cylindrical TPMS model used resulted in some unrealizable artifacts for manufacturing at the center point of the mirror. To resolve this, the center was removed and replaced with another sheet diamond lattice with less azimuthal cells to ensure the center point was well behaved. The final model includes a 1 mm thick facesheet, however is hidden in the figure to better show the lattice structure behind the solid facesheet. Figure 4.17 shows discrete slices of the lattice starting from the back side of the solid 1 mm facesheet in Fig. 4.18. The final model has a mass of 0.45 kg, an estimation of self weight deflection of 4 nm RMS, and a quilting deflection of less than 10 nm PV.

4.5.3 Advanced mirror design FEA confirmation

The final mirror design that combines both topology optimization and lattice infill was post processed with a finite element analysis to confirm all requirements have been met. However, it is computationally expensive to create a compliance matrix with the amount of elements required to make a refined mesh on the lattice. Therefore, two methods were used to perform the analysis. The first analysis confirms the self weight deflection requirements and the second analysis confirms the deflection from polishing pressure.

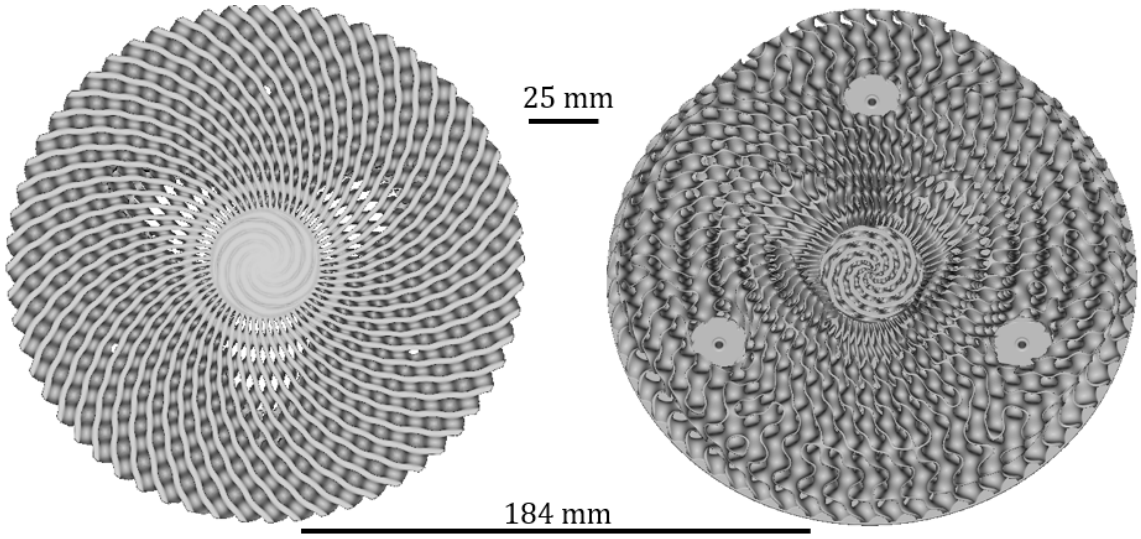

Figure 4.17: Mirror design combining the 0.6 threshold topology optimization output with a cylindrical TPMS sheet diamond lattice structure

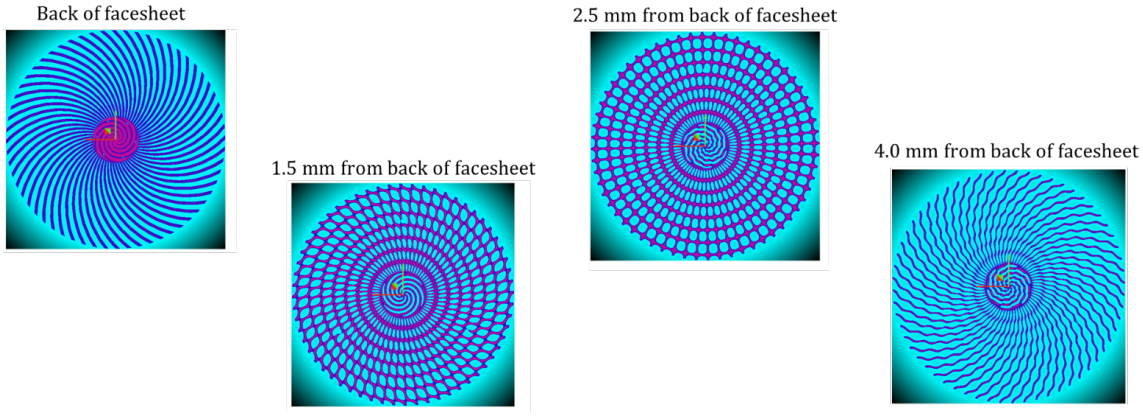

Figure 4.18: Discrete slices showing the TPMS lattice structure behind the facesheet

4.5.3.1 Self weight deflection FEA analysis

To quantify the self weight deflection by FE analysis, a compliance matrix was created by a separate finite element analysis on a unit cell of the lattice used. This compliance matrix is used in a solid version of the mirror (Fig. 4.16) as the elastic modulus material property for the volume the lattice occupies. This solid attribute in the FE model known as a homogenized material unit cell, which provides an accurate representation of the stiffness of a lattice without having to mesh a large lattice scaffold. The homogenization method is widely used to perform analysis on advanced lattice structure designs [80, 81, 82]. To perform an appropriate homogenization, the relative density of the lattice, the lattice type, and the orientation of the lattice must be known. The relative density is simply the ratio of the mass of the lattice over the solid, both of which are known. The homogenized unit cell uses the same relative density, thus providing the relative stiffness which can then be used on the larger model for analysis. An adjustment to the lattice results in a new relative density, where the homogenized unit cell can then also be updated for analysis. However, homogenization will not reveal edge effects from the lattice spacing, such as quilting deflections. To quantify the quilting deflection, another method was used and is described in the following section.

The homogenized model was analyzed identically to the traditional design in Sec. 4.4.4. The finite element mesh used solid tetrahedral elements with 4 mm edge lengths combined with a quadrangulate surface mesh used for post processing. A gravitational acceleration load with the force vector generated by the $1g$ acceleration value acting on the mass of each tetrahedral element. The native FEA solution is shown in Fig. 4.19(a), with the post processed surface data shown in Fig. 4.19(b-d).

Here, we can see the effect from the topology optimized structure in the residual map, similar to the isogrid structure in the traditional design, however the deflection is an order of magnitude less than the functional requirement. From Fig. 4.19 it is

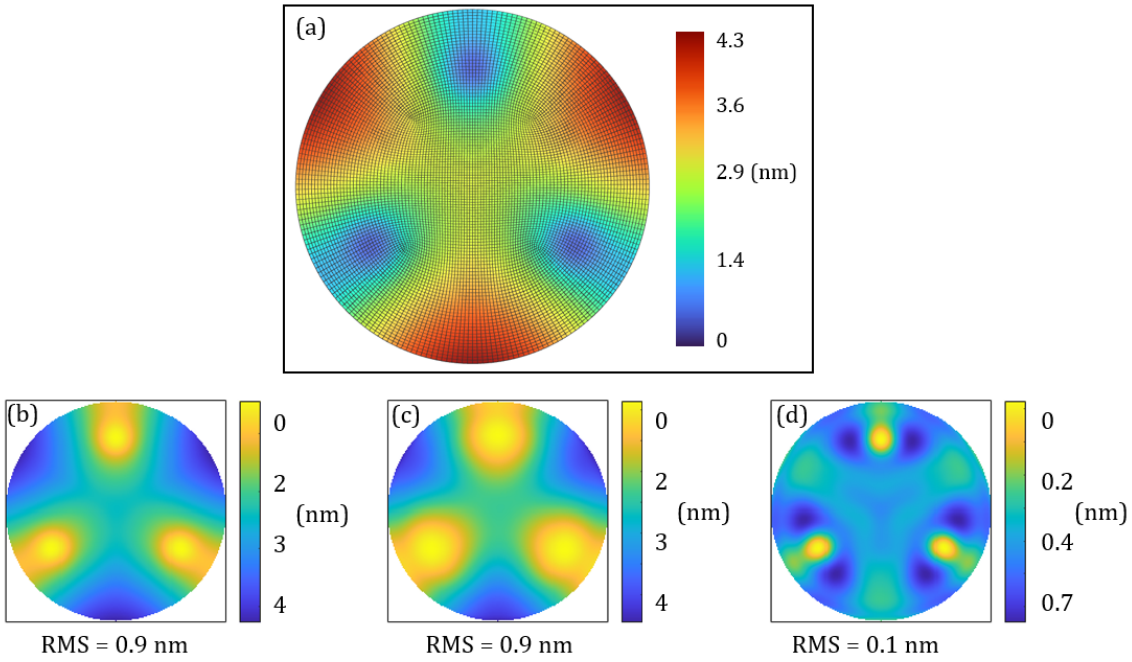

Figure 4.19: (a) Topology optimized mirror with TPMS lattice homogenization gravitational acceleration load FEA in native FEA output, (b) Raw imported surface data from quadrangulate mesh, (c) Zernike fit, (d) Zernike fit removal from the data set, or residual map

shown that the RMS and PV deflection is less than the functional requirement and closely agrees with the approximation from the substitution of relative stiffness in Eq. 4.2.

4.5.3.2 Surface quilting from lattice

The higher order quilting surface deflections do not require a full aperture analysis to quantify the edge effects from the lattice if the lattice at the surface has symmetry. While this was performed on the traditional mirror design, a sub-sample of the aperture over some cells clearly would have been sufficient to provide enough information on the quilting deflection. Because the ability to perform meshing on large lattice structures is limited to a homogenized method, a sub-sample approach was used to analyze the quilting deflection from polishing on the lattice supported mirror, where direct meshing on the lattice could be performed.

A solid tetrahedral volume mesh was created over a 25 mm circular section of the

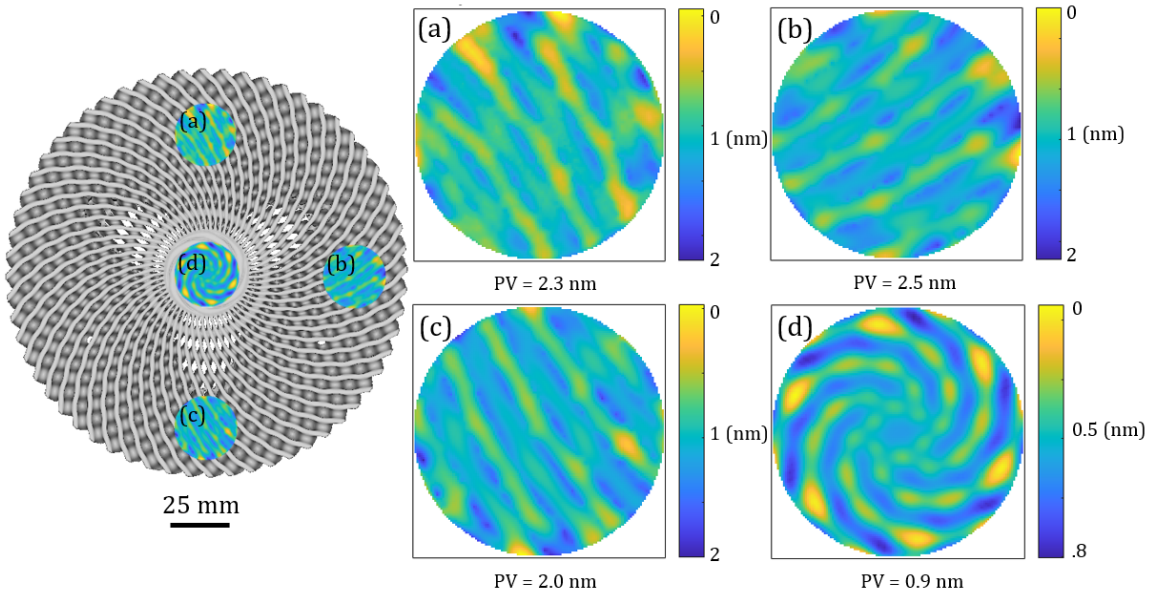

Figure 4.20: Residual maps from polishing the lattice backed mirror. The locations of each map, (a) 12 o'clock, (b) 3 o'clock, (c) 6 o'clock, (d) center. The peripheral samples (a,b,c) are at the same radial distance which is equal to the mounting radial distance.

lightweight mirror at four different locations. One location was directly over a mount pad, with two more 90 degrees apart at the same radial distance, and one at the center of the mirror. The same conditions as the traditional mirror were applied, with a 42 kPa polishing pressure over the sub aperture sample. The four samples were post processed identically to the traditional mirror and the residual deflection maps are shown in Fig. 4.20.

As a result of the rotational symmetry, each of the three maps look near identical with an average peak to valley displacement of only 2.3 nm and 0.3 nm RMS compared to the traditional mirror with 42 nm and 9 nm respectively. Using Eq. 4.7, the Strehl ratio from these quilting displacements would be greater than 0.98. The striations in the three maps match directly to the spiral rib portion of the TPMS lattice structure just behind the facesheet. This is another confirmation that the geometry further from the facesheet has a negligible effect on surface quilting. With both, the self weight deflection and quilting deflection within specification, the design of the mirror

is complete. The overall mass of the final mirror is 0.45 kg, equating to a mass per unit area of only 15.5 kg/m^2.

4.6 Conclusion

Here we provided two systematic design methodologies to create lightweight mirrors. The first design method used a series of analytical expressions with discussions on key trade-offs for the design parameters to achieve the functional requirements outlined in Sec. 4.2. The second method established a workflow for combining topology optimization and lattice structure infills with analytical estimations to achieve the functional requirements. During this method, key waypoints were identified when considering design for manufacturability. Each methodology was applied through a case study which concluded with an independent FE analysis for design confirmation. A summary of each mirror and the evaluation in performance for each functional requirement is shown in Table 4.1.

The traditional mirror design, while meeting all functional requirements, was outperformed by the mirror designed for advanced manufacturing for each requirement. The advanced mirror design had an overall reduction of both areal mass density and self weight deflection, 24% and 25% respectively, which is representative of a higher specific stiffness than the traditional design. The increase in specific stiffness is a direct result of the topology optimization with the appropriate boundary conditions, where the optimization provided a distribution of stiffness only where required. This is contrary to the traditional design that assumes an even distribution of stiffness over the entire aperture to develop the analytic expressions for self weight deflection. While the first natural frequency of the mirrors were not discussed, because the frequency is proportional to the specific stiffness of the mirror, it can be inferred that the mirror with a higher specific stiffness also has a higher first natural frequency, considering the aperture size, thickness, and mounting conditions are the same.

The overall quilting deflection was reduced by 94% on the advanced lattice struc-

Table 4.1: Summary of the functional requirements for both mirror design case studies and the resulting performance improvement with the advanced design

Functional Requirement	Traditional Mirror	Advanced Mirror	Improvement
m/A: 20 kg/m^2	20.6 kg/m^2	15.5 kg/m^2	24%
δ_{RMS}: 5 nm RMS	1.2 nm RMS	0.9 nm RMS	25%
δ_q: 43 nm PV	42 nm PV	2.3 nm PV	94%

ture design compared to the traditional isogrid design. This improvement can only be accomplished by reducing the cell size behind the facesheet or increasing the facesheet thickness. However, the increase in facesheet thickness results in a significant weight increase with little benefit to overall mirror stiffness. The lattice infill allowed for a decrease in cell size to a level that also allowed for a decrease in facesheet thickness compared to the traditional design, thus reducing both the quilting deflection and areal mass density. The generation of a lattice structure with 3-dimensional parameters allowed for a smaller cell size where required and larger elsewhere, shown with by the graded relative density.

The lattice structure also provides unique flexibility to the designer, including but not limited to the lattice unit cell geometry, unit cell orientation, and graded density. A unique design feature that can have a direct effect on optical performance is the lattice unit cell frequency behind the facesheet. The case studied showed a rotationally symmetric cell structure behind the facesheet with an azimuthal spatial frequency of 30 cycles per aperture, however depending on specific spatial frequency requirements from the optical design this can be modified with either more or less frequency. In a traditional design, this is was an unimaginable design parameter when considering all other functional requirements. Utilization of this unique capability to alter image performance in a deterministic way could provide interesting results in future studies.

The advancement of additive manufacturing has proven to be a disruptive technology for component design in almost any field of engineering. This advancement was leveraged to develop a new design methodology and provide a paradigm shift in

the mirror preform design, resulting in a higher performance mirror that is readily prototyped on the order of days.

CHAPTER 5: CONCLUSION

This work shown in this dissertation addressed the four key aspects mentioned en route the creation of the next generation advanced reflective optics. These aspects were addressed by (i) a new optic mounting system with precision placement for the optic used for both manufacture and metrology, (ii) the identification and fundamental process grinding data for a potential new process chain for SiC mirrors, (iii) systematic design methodologies for both isogrid backed mirrors and additively manufactured mirrors.

Chapter 2 provided a new design for a kinematic mount that can be used through the entire process chain of fabricating the optical surface. This addresses the iterative process chain required for the manufacture of high precision optics. The mount design first provides a low stress constraint to the mirror, thus reducing the uncertainty for different mount induced deformations during the manufacture-metrology feedback loop. An additional kinematic mount can be installed on metrology equipment, such as a profilometer or interferometer, allowing for a rapid inspection of the mirror figure without removing the optical cell, and in turn the global reference frame from the diamond turning machine. During manufacturing, the diamond turning machine kinematic errors are imprinted on the mirror, thus the ability to move the mirror between mounting platforms for independent machine metrology will enable simple toolpath corrections for these errors, assuming the errors repeat, rather than timely alignment procedures of the machine tool axes.

The mount configuration was designed to account for the effects from the process forces. The design leverages the process forces to increase the mount stiffness by orienting the preload direction with the dominant direction of the process force. Cur-

rently, the preload direction is aligned with the dominant force for diamond turning. For process forces with a different dominant force direction, a new mount design can be accomplished by rotating the joints to align the process force magnitude with the preload force.

The optical cell acts as the global reference system for the mirror, thus eliminating the need for ancillary fiducials on the optic. The reference datums are machined in the same manufacturing setup as the mirror figuring, thus transferring the precision of the diamond turning machine into the reference features. Because the exact constraint design of the mount is very repeatable, this results in a low uncertainty for the location of the mirror in the global reference system of the optical cell. The datums on the optical cell also act as transfer datums when the optic and optical cell system is installed in an instrument. The repeatability of the mount quantifies the uncertainty of the placement of the optic relative to the transfer datums on the optical cell. Thus, measurements can be performed on the housing of the instrument and the coordinate system location and uncertainty for the mirror is known.

The kinematic mount system was fabricated and used for diamond turning a 270 mm freeform mirror. The test mirror was diamond turned and removed from the optical cell. The optical cell was installed on a Moore UMM and the mirror was installed in the optical cell for figure metrology, shown in Fig. 5.1. The ongoing figure metrology research for the freeform mirror is performed by other graduate research students. However, the surface texture of the diamond turned mirror is less than 10 nm RMS without polishing, a result of adequate mount stiffness when considering the processes forces. Future work using this mount would require a reported figure error measurand followed by a new toolpath generation to correct systematic machining errors introduced by the diamond turning machine. Further, research on the thermal stability of the diamond turning machine must be addressed to ensure a systematic correction attempt.

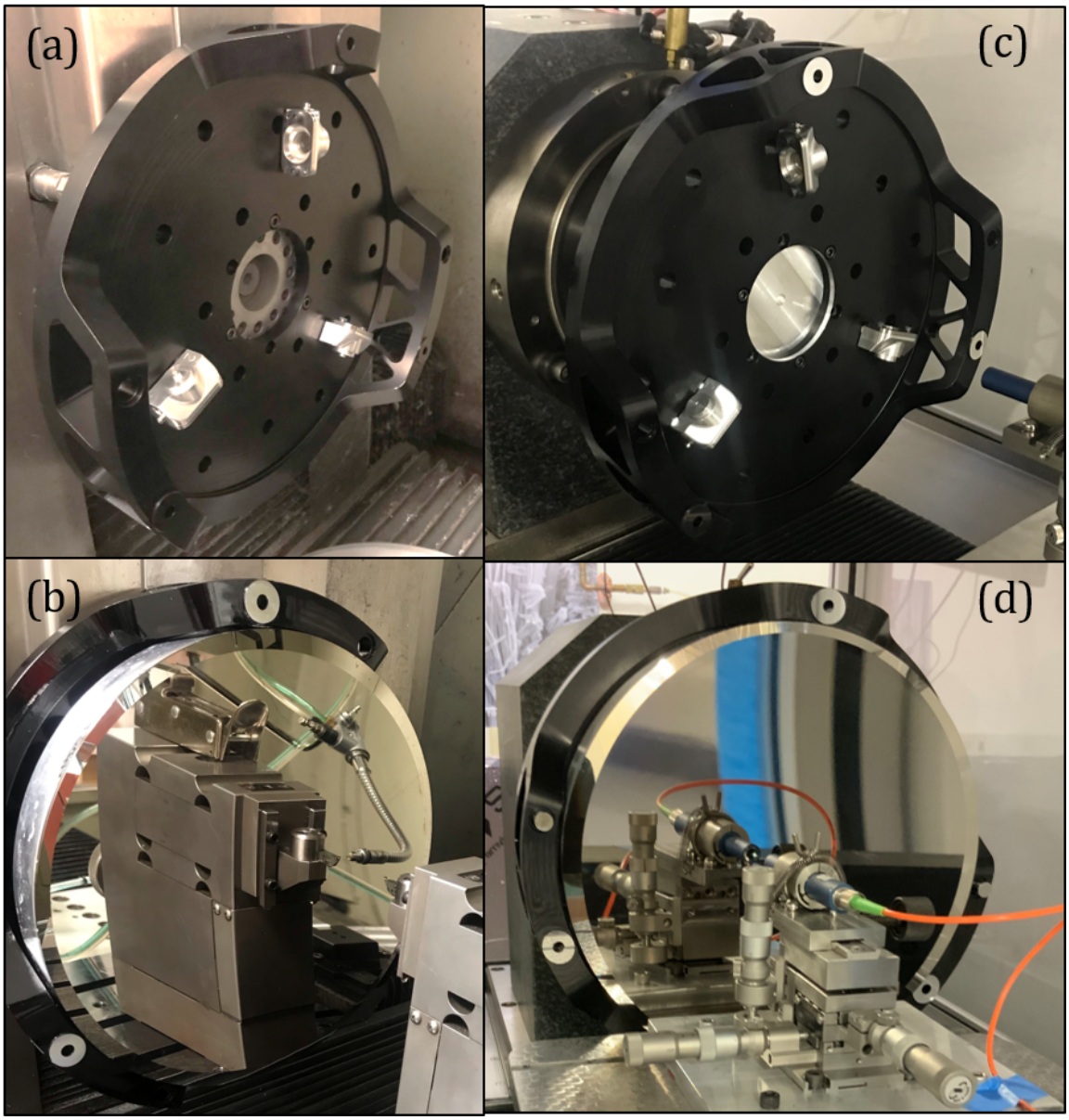

Figure 5.1: Manufacture and measurement set up for 270 mm freeform optic with (a) the optical cell is installed on the diamond turning machine. (b) A 270 mm freeform mirror was diamond turned followed by diamond turning of the reference features on the optical cell. (c) Shows the optical cell remounted on a Moore UMM used for figure metrology. The reference features on the cell align the cell to the UMM and the confocal probe. (d) The 270 mm freeform mirror is installed in the optical cell with the aligned confocal probe used for figure metrology.

A supplementary section has been added in Appendix A.1 with a MATLAB® script to design and analyze a torsional kinematic mount. Appendix A.1 also includes a script to calculate the effect of the process forces on the preload, stiffness, and groove resultant forces.

Chapter 3 introduced a new grade of additively manufactured SiC, designed for the use in nuclear applications, to the optics community. In this Chapter, the author provided fundamental grinding research on the AM SiC for reflective optics. The process forces were measured and compared to the process forces of common used CVD SiC in optical applications. The AM SiC in the current state was shown to have lower forces compared to the CVD SiC, however it was discovered that the same process parameters can be used for both materials. The results for high speed grinding with a precision machine tool was promising for near net finishing, achieving specular surface finishes on both materials. The high speed grinding was shown to have lower specific grinding energy while the surface damage during rough grinding appeared constant at any chosen wheel speed, thus rough grinding can be performed with higher removal rates than first assumed.

The hypotheses for the lower forces include (i) dislodgment of the large alpha-particles in the CVI matrix, (ii) differences in grain orientation between the CVD SiC (columnar) and CVI SiC (random), (iii) a lower flexural strength due to residual porosity. The specular surface texture was limited by residual porosity in the AM SiC, however the CVD SiC achieved less than 10 nm RMS with a precision machine tool with a ceramic roller bearing spindle, thus the limitation was due to the material and not the machine or machining parameters.

The additive method enables a rapid prototype of a mirror design with a production time on the order of days. Extreme freeform shapes are readily produced with the binder jet process with potential to reduce grinding time after infiltration. However, to create these shapes for optical applications future work must include reducing the

surface porosity to increase the surface texture quality and increasing the precision of the binder jet machines to reduce the grinding stock.

The most pressing research area for the use of this material for reflective optics is increasing the surface quality. There are two techniques that could increase the surface quality worth investigating. The first is applying a re-coat, or a second furnace run after a rough grinding process on the component. This is the same process chain used on SiC mirrors made by any method other than just CVD. The mirror preform is made from a substrate material such as graphite or HIP SiC, reaction bonded or sintered, rough ground to form, and then CVD coated. However, this method introduces additional variables, such as coating delamination, trapped sub-surface damage, and a sharp transition in thermo-mechanical properties at the interface. The second technique involves an extended duration run in the furnace during infiltration. As the porosity voids are filled during infiltration, the outer coating continues to grow with time.

A study was conducted using the second method, with samples kept in the furnace for an extra 24 hours. The samples were then mounted in the machine and rough ground at depths of 5 µm until the surface was uniform and planar. A single 10 µm finish pass was performed on the sample using the same parameters discussed in Chapter 3. The samples were measured with a Zeiss Smartproof 5 confocal microscope with both a 20x and 50x objective with a 560 µm and 230 µm square field of view, respectively. The original sample was also remeasured with the new microscope for a direct comparison. The surface measurements were processed with a plane removal, Gaussian band pass filter with cutoff wavelengths of 80 µm and 2.5 µm. Figures 5.2 and 5.3 show the extended run sample and the original samples. The first observation that can be made is the smaller porosity void size compared to the original. Also, the peak to valley scale bars have changed by an order of magnitude. The RMS surface roughness has improved by a factor of 4.6 for each measurement. This result, while

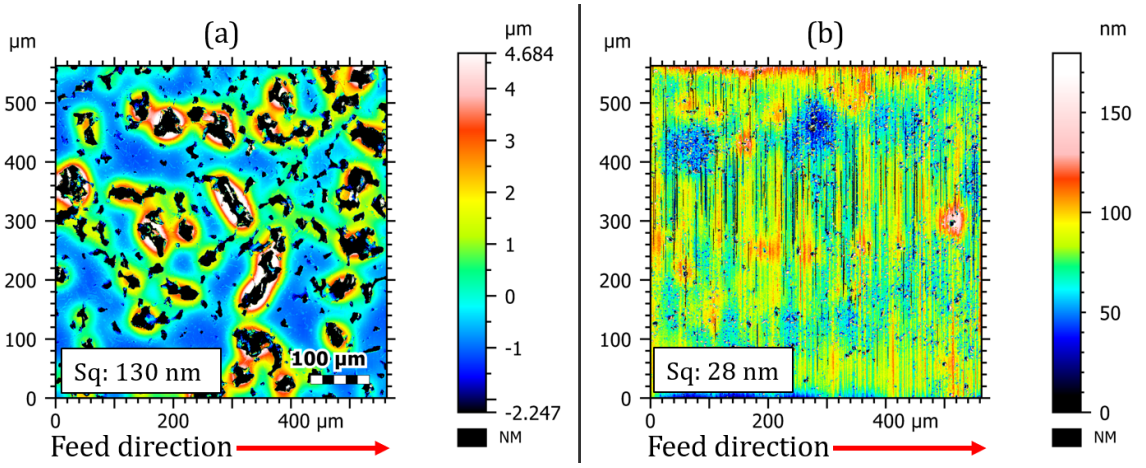

Figure 5.2: 20x objective measurements. (a) The original sample remeasured with the standard furnace run time. (b) The extended run time sample with an extra 24 hours of furnace time. The extra 24 hours resulted in a 4.6x improvement in RMS surface roughness.

still not acceptable for high quality mirrors, is a promising step towards the material's use in optical applications.

Once the surface quality research nets a surface finish of optical quality for visible incident wavelengths, further research in the material properties can also be investigated. With the flexibility of the binder jet additive process, heterogeneous material combinations are possible. Research on "engineered materials", such as coated chopped carbon fiber or diamond impregnation to alter the coefficient of thermal expansion or melt infiltration with Silicon for an increase in thermal conductivity are all possible. Additional future work may also include the grinding mechanics and wheel wear with the cross axis toolpath strategy. The average diamond grain in the grinding wheel will traverse a helical path through the workpiece while in a cross axis grinding configuration, thus extending the length of cut compared to a parallel grinding configuration. Knowing the true length of cut, and subsequently the duration the cut, per diamond grain is useful for wear studies among others. For this reason, a supplement derivation for the helical distance covered per grain once per revolution for the major diameter of the wheel is provided in Appendix B.

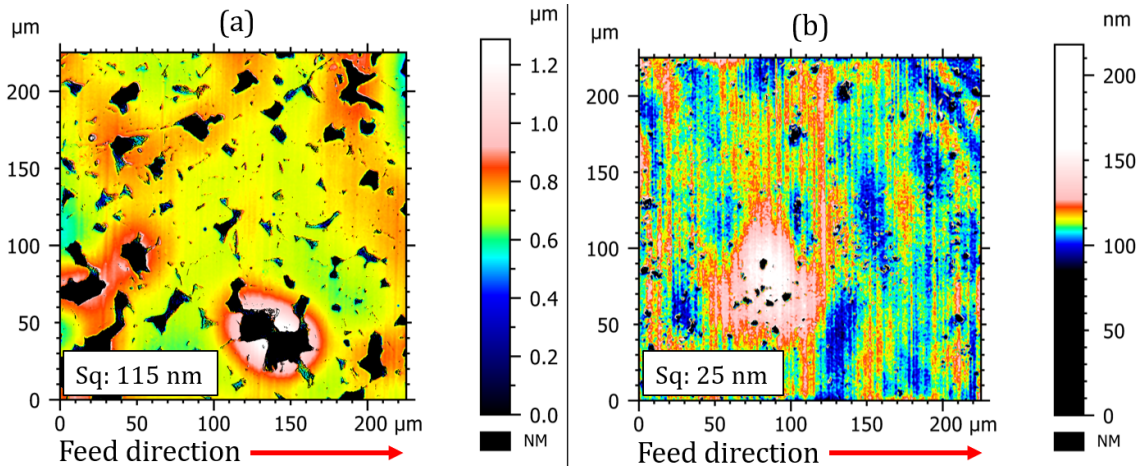

Figure 5.3: 50x objective measurements. (a) The original sample remeasured with the standard furnace run time. (b) The extended run time sample with an extra 24 hours of furnace time. The extra 24 hours resulted in a 4.6x improvement in RMS surface roughness.

With the positive progression in surface quality of the additive SiC material, a systematic engineering methodology was developed to leverage this material process chain for a higher performance lightweight mirror in Chapter 4. However, while the material development still does not meet specification for a visible spectrum incident wavefront, the design methodology is a parallel and material agnostic workflow. Thus, Chapter 2 and 4 can be combined with NiP coated Titanium or Aluminum additively manufactured lightweight mirrors that mount in the kinematic mount system for iterative diamond turning and metrology. An example mirror preform has been printed in Ti-6Al-4V with the same geometry as the SiC mirror designed in Chapter 4 and is shown in Fig. 5.4.

The mirror was printed on a ARCAM EBM additive machine in 12 hours and used less than 1 kg of powder including lost powder in recovery. The mirror preform has an additional 1 mm of stock on the facesheet, mount points, and threaded mount holes. The mirror will require post-machining on these areas to create a planar surface and mounting datums prior to NiP coating. After coating, the mirror can be mounted on a diamond turning machine for a facing operation followed by a full aperture polish.

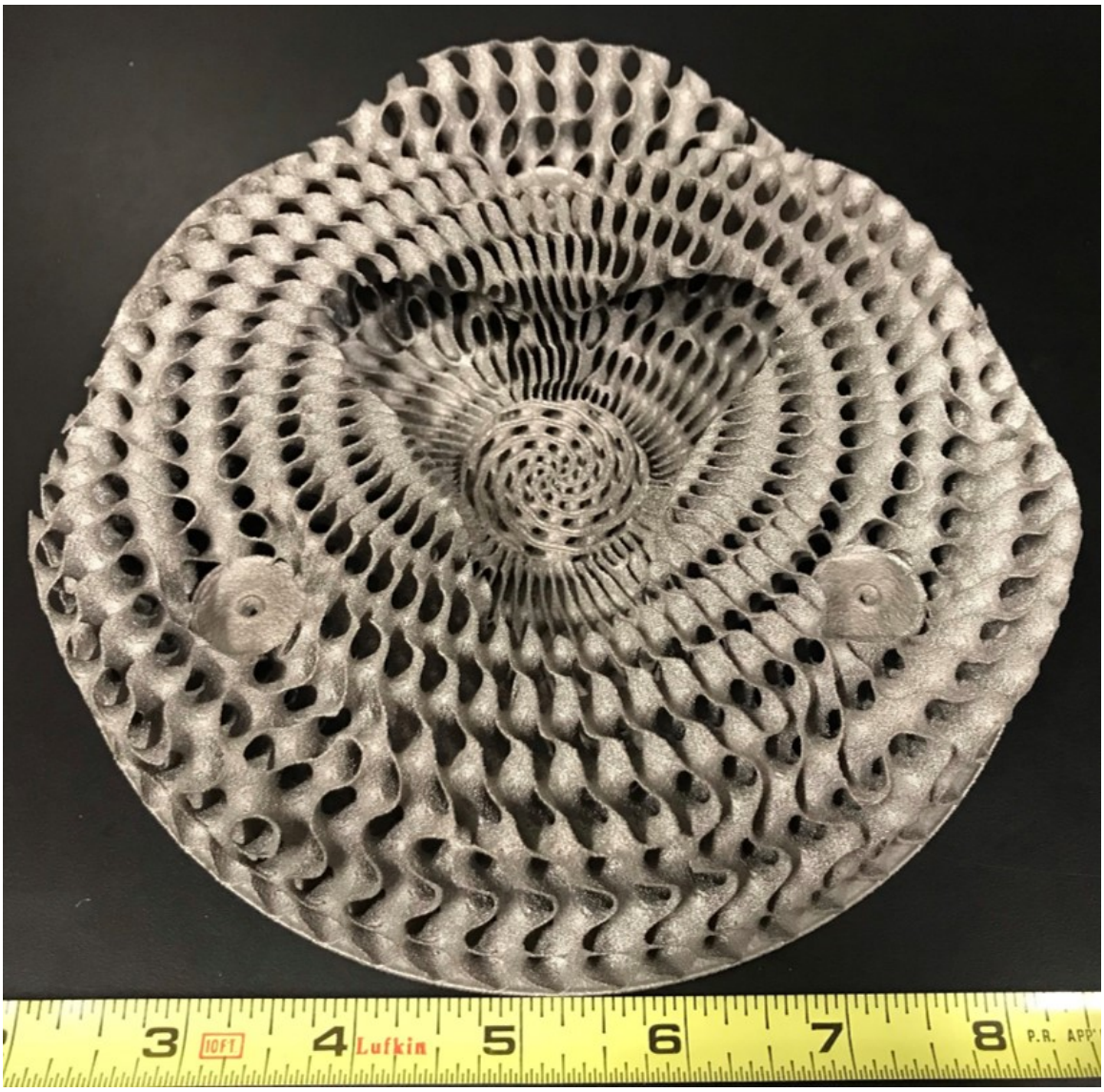

Figure 5.4: A Ti-6Al-4V mirror preform additively manufactured on an ARCAM EBM machine. The mirror is a replication of the mirror designed for SiC, however the intention is a proof of concept that will be NiP coated on the optical surface, diamond turned, and polished. The design methodology developed in Chapter 4 is agnostic to the material selection and expected deformation maps are readily created with updated material properties.

The model in Chapter 4 is readily modified with the final actual facesheet thickness and material properties along with updating the polish pressure to predict the MSF print through on this Titanium mirror substrate as work progresses. Appendix A.2 provides the code developed to process the FEA deformed sufaces and curve fit with Zernike polynomials used in Chapter 4.

The most pressing future work for the additively manufactured mirror is quantifying the boundary conditions or process limitations of each additive process. However, significant work has been done to quantify slope limitations, unsupported sections, and thermal distribution to reduce part deformation in the additive community. To best leverage this pool of knowledge, a concurrent engineering developmental team for additively manufactured mirror preforms should include subject matter experts from each step of the process chain during the design process to ensure the manufacturing limitations are discussed. Other future work could include actuators and sensors for small intentional deformations to change the direction of local optical surface normals for wavefront correction. A potential revisitation of the original purpose for SiC mirrors is always a possibility. If the need for liquid-cooled mirrors return, the additive method is a strategic advantage to optimize the conformal cooling passages along the freeform surface.

With further maturation of the new process chain for additively manufactured silicon carbide, discussed in Chapter 3, the apotheosis of this work is a future research project on the implementation of the combination the Chapters 2-4, with an additively manufactured, high efficiency lightweight silicon carbide mirror with the optical surface fabricated, measured, and corrected using the new kinematic mount platform. The work discussed in the this dissertation provided a systematic framework to generate state of the art reflective optics.

REFERENCES

[1] R. R. Donaldson and S. R. Patterson, "Design and Construction of a Large Vertical Axis Diamond Turning Machine," in *Proc. SPIE 0433, Contemporary Methods of Optical Manufacturing and Testing* (G. M. Sanger, ed.), vol. 0433, pp. 62–67, International Society for Optics and Photonics, dec 1983.

[2] S. R. Patterson and E. B. Magrabl, "Design and testing of a fast tool servo for diamond turning," *Precision Engineering*, vol. 7, no. 3, pp. 123–128, 1985.

[3] G. E. Davis, J. W. Roblee, and A. R. Hedges, "Comparison of freeform manufacturing techniques in the production of monolithic lens arrays," in *SPIE Optical Manufacturing and Testing VIII* (J. H. Burge, O. W. Fähnle, and R. Williamson, eds.), vol. 7426, p. 742605, SPIE, aug 2009.

[4] E. Brinksmeier, Y. Mutlugünes, F. Klocke, J. Aurich, P. Shore, and H. Ohmori, "Ultra-precision grinding," *CIRP Annals*, vol. 59, pp. 652–671, jan 2010.

[5] K. P. Thompson and J. P. Rolland, "Freeform optical surfaces," *OPN Optics & Photonics News*, pp. 30–35, 2012.

[6] A. Bauer, E. M. Schiesser, and J. P. Rolland, "Starting geometry creation and design method for freeform optics," *Nature Communications*, vol. 9, p. 1756, 2018.

[7] M. Beier, J. Hartung, J. Kinast, A. Gebhardt, F. Burmeister, U. D. Zeitner, S. Risse, R. Eberhardt, and A. Tünnermann, "Fabrication of metal mirror modules for snap-together VIS telescopes," in *SPIE/APOMA* (J. L. Bentley and S. Stoebenau, eds.), p. 963313, oct 2015.

[8] M. P. Chrisp, B. Primeau, and M. A. Echter, "Imaging freeform optical systems designed with NURBS surfaces," *Optical Engineering*, vol. 55, p. 071208, aug 2016.

[9] N. W. Horvath, I. W. Barron, J. D. Owen, B. S. Dutterer, E. Schiesser, A. Bauer, J. P. Rolland, and M. A. Davies, "Optomechanical design and fabrication of a snap together freeform TMA telescope," in *Proceedings - 32nd ASPE Annual Meeting*, vol. 67, pp. 133–138, 2017.

[10] Z. Li, X. Liu, F. Fang, X. Zhang, Z. Zeng, L. Zhu, and N. Yan, "Integrated manufacture of a freeform off-axis multi-reflective imaging system without optical alignment," *Optics Express*, vol. 26, p. 7625, mar 2018.

[11] F. Z. Fang, X. D. Zhang, A. Weckenmann, G. X. Zhang, and C. Evans, "Manufacturing and measurement of freeform optics," *CIRP Annals - Manufacturing Technology*, vol. 62, pp. 823–846, 2013.

[12] X. Zhang, Z. Zeng, X. Liu, and F. Fang, "Compensation strategy for machining optical freeform surfaces by the combined on- and off- machine measurement," *Optics Express*, vol. 23, no. 19, pp. 24800–24810, 2015.

[13] L. M. Pant, M. P. Singh, K. K. Pant, and A. Ghosh, "In process metrology of aspheric optical surfaces during sub-aperture polishing process," in *SPIE Optics and Photonics* (K. Bhattacharya, ed.), vol. 9654, p. 96540U, International Society for Optics and Photonics, jun 2015.

[14] F. J. Chen, S. H. Yin, H. Huang, H. Ohmori, Y. Wang, Y. F. Fan, and Y. J. Zhu, "Profile error compensation in ultra-precision grinding of aspheric surfaces with on-machine measurement," *International Journal of Machine Tools and Manufacture*, vol. 50, pp. 480–486, 2010.

[15] Y. E. Tohme, "Grinding aspheric and freeform micro-optical molds," in *Proc. SPIE 6462, Micromachining Technology for Micro-Optics and Nano-Optics V and Microfabrication Process Technology XII* (M.-A. Maher, H. D. Stewart, J.-C. Chiao, T. J. Suleski, E. G. Johnson, and G. P. Nordin, eds.), vol. 6462, p. 64620K, International Society for Optics and Photonics, feb 2007.

[16] A. M. Hoogstrate, C. van Drunen, B. van Venrooy, and R. Henselmans, "Manufacturing of high-precision aspherical and freeform optics," in *Proceedings of SPIE* (R. Navarro, C. R. Cunningham, and E. Prieto, eds.), vol. 8450, pp. 84502Q1 – 84502Q9, International Society for Optics and Photonics, sep 2012.

[17] M. A. Ealey and G. Q. Weaver, "Developmental history and trends for reaction-bonded silicon carbide mirrors," in *Proceedings of SPIE - The International Society for Optical Engineering*, vol. 2857, pp. 66–72, 1996.

[18] L. D. Buelow, F. R. Hassell, and C. Lieto, "Overview of fabrication processes for uncooled laser optics," in *SPIE Silicon Carbide Materials for Optics and Precision Structures* (M. A. Ealey, ed.), vol. 2543, pp. 50–58, oct 1995.

[19] S. J. Kishner, G. J. Gardopee, M. B. Magida, and R. A. Paquin, "Large stable mirrors: a comparison of glass, beryllium, and silicon carbide," in *Proc. SPIE 1335 Dimensional Stability*, vol. 1335, pp. 127–139, 1990.

[20] M. A. Ealey and J. A. Wellman, "Ultralightweight silicon carbide mirror design," in *Proceedings of SPIE - The International Society for Optical Engineering* (M. A. Ealey, ed.), vol. 2857, pp. 73–77, nov 1996.

[21] C. J. Shih and A. Ezis, "Application of hot-pressed silicon carbide," in *Proc. SPIE 2543, Silicon Carbide Materials for Optics and Precision Structures*, vol. 2543, pp. 24–37, 1995.

[22] M. I. Anapol, P. Hadfield, and T. Tucker, "SiC lightweight telescopes for advanced space applications 2. structures technology," in *SPIE Surveillance Technologies II*, pp. 296–303, 1992.

[23] P. N. Robb, R. R. Charpentier, S. V. Ljubarsky, M. N. Tolstoy, G. V. Evteev, and Y. P. Khimitch, "Three-mirror anastigmatic telescope with a 60-cm aperture diameter and mirrors made of silicon carbide," in *Proc. SPIE* (M. A. Ealey, ed.), vol. 2543, pp. 185–193, International Society for Optics and Photonics, oct 1995.

[24] J. Robichaud, M. Anapol, L. Gardner, and P. Hadfield, "Ultralightweight off-axis three mirror anastigmatic SiC visible telescope," in *SPIE Proceedings*, vol. 2543, pp. 180–184, 1995.

[25] D. Castel, B. Calvel, P. Lamy, K. Dohlen, and M. B. Sicspace, "The monolithic SiC telescope of the OSIRIS Narrow Angle Camera for the cometary mission ROSETTA," in *Proceedings of SPIE*, vol. 3785, pp. 277–786, 1999.

[26] A. Zocca, P. Colombo, C. M. Gomes, and J. Günster, "Additive Manufacturing of Ceramics: Issues, Potentialities, and Opportunities," *Journal of the American Ceramic Society*, vol. 98, pp. 1983–2001, jul 2015.

[27] K. Terrani, B. Jolly, and M. Trammell, "3D printing of highpurity silicon carbide," *Journal of the American Ceramic Society*, vol. 103, pp. 1575–1581, mar 2020.

[28] R. A. Paquin, "Materials for mirror systems: an overview," in *SPIE Silicon Carbide Materials for Optics and Precision Structures* (M. A. Ealey, ed.), vol. 2543, pp. 2–11, oct 1995.

[29] J. S. Johnson, K. D. Grobsky, and D. Bray, "Rapid fabrication of lightweight silicon-carbide mirrors," in *Optomechanical Design and Engineering 2002*, vol. 4771, p. 243, 2002.

[30] T. E. of Encyclopaedia Britannica, "Hale Telescope — astronomy — Britannica," 2010.

[31] U. Papenburg, W. Pfrang, G. S. Kutter, C. E. Mueller, B. P. Kunkel, M. Deyerler, and S. Bauereisen, "Optical and optomechanical ultralightweight C/SiC components," in *SPIE International Symposium* (H. P. Stahl, ed.), vol. 3782, pp. 141–156, International Society for Optics and Photonics, nov 1999.

[32] Z. Xuejun, Z. Zhongyu, Z. Ligong, and F. Di, "Manufacturing and Testing SiC Aspherical mirrors in Space telescopes," in *Proc. SPIE, Optical Devices and Instruments*, pp. 602402–1, 2005.

[33] J. Robichaud, D. Sampath, C. Wainer, J. Schwartz, C. Peton, and S. Mix, "Silicon carbide optics for space and ground based astronomical telescopes," in *Proceedings of SPIE*, vol. 8450, 2012.

[34] J. Ding, X. wu FAN, Z. PANG, L. FENG, Q. CHEN, and Z. MA, "Manufacturing and testing of surface modified silicon carbide aspheric mirror," in *Proc. SPIE 10837, 9th International Symposium on Advanced Optical Manufacturing and Testing Technologies: Large Mirrors and Telescopes*, vol. 10837, p. 41, 2019.

[35] G. Ding, R. He, K. Zhang, N. Zhou, and H. Xu, "Stereolithography 3D printing of SiC ceramic with potential for lightweight optical mirror," *Ceramics International*, vol. 46, pp. 18785–18790, aug 2020.

[36] T. Hull, M. J. Riso, J. M. Barentine, and A. Magruder, "Mid-spatial frequency matters: examples of the control of the power spectral density and what that means to the performance of imaging systems," in *Infrared Technology and Applications XXXVIII*, vol. 8353, p. 835329, 2012.

[37] P. A. Lightsey, A. A. Barto, and J. Contreras, "Optical Performance for the James Webb Space Telescope," in *Proc. SPIE, Optical, Infrared, and Millimeter Space Telescopes*, vol. 5487, pp. 825–832, 2004.

[38] M. Clampin, "The James Webb Space Telescope (JWST)," *Advances in Space Research*, vol. 41, no. 12, pp. 1983–1991, 2008.

[39] J. Reimers, A. Bauer, K. P. Thompson, and J. P. Rolland, "Freeform spectrometer enabling increased compactness," *Light: Science & Applications*, vol. 6, pp. e17026–e17026, jul 2017.

[40] A. H. Slocum, "Kinematic couplings for precision fixturing Part I: Formulation of design parameters," *Precision Engineering*, vol. 10, no. 2, pp. 85–91, 1988.

[41] A. Slocum, "Kinematic couplings: A review of design principles and applications," *International Journal of Machine Tools & Manufacture*, vol. 50, pp. 310–327, 2009.

[42] M. L. Culpepper, "Design of quasi-kinematic couplings," *Precision Engineering*, vol. 28, pp. 338–357, jul 2004.

[43] P. J. Willoughby, A. J. Hart, and A. H. Slocum, "Experimental Determination of Kinematic Coupling Repeatability in Industrial and Laboratory Conditions," *Journal of Manufacturing Systmes*, vol. 24, pp. 108–121, 2005.

[44] L. C. Hale and A. H. Slocum, "Optimal design techniques for kinematic couplings," *Precision Engineering*, vol. 25, pp. 114–127, 2001.

[45] A Slocum, "Design of three groove Kinematic couplings," *Precision Engineering*, vol. 14, no. 2, pp. 67–76, 1992.

[46] J. R. C. G. Kruis, *Design, analysis, testing and applications of two-body and three-body kinematic mounts*. PhD thesis, Ecole Polytechnique Federale De Lausanne, 2016.

[47] P. Schmiechen and A. Slocum, "Analysis of kinematic systems: a generalized approach," *Precision Engineering*, vol. 19, no. 1, pp. 11–18, 1996.

[48] L. C. Hale, *Principles and Techniques for Designing Precision Machines*. PhD thesis, MIT, 1999.

[49] M. Barraja and R. Ryan Vallance, "Tolerancing kinematic couplings," *Precision Engineering*, vol. 29, pp. 101–112, 2005.

[50] N. W. Horvath and M. A. Davies, "Concurrent engineering of a next-generation freeform telescope: mechanical design and manufacture," in *Advanced Optics for Imaging Applications: UV through LWIR IV* (P. L. Marasco, J. S. Sanghera, and J. N. Vizgaitis, eds.), vol. 10998, p. 35, SPIE, may 2019.

[51] W. C. Young and R. G. Budynas, *Roark's Formulas for Stress and Strain*. McGraw-Hill, 8th ed., 2012.

[52] P. J. Smilie, "Design and characterization of an infrared Alvarez lens," *Optical Engineering*, vol. 51, pp. 13006–1 – 13006–7, 2012.

[53] I. Inasaki, "Grinding of Hard and Brittle Materials," *CIRP Annals - Manufacturing Technology*, vol. 36, pp. 463–471, jan 1987.

[54] S. Malkin and T. W. Hwang, "Grinding Mechanisms for Ceramics," *CIRP Annals - Manufacturing Technology*, vol. 45, pp. 569–580, jan 1996.

[55] R. Komanduri, D. A. Lucca, and Y. Tani, "Technological advances in fine abrasive processes," *CIRP Annals - Manufacturing Technology*, vol. 46, pp. 545–596, jan 1997.

[56] P. Shanmugam, N. Sizemore, J. D. Owen, E. Fess, J. Hamel, J. Ross, J. Lambropoulos, and M. Davies, "Grinding of Silicon Carbide for Freeform Optics," in *32nd ASPE Annual Meeting*, 2017.

[57] Z. Zhong and T. Nakagawa, "New Grinding Methods for Aspheric Mirrors with Large Curvature Radii," *CIRP Annals - Manufacturing Technology*, vol. 41, pp. 335–338, jan 1992.

[58] Y. Namba, H. Kobayashi, H. Suzuki, K. Yamashita, and N. Taniguchi, "Ultraprecision surface grinding of chemical vapor deposited silicon carbide for X-ray mirrors using resinoid-bonded diamond wheels," *CIRP Annals - Manufacturing Technology*, vol. 48, pp. 277–280, jan 1999.

[59] J. L. Ruckman, E. M. Fess, and H. M. Pollicove, "Deterministic processes for manufacturing conformal (freeform) optical surfaces," in *Window and Dome Technologies and Materials VII* (R. W. Tustison, ed.), vol. 4375, pp. 108–113, SPIE, sep 2001.

[60] J. Kovach and S. Malkin, "High-speed, low-damage grinding of advanced ceramics Phase 1. Final report," tech. rep., Oak Ridge National Laboratory (ORNL), Oak Ridge, TN, mar 1995.

[61] M. Sweeney, M. Acreman, T. Vettese, R. Myatt, and M. Thompson, "Application and testing of additive manufacturing for mirrors and precision structures," in *SPIE Material Technologies and Applications to Optics, Structures, Components, and Sub-Systems II* (M. Krödel, J. L. Robichaud, and W. A. Goodman, eds.), vol. 9574, p. 957406, sep 2015.

[62] E. Hilpert, J. Hartung, S. Risse, R. Eberhardt, and A. Tünnermann, "Precision manufacturing of a lightweight mirror body made by selective laser melting," *Precision Engineering*, vol. 53, pp. 310–317, jul 2018.

[63] N. Heidler, E. Hilpert, J. Hartung, H. von Lukowicz, C. Damm, T. Peschel, and S. Risse, "Additive manufacturing of metal mirrors for TMA telescope," in *Optical Fabrication, Testing, and Metrology VI* (S. Schröder and R. Geyl, eds.), vol. 10692, p. 11, SPIE, jun 2018.

[64] W. P. Barnes, "Optimal Design of Cored Mirror Structures," *Applied Optics*, vol. 8, no. 6, pp. 1191–1196, 1969.

[65] P. K. Mehta, "Flexural Rigidity Characteristics Of Light-Weighted Mirrors," in *SPIE Structural Mechanics of Optical Systems II*, vol. 0748, pp. 158–171, 1987.

[66] D. Vukobratovich, B. Iraninejad, R. M. Richard, Q. M. Hansen, and R. Melugin, "Optimum shapes for lightweighted mirrors," in *SPIE Advanced Technology Optical Telescopes I*, vol. 0332, pp. 419–423, 1982.

[67] T. M. Valente and D. Vukobratovich, "A Comparison Of The Merits Of Open-Back, Symmetric Sandwich, And Contoured Back Mirrors As Light-Weighted Optics.," in *SPIE Precision Engineering and Optomechanics*, vol. 1167, pp. 20–36, 1989.

[68] D. Vukobratovich, "Lightweight Laser Communications Mirrors Made With Metal Foam Cores," in *Proceedings of SPIE*, pp. 216–226, 1989.

[69] R. E. Parks, "Specifications: figure and finish are not enough," in *SPIE An Optical Believe It or Not: Key Lessons Learned*, vol. 7071, p. 70710B, 2008.

[70] M. Beier, J. Hartung, T. Peschel, C. Damm, A. Gebhardt, S. Scheiding, D. Stumpf, U. D. Zeitner, S. Risse, R. Eberhardt, and A. Tünnermann, "Development, fabrication, and testing of an anamorphic imaging snap-together freeform telescope," *Applied Optics*, vol. 54, no. 12, p. 3530, 2015.

[71] N. W. Horvath, M. A. Davies, and S. R. Patterson, "Kinematic mirror mount design for ultra-precision manufacturing, metrology, and system level integration for high performance visible spectrum imaging systems," *Precision Engineering*, vol. 60, pp. 535–543, nov 2019.

[72] J. Robichaud, "SiC Optics for EUV, UV, and Visible Space Missions," in *SPIE Astronomical Telescopes + Instrumentation*, vol. 4854, pp. 39–49, 2003.

[73] D. Castel, E. Sein, S. Lopez, T. Nakagawa, and M. Bougoin, "The 3.2m all SiC Telescope for SPICA," in *Proc. SPIE*, vol. 8450, pp. 1–13, 2012.

[74] E. Sein, Y. Toulemont, F. Safa, M. Duran, P. Deny, D. D. Chambure, T. Passvogel, and G. PILBRATT ASTRIUMToulouse, "A 3.5 M SiC telescope for HERSCHEL Mission," in *Proc. SPIE 4850*, 2003.

[75] N. Horvath, A. Honeycutt, and M. A. Davies, "Grinding of additively manufactured silicon carbide surfaces for optical applications," *CIRP Annals*, vol. 69, no. 1, pp. 509–512, 2020.

[76] K. Schwertz and J. H. Burge, *Optomechanical Design and Analysis*. SPIE Press, 2012.

[77] M. F. Ashby, "The Mechanical Properties of Cellular Solids," *Metallurgical Transanctions A*, vol. 14A, pp. 1755–1769, 1983.

[78] S. Liu, R. Hu, Q. Li, P. Zhou, Z. Dong, and R. Kang, "Topology optimization-based lightweight primary mirror design of a large-aperture space telescope," *Applied Optics*, vol. 53, no. 35, pp. 8318–8325, 2014.

[79] O. Al-Ketan, R. Rowshan, and R. K. Abu Al-Rub, "Topology-mechanical property relationship of 3D printed strut, skeletal, and sheet based periodic metallic cellular materials," *Additive Manufacturing*, vol. 19, pp. 167–183, jan 2018.

[80] D. Cellucci and K. C. Cheung, "Evaluation of Cellular Solids Derived from Triply Periodic Minimal Surfaces," *ASME Manufacturing Science and Engineering*, dec 2015.

[81] Y. Lu, W. Zhao, Z. Cui, H. Zhu, and C. Wu, "The anisotropic elastic behavior of the widely-used triply-periodic minimal surface based scaffolds," *Journal of the Mechanical Behavior of Biomedical Materials*, vol. 99, pp. 56–65, nov 2019.

[82] J. M. Guedes and N. Kikuchi, "Preprocessing and postprocessing for materials based on the homogenization method with adaptive finite element methods," *Computer Methods in Applied Mechanics and Engineering*, vol. 83, pp. 143–198, 1990.

APPENDIX A: MATLAB® SCRIPTS

A.1 Supplementary Code for Kinematic Mount Analysis

A.1.1 Calculator for Hertzian contact stress, mount compliance, and repeatability

```
% Hertz Stress Calculator - Kinematic
% coupling Contact Stress
% Reference: Roarks Formulas for Stress and Strain 8th Ed.
- Page 716 case 4
% Layton C. Hale, Alex H. Slocum, "Optimal design techniques
for kinematic couplings", Precision Engineering 25 (2001) 114127
%
%Generated by: N. Horvath 3/9/18
%Revision 1: Analytical model of deflection
    and stiffness 1/29/19
%Revision 2: Added repeatability and failure
    criteria 2/20/19
%Revision 3: Cleaned up output with fprintf for
    dissertation appendix 9/6/2020
clear
clc
close all
%
% User Inputs
%
```

```
% Body 1 is the "Sphere" with Body 2 being the "Groove"
% XZ Plane is through the groove center - Perpendicular to DOF axis
% YZ Plane is along groove center - Parallel to DOF axis
% Units unless otherwise stated are in mm and Newtons

Preload=0:.01:200;
Groove_angle=58; %degrees
E1=203000; %Elastic Modulus MPa
E2=E1;
v1=0.3; %Possion's ratio
v2=v1;
mu=.04; %Friction Coefficient
HB=654; %Brinell Hardness
%Radii
r1x=12.7;
r1y=12.7;
r2x=6.35;
r2y=100E6;

% Input failure criteria
Allowable_Shear=1200*.58; %MPa

% Maximum Compliance Goal
C_max = 45; % nm/N

%Equations to solve contact pressure and system
%predictive repeatability
```

```
%
Ce=(1-v1^2)/E1+(1-v2^2)/E2;
Req=1/r1x+1/r1y+1/r2x+1/r2y;
Kd=1.5/Req;
phi=0;
cos=Kd/1.5*((1/r1x-1/r1y)^2+(1/r2x-1/r2y)^2+...
    2*(1/r1x-1/r1y)*(1/r2x-1/r2y)*cosd(2*phi))^(1/2);
load=Preload/2*sind(Groove_angle/2);

%Spline interpolation to make a continuous curve from lookup table
% References "cosTheta.m" and "splineFit.m" functions
[alpha,beta,lamda]=cosTheta(cos);

%Outputs
d = zeros(1,length(load));
k = zeros(1,length(load));
c = zeros(1,length(load));
Contact_Area = zeros(1,length(load));
Shear = zeros(1,length(load));
for i = 1:length(load)
    d(i)=lamda*((load(i)^2*Ce^2)/Kd)^(1/3);
    c(i)=(2*lamda*((load(i)^2*Ce^2)/Kd)^(1/3)/(3*load(i)));
    k(i)=1./c(i);

    a=alpha*(load(i)*Kd*Ce)^(1/3);
    b=beta*(load(i)*Kd*Ce)^(1/3);
    Contact_Area(i)=pi*a*b;
```

```
    Shear(i) = 1.5*(load(i)/Contact_Area(i))*...
        (0.303+0.0855*(b/a)-0.808*(b/a)^2);
end
%Compliance to nm/N
c=c*10^6;
% Figure for compliance curve as function of preload
figure()
[AX,H1,H2]=plotyy(Preload,k,Preload,c,'semilogy');
set(gca,'FontSize', 10)
set(H1,'LineStyle','-','LineWidth',2,'Color','k')
set(AX,{'ycolor'},{'k';'b'})
set(H2,'LineStyle','-.','LineWidth',2,'Color','b')
ylabel(AX(1),'Stiffness (N/mm)')
ylabel(AX(2),'Compliance (nm/N)')
xlabel('Preload (N)')
axis(AX(1),[0 200 1e3 1e5])
axis(AX(2),[0 200 10 100])
legend('Stiffness','Compliance','Location','NorthEast')
grid

% Finding Compliance Goal and subsequent Load
m = find(c>=C_max); %dummy index
load =load(m(end)); %Max value in array

%Failure Criteria and Repeatability
Max_P=(3*load)/(2*pi*a*b);
%Repeatability=mu*((2*Req/3))^(1/3)*(load/((E1+E2)/2))^(2/3)
Repeatability_actual=(mu*load)./(18*k(m(end)).*...
```

```
    sind(Groove_angle).^2.*cosd(Groove_angle)).*...
    (2*sqrt(3)+cosd(Groove_angle)+...
    sind(2*Groove_angle))*10^6; %nm;
Z_Deflect=-d(m(end))*cosd(Groove_angle)*10^6; %nm
Max_Shear=Max_P*(0.303+0.0855*(b/a)-0.808*(b/a)^2); %MPa

e2=(1-(b/a)^2); %approximate eccentricity

sig_a=Max_P*(1-2*v1)*(b/(a*e2))*...
    (1/sqrt(e2)*atanh(sqrt(e2))-1); %MPa
sig_b=Max_P*(1-2*v1)*(b/(a*e2))*...
    (1-b/(a*sqrt(e2))*atan((sqrt(e2)*a)/b)); %MPa

SF = Allowable_Shear./Max_Shear;

Pload_Req = Preload(m(end));

fprintf('The estimated repeatability per contact considering
    a friction coefficient of %1.2f is %2.0f nm.
    \n',mu,Repeatability_actual)
fprintf('The axial displacement of the joint due to preload
    is %4.0f nm. \n',Z_Deflect)
fprintf('The principal shear stress values are %2.1f MPa
    and %2.1f MPa. \n',sig_a,sig_b)
fprintf('The safety factor against plastic deformation
    from shear stress is %1.1f. \n',SF)
fprintf('The preload required to satisfy the compliance
```

```
    goal of %2.0f nm/N is %2.0f N.',C_max,Pload_Req)
```

The estimated repeatability per contact considering a friction coefficient of 0.04 is 24 nm. The axial displacement of the joint due to preload is -682 nm. The principal shear stress values are 72.8 MPa and 54.5 MPa. The safety factor against plastic deformation from shear stress is 8.5. The preload required to satisfy the compliance goal of 45 nm/N is 79 N.

A.1.1.1 Functions for mount calculator

```
function[alpha, beta, lamda]= cosTheta(cos_theta)

%Vectors from Roarks Formulas for Stress and Strain
- Page 716 case 4
%Generated by N. Horvath 3/9/18

x=[0 0.1 0.2 0.3 0.4 0.5 0.6 0.7 0.75...
    0.8 0.85 0.9 0.92 0.94 0.96...
    0.98 0.99];
alpha=[1 1.07 1.15 1.242 1.351 1.486...
    1.661 1.905 2.072 2.292 2.6 3.093...
    3.396 3.824 4.508 5.937 7.774];
beta=[1 0.936 0.878 0.822 0.769 0.717...
    0.664 0.608 0.578 0.544 0.507 0.461...
    0.438 0.412 0.378 0.328 0.287];
lamda=[0.75 0.748 0.743 0.734 0.721...
    0.703 0.678 0.644 0.622 0.594 0.559...
    0.51 0.484 0.452 0.41 0.345 0.288];

[Pa, ~] = splineFit(x, alpha);
```

```
[Pb, ~] = splineFit(x, beta);
[Pl, ~] = splineFit(x, lamda);

alpha=Pa(cos_theta);
beta=Pb(cos_theta);
lamda=Pl(cos_theta);

% Fitting function for lookup table

function [fitresult, gof] = splineFit(x, y)
% Generated by: N. Horvath 3/9/18
% This interpolates the lookup table with a
smooth spline curve for the
% cosTheta.m values

%% Fit: 'alpha'.
[xData, yData] = prepareCurveData( x, y );

% Set up fittype and options.
ft = 'splineinterp';

% Fit model to data.
[fitresult, gof] = fit( xData, yData, ft,
'Normalize', 'on' );
```

A.1.2 Calculator for change in preload and resultant forces due to process forces

```
% Kinematic mount change in groove forces due to machining forces
% Generated by: N. Horvath 1/30/19\\
% Generates 2 figures that show both the change in preload
% and change in reaction forces for each contact patch.
% This variability can be used as a delta % preload to ensure
% both a maximum compliance is not exceeded and the maximum
% shear stress is not exceed.
Use the max delta values in the "Kinematic\_Mount\_Calc.m".


clear all
close all
clc
syms x y z Fc r L p

% User inputs for groove and kinematic mount geometry

B=210; %Angle of 2nd groove from defined X axis
a=120; %Angle from 2nd groove to 3rd groove

%Symbolic system of equations
eqns = [ Fc*(r/L)-y-z == x;...
(Fc*(r/L)*cosd(p)-z*cosd(B+a))/cosd(B) == y;...
(Fc*(r/L)*sind(p)-x-y*sind(B))/sind(B+a) == z];
S = solve(eqns);
sol = [S.x; S.y; S.z];
clear Fc r L p
```

```
% User Inputs %

Fc=1; % Tangential cutting force
u=0.4; % Ratio of  normal force to tangential force
%(turning expected is <1 and grinding >1)
groove_angle = 58;
R = 135; %Radius of surface under cut
L=0.66*R; %Radius of kinematic circle
n=5; %Number of discrete radial locations to quantify

%Forces
F1 = matlabFunction(S.x);
F2 = matlabFunction(S.y);
F3 = matlabFunction(S.z);

p=[0:1:360]; %One revolution of the mirror
Fr1 = zeros(n,length(p));
Fr2 = zeros(n,length(p));
Fr3 = zeros(n,length(p));

% Populate force array as a function of
% azimuthal and radial location
for j = 1:n
    r = R*(j/n);
    Fr1(j,:) = F1(Fc,L,p,r);
    Fr2(j,:) = F2(Fc,L,p,r);
```

```
    Fr3(j,:) = F3(Fc,L,p,r);
end

% Change in preload from process force
figure()
subplot(2,2,1)
plot(p,Fr1)
legend('r = 0.2R','r = 0.4R','r = 0.6R','r = 0.8R','r = R')
ylabel('\DeltaPreload (N)')
xlabel('degrees')
title('Joint 1')
axis([ 0 360 -1 2])
set(gca,'Xtick',0:60:360)
grid

subplot(2,2,2)
plot(p,Fr2)
% legend('r = .2R','r = .4R','r = .6R','r = .8R','r = R')
ylabel('\DeltaPreload (N)')
xlabel('degrees')
title('Joint 2')
axis([ 0 360 -1 2])
set(gca,'Xtick',0:60:360)
grid

subplot(2,2,3)
plot(p,Fr3)
```

```
% legend('r = 0.2R','r = 0.4R','r = 0.6R','r = 0.8R','r = R')
ylabel('\DeltaPreload (N)')
xlabel('degrees')
title('Joint 3')
axis([ 0 360 -1 2])
set(gca,'Xtick',0:60:360)
grid

% Groove resultant forces

tht=groove_angle/2;
theta_minus = (cosd(tht)-u*sind(tht))/...
    (2*cosd(tht)*sind(tht));
theta_plus = (cosd(tht)+u*sind(tht))/...
    (2*cosd(tht)*sind(tht));

F_11 = Fr1.*theta_minus;
F_21 = Fr1.*theta_plus;

F_12 = Fr2.*theta_minus;
F_22 = Fr2.*theta_plus;

F_13 = Fr3.*theta_minus;
F_23 = Fr3.*theta_plus;

figure()
subplot(3,2,1)
```

```
plot(p,F_11)
% legend('r = .2R','r = .4R','r = .6R','r = .8R','r = R')
title('F11')
xlabel('degrees')
ylabel('Reaction Force (N)')
axis([ 0 360 -0.75 2])
set(gca,'Xtick',0:90:360)
grid

subplot(3,2,2)
plot(p,F_21)
legend('r = 0.2R','r = 0.4R','r = 0.6R','r = 0.8R','r = R')
title('F21')
xlabel('degrees')
ylabel('Reaction Force (N)')
axis([ 0 360 -0.75 2])
set(gca,'Xtick',0:90:360)
grid

subplot(3,2,3)
plot(p,F_12)
% legend('r = .2R','r = .4R','r = .6R','r = .8R','r = R')
title('F12')
xlabel('degrees')
ylabel('Reaction Force (N)')
axis([ 0 360 -0.75 2])
set(gca,'Xtick',0:90:360)
```

```
grid

subplot(3,2,4)
plot(p,F_22)
% legend('r = .2R','r = .4R','r = .6R','r = .8R','r = R')
title('F22')
xlabel('degrees')
ylabel('Reaction Force (N)')
axis([ 0 360 -0.75 2])
set(gca,'Xtick',0:90:360)
grid

subplot(3,2,5)
plot(p,F_13)
% legend('r = .2R','r = .4R','r = .6R','r = .8R','r = R')
title('F13')
xlabel('degrees')
ylabel('Reaction Force (N)')
axis([ 0 360 -0.75 2])
set(gca,'Xtick',0:90:360)
grid

subplot(3,2,6)
plot(p,F_23)
% legend('r = .2R','r = .4R','r = .6R','r = .8R','r = R')
title('F23')
xlabel('degrees')
```

```
ylabel('Reaction Force (N)')
axis([ 0 360 -0.75 2])
set(gca,'Xtick',0:90:360)
grid

max_dp = Fr1(n,90);
min_dp = Fr1(n,270);
max_fg = max(F_11(n,90), F_21(n,90));
% State results
fprintf('The maximum increase in preload is %1.1f N,
    occurring when tool force directly over a joint.
    \n',max_dp)
fprintf('The maximum decrease in preload is %1.1f N,
occurring when tool force is 180 deg from joint.
    \n', min_dp)
fprintf('The maximum change in resultant force
    is %1.1f N.',max_fg)
```

A.2 Supplementary Code for FE Analysis Curve Fitting With Zernike Polynomials

```
% Zernike polynomial fitting to deformed FEA results
% Generated by: N. Horvath 2/10/19
% Import FEA initial point cloud and deformed point cloud
% Set the proper clear aperture to obtain correct normalization
% radius
% Fitting performed by open source ZernikeCalc.m by J. Howard
% ZernikeCalc.m modified by N. Horvath to output PV surface error
close all
clc
clear
%
[Xi,Yi,Zi,Xf,Yf,Zf] = importFEA('M1 Aluminum Gravity 1G Z.txt');

% User Inputs
CA=184; %Clear aperture
N=1; %Grid spacing - refine until convergence in residual map
Z = 'Standard'; % Zernike index - refer to ZernikeCalc.m
% to ensure correct index ordering
Order = 21; %Number of Zernike Terms

[x,y] = meshgrid(-CA/2:N:CA/2);
F = scatteredInterpolant(Xi,Yi,Zi); %Initial Surface Map Fit
G = scatteredInterpolant(Xf,Yf,Zf); %Deformed Surface Map Fit

F.Method = 'natural'; %Interpolation type
```

```
G.Method = 'natural';


Ui = F(x,y);
Vi = G(x,y);


figure()
subplot(2,2,1);
plot3(Xi,Yi,Zi,'r+')
hold on
plot3(Xf,Yf,Zf,'bo')
surf(x,y,Ui,'edgecolor','none');
surf(x,y,Vi,'edgecolor','none');
xlabel('mm')
ylabel('mm')
zlabel('mm')
grid
axis([-CA/2 CA/2 -CA/2 CA/2]);
hold off


subplot(2,2,4)
plot3(Xi,Yi,Zi,'r+')
hold on
plot3(Xf,Yf,Zf,'bo')
surf(x,y,Ui,'edgecolor','none');
surf(x,y,Vi,'edgecolor','none');
xlabel('mm')
ylabel('mm')
```

```
zlabel('mm')
grid
view(2)
axis([-CA/2 CA/2 -CA/2 CA/2]);
hold off

dUV=(Vi-Ui); %Subtraction of deformed map from initial map
figure()
surf(dUV)
Z_index = 1:Order;
Rnorm = length(x)/2*N; %Normalization Radius

%Generate coefficients
[Zernike,coeff] = ZernikeCalc(Z_index, dUV, length(x), Z, 0, Rnorm);

%Initial-Fit-Residual Plot and RMS and PV results
ZernikeCalc(Z_index, dUV, length(x), Z, 0, Rnorm);

% Select terms
Zernike_fit = (Zernike(:,:,1)+Zernike(:,:,2)+Zernike(:,:,3)...
   +Zernike(:,:,4)+Zernike(:,:,5)+Zernike(:,:,6)...
   +Zernike(:,:,7)+Zernike(:,:,8)+Zernike(:,:,9)...
   +Zernike(:,:,10)+Zernike(:,:,11)+Zernike(:,:,12)...
   +Zernike(:,:,13)+Zernike(:,:,14)+Zernike(:,:,15)...
   +Zernike(:,:,16)+Zernike(:,:,17)+Zernike(:,:,18)...
   +Zernike(:,:,19)+Zernike(:,:,20)+Zernike(:,:,21))...
   *10^6; % Convert Height to nm
```

```
% Reshape for cropping
A=reshape(x,[],1);
B=reshape(y,[],1);
C=reshape(Zernike_fit,[],1);

Zernike_fit_crop = CACrop(A,B,C,CA);
ZRC = reshape(Zernike_fit_crop,[],length(Zernike_fit));

figure()
subplot(1,2,1)
surf(x,y,ZRC,'edgecolor','none')
c=colorbar;
c.Label.String = 'Deflection (nanometers)';
xlabel('mm')
ylabel('mm')
zlabel('nm')
% title('Zernike Fit')
view([25,50])
axis([-CA/2 CA/2 -CA/2 CA/2]);
title('(a)')
subplot(1,2,2)
contour(x,y,ZRC,10)
c=colorbar;
c.Label.String = 'Deflection (nanometers)';
xlabel('mm')
ylabel('mm')
```

```
zlabel('nm')
axis([-CA/2 CA/2 -CA/2 CA/2]);
title('(b)')

% Raw Data Point Overlay
Aa=reshape(x,[],1);
Ba=reshape(y,[],1);
Ca=reshape(dUV,[],1);

Data_crop = CACrop(Aa,Ba,Ca,CA);
dUVC = reshape(Data_crop,[],length(Zernike_fit));

figure()
plot3(x,y,dUVC*10^6,'r+')
hold on
surf(x,y,ZRC)
xlabel('mm')
ylabel('mm')
zlabel('nm')
grid
```

APPENDIX B: DERIVATION OF THE LENGTH OF CUT PER DIAMOND GRAIN IN A CROSS AXIS GRINDING CONFIGURATION

The cross axis grinding configuration (Chapter 3, Fig. 3.3) results in a length of cut on a helical path for each grain. This derivation quantifies the length of travel per grain for the major diameter of the wheel.

Nomenclature

ϕ_e	Exit angle of cut
ϕ_s	Start angle of cut
θ	Angle between center line of wheel and tip of cusp pattern
d	Depth of cut
f	Feed per revolution
h	Distance from center of wheel to workpiece top
L	Length of cut per grain
R	Wheel major radius
s	Stepover

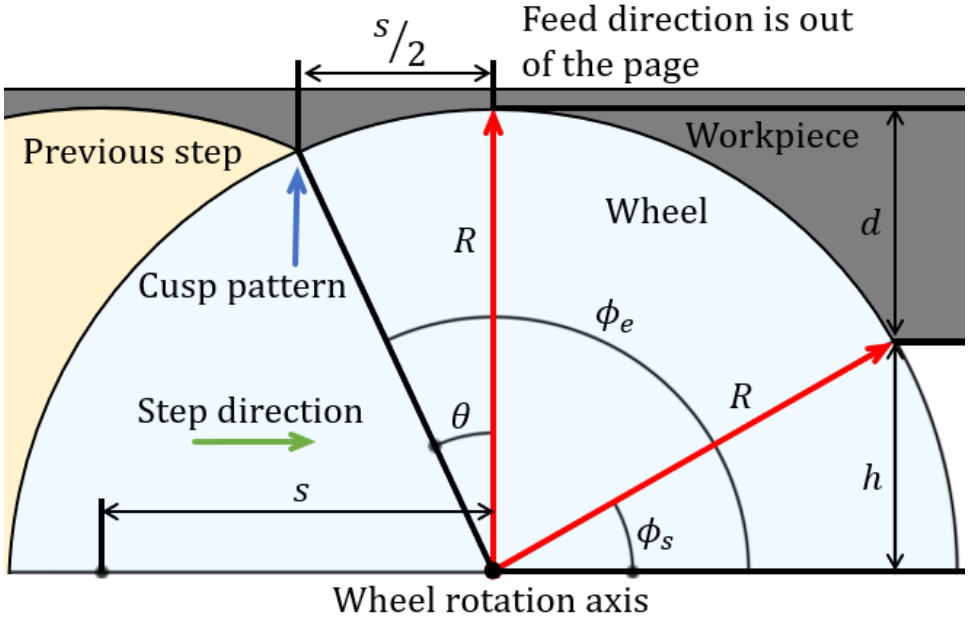

Figure B.1: A schematic of the wheel-workpiece interaction in cross axis grinding

The start angle is shown as:

$$\begin{aligned} \sin\phi_s &= \frac{h}{R} \\ R &= h + d \\ \therefore \phi_s &= \sin^{-1}\left(\tfrac{R-d}{R}\right) \end{aligned} \tag{B.1}$$

The exit angle is shown as:

$$\begin{aligned} \sin\theta &= \frac{s}{2R} \\ \phi_e &= \tfrac{\pi}{2} + \theta \\ \therefore \phi_e &= \sin^{-1}\left(\tfrac{s}{2R}\right) + \tfrac{\pi}{2} \end{aligned} \tag{B.2}$$

Parametric form for wheel and feed:

$$\begin{aligned} r(t) &= \langle x(t), y(t), z(t)\rangle \\ x(t) &= R\cos t \\ y(t) &= R\sin t \\ z(t) &= \left(\tfrac{f}{2\pi}\right) t \\ \phi_s &\leqslant t \leqslant \phi_e \end{aligned} \tag{B.3}$$

The distance traveled per grain is shown as:

$$\begin{aligned} L &= \int_{\phi_s}^{\phi_e} |r'(t)|dt \\ |r'(t)| &= \sqrt{R^2 + \left(\tfrac{f}{2\pi}\right)^2} \end{aligned} \tag{B.4}$$

$$\therefore L = (\phi_e - \phi_s)\sqrt{R^2 + \left(\tfrac{f}{2\pi}\right)^2} \tag{B.5}$$